2017

Correlating Metastable-Atom Density, Reduced Electric Field, and Electron Energy Distribution in the Initiation, Transient, and Post-Transient Stages of a Pulsed Argon Discharge

James B. Franek

Correlating Metastable-Atom Density, Reduced Electric Field, and Electron Energy Distribution in the Initiation, Transient, and Post-Transient Stages of a Pulsed Argon Discharge

James B. Franek

Dissertation submitted
to the College of Arts and Sciences
at West Virginia University

In partial fulfillment of the requirements of the degree of

Doctor of Philosophy in
Physics

Mark Koepke, Ph.D., Chair
Julian Schulze, Ph.D.
Paul Cassak, Ph.D.
Paul Miller, Ph.D.
Charter Stinespring, Ph.D.

Department of Physics and Astronomy

Morgantown, West Virginia
2017

Keywords: Optical Emission Spectroscopy (OES), 420.1-419.8nm argon emission-line ratio, Metastable-atom, Extended corona model

Abstract

Correlating Metastable-Atom Density, Reduced Electric Field, and Electron Energy Distribution in the Initiation, Transient, and Post-Transient Stages of a Pulsed Argon Discharge

James B. Franek

Argon emission lines, particularly those in the near-infrared region (700-900nm), are used to determine plasma properties in low-temperature, partially ionized plasmas to determine effective electron temperature [*Boffard et al.,* 2012], and argon excited state density [*Boffard et al.,* 2009] using appropriately assumed electron energy distributions. While the effect of radiation trapping influences the interpretation of plasma properties from emission-line ratio analysis, eliminating the need to account for these effects by directly observing the $3p_x$-to-$1s_y$ transitions [*Boffard et al.,* 2012] is preferable in most cases as this simplifies the analysis. In this dissertation, a 1-Torr argon, pulsed positive column in a hollow-cathode discharge is used to study the correlation between four quantities: 420.1-419.8nm emission-line ratio, metastable-atom density, reduced electric field, and electron energy distribution.

The extended coronal model is used to acquire an expression for 420.1-419.8nm emission-line ratio, which is sensitive to direct electron-impact excitation of argon excited states as well as stepwise electron-impact excitation of argon excited states for the purpose of inferring plasma quantities from experimental measurements. Initial inspection of the 420.1-419.8nm emission-line ratio suggests the pulse may be empirically divided into three distinct stages labelled the Initiation Stage, Transient Stage, and Post-Transient stage. Using equilibrium electron energy distributions from simulation to deduce excitation rates [Adams *et al.,* 2012] in the extended coronal model affords agreement between predicted and observed metastable density in the Post-Transient stage of the discharge [Franek *et al.,* 2015].

Applying this model-assisted diagnostic technique to the characterization of plasma systems utilizing lower-resolution spectroscopic systems is not straightforward, however, as the 419.8nm and 420.1nm emission-line profiles are convolved and become insufficiently resolved for treating the convolution as two separate emission-lines. To remedy this, the argon 425.9nm emission-line is evaluated as a proxy for the 419.8 nm emission-line. Both emission-lines (419.8nm and 425.9nm) are attributed to direct excitation from the argon ground state. The intensity of the 425.9nm emission-line is compared to the intensity of the 419.8nm emission-line over a range of plasma conditions to infer the same plasma quantities from similar experimental measurements. Discrepancies between the observed intensities of the emission-lines (419.8nm, 425.9nm) are explained by electron-impact cross-sections of their parent states. It is shown that the intensity of the argon 425.9nm emission-line is similar to that of the 419.8nm emission-line. The difference between the observed emission lines (425.9nm, 419.8nm) is attributed to the electron energy distribution in the plasma.

Table of contents

List of Figures

I. Introduction

In this section, the broad scope of plasma science is introduced. The transfer of energy between plasma species, and the concept of metastablility and the chemical properties of metastable-atoms are introduced as well. The effect of metastable-atoms on plasma emissions is discussed, and the idea of using a single-emission-line-ratio technique via Optical Emission Spectroscopy (OES) as a metastable-atom diagnostic is introduced.

The broad scope of plasma science

It is well-known that plasma is the most pervasive state of matter in the known universe. This pervasiveness is due to the large range of conditions attributed to the plasma state-of-matter, as depicted in figure (1.1). Figure (1.1) displays approximately fifteen orders-of-magnitude on the y-axis (Temperature) and thirty orders-of-magnitude on the x-axis (Density) to span 450 'square orders-of-magnitude' – most of which are attributed to the plasma state-of-matter. Liquids, gasses, and solids are roughly represented by 30 'square orders-of-magnitude' to the right of the 'quantum degeneracy' line [*Inan & Golkowski,* 2011]. Figure (1.1), perhaps, is the most-recognizable, most-reproduced plot in the plasma science community, as it is found in National Research Council reports [NRC, 2010], engineering textbooks [*Lieberman & Lichtenberg,* 1994; *Inan & Golkowski*, 2011], plasma physics textbooks [*Boyd & Sanderson*, 2003], presentations from the national laboratories [*Matzen et al., 2004*], and University websites[1,2] just to name a few. Figure (1.1) is so ubiquitous, in fact, that it is dubbed 'public domain' by the NRL plasma formulary.

While the plasma state-of-matter may describe a broad range of conditions as described by figure (1.1), the pervasiveness of the figure suggests that the scope of plasma scientists may be equally as broad. The field 'plasma science,' in fact, is academically pervasive, being so prevalent that in the United States university system, plasma science is studied in physics departments for fluid mechanics [*Wallace et al.,* 2004], space plasmas [*Gekelman et al.,* 1991], and atomic physics [*Boffard et al.,* 2004] applications; studied in mathematics departments for magnetohydrodynamic (MHD) theory [*Weitzner et al.,* 2014]; studied in biology and chemistry departments for medical [*Graves et al.,* 2012] or etching [*Zhu et al.,* 2014] applications; studied in astronomy departments for dusty plasma [*Pieper et al.,* 1996] applications; studied in geophysical institutes for space-plasma applications [*Delamere et al.,* 2015]; and studied in electrical [*Babaeva & Kushner,* 2014; *Chen,* 1991; *Boffard et al.*, 2004], mechanical [*Yun et*

[1] https://www.aa.washington.edu/research/HITsi/research/plasma, accessed 18 Nov, 2016.
[2] http://pedl.tamu.edu/index_files/AboutUs.html, accessed 18 Nov, 2016

al., *2000; Zhang et al.*, 2015; *Adomovich et al.,* 2009], computer [*Wang & Wendt, 2000]*, nuclear [*Foster et al.,* 2011; *Kugel et al.*, 2008], materials [*Fox-Lyon et al.,* 2013] and aerospace [*Yun et al,,* 2000; *Sheehan et al.*, 2014; *Keidar et al.,* 2001] engineering departments for technological applications. The depth of the field of plasma science should not be understated either, even within a sub-field of plasma science (e.g. low-temperature plasmas), as it is commonplace or even required for the plasma scientist to be well-versed in each of several subfields. While this dissertation is only concerned with the small portion of figure (1.1) denoted as 'Pulsed Plasmas,' this dissertation draws from quantum mechanics (Chapter II), atomic physics (Chapter III), electrical engineering (Chapter IV), plasma spectroscopy (Chapter V), and plasma kinetic theory/statistical mechanics (Chapter VI). This wealth of diverse physics makes low temperature plasmas a ripe area for gaining an all-inclusive understanding of atomic physics, plasma chemistry, as well as plasma physics [NRC, 2010] and has also led to the widespread use of low-temperature "lab plasmas" in semiconductor manufacturing, plasma medicine, lighting, plasma thrusters, materials processing, etc.

Energy transfer in pulsed, low-temperature plasmas

Low-temperature, partially ionized, non-equilibrium plasmas are often called "collisional plasmas" because energy is transferred via electron collisions [NRC, 2010]. An applied electric field transfers energy to plasma electrons that then distribute this energy to other species via Coulomb collisions. This balance between sustaining (input) power into the system and subsequent transfer into other plasma species results in many possible physical and chemical conditions that may be exploited for different purposes. In electron-atom collisions, energy from the incident electron may be transferred to a ground-state atom; the products of this collision depend on the initial energy of the incident electron and the properties of the target atom. While this process is discussed in detail in Chapter II, key points are discussed here.

For incident electron energy less than the energy threshold for ionization of the target atom $(E_{e^-} < E_{thresh})$, kinetic energy from the incident electron is

transferred to either kinetic energy of the target atom, in a momentum-transfer collision, or to potential energy of the target atom in an excitation collision, producing an excited-state atom. In the latter case, an electron from the target atom will transfer into a more-energetic (quantized) bound state and the remainder of the incident electron energy will either remain with the incident electron or be transferred into the kinetic energy of newly-formed excited-state atom. In argon, the excited state atom should have total angular momentum $J = 1$ due to angular momentum considerations. (Coulomb interactions are mediated via virtual photon exchange, and only one unit of angular momentum may be transferred to the ground state, $J = 0$, of argon.) These states are referred to as 'resonant states' and return to the ground state via photon emission ($\Delta J = 1$).

For incident electron energy near the threshold for ionization of the target atom ($E_{thresh} < E_{e^-} < 4 * E_{thresh}$), the target atom may ionize, and the remainder of the incident electron kinetic energy may either remain in the incident electron, or be partially transferred into the liberated electron. In either case, a low-energy electron may recombine with the newly formed ion and form an excited-state atom. Because electron-ion recombination is not governed by the exchange of a virtual photon, the resulting excited-state is not required to have total angular momentum $J = 1$. The likelihood of this interaction increases with increasing incident electron energy until the incident electron energy reaches approximately four-times the threshold energy for ionization [*Boffard et al.,* 2007].

Regardless of the population mechanisms, excited-states usually relax via photon emission, and return to the ground-state when possible. If the excited-state atom is unable to relax into a lower state, it remains in the excited state and is referred to as a "metastable-atom." Metastability is the result of conservation of angular momentum and can be better understood after examining the allowed energy levels in the noble gasses in detail.

Allowed energy states of the noble gasses, and metastability

Excited states of the noble gasses (except for He) correspond to the single-electron promotion of a $(np)^6$ outer-shell electron into a higher-lying bound state. The promotion of multiple electrons result in auto-ionizing states (states with

energy above the ionization energy) and its occurrence is considered rare. In argon, promoting one electron from the $(1s)^2(2s)^2(2p)^6(3s)^2(3p)^6\ {}^1S_0$ ground state into the nearby (4s) level results in excited states with electron configuration $(3p)^5(4s)^1$. (The core electron configuration $(1s)^2(2s)^2(2s)^6(3s)^2$ will be suppressed from now on.) The $(3p)^5$ ion core can be treated as an electron-hole with angular momentum vectors $l_{hole} = 1,\ s_{hole} = {}^1/_2$, and the promoted electron will have angular momentum vectors $l_{electron} = 0,\ s_{electron} = {}^1/_2$. Depending upon how the angular momentum vectors of the system are oriented with respect to each other, these angular momentum vectors may add (couple) in four different ways, resulting in total angular momentum J=1, 0, 1, or 2. The four predicted states J=1, 0, 1, 2 are empirically labeled $1s_2$, $1s_3$, $1s_4$, and $1s_5$, respectively, and are collectively referred to as the 1s, or $1s_x$ manifold in Paschen's notation. $1s_2$ is the most-energetic of the four states, $1s_3$ is the second-most energetic and so forth. While quantitative knowledge of the energy levels cannot be acquired by knowledge of angular momenta alone, a qualitative picture of the energy level sequence sometimes may be constructed by invoking the various coupling schemes. The utility of various coupling schemes are discussed in appendix I. The argon $1s_4$ and $1s_2$ states have total angular momentum J=1 and are called *resonant* states because they spontaneously decay to the argon ground state via photon emission. The argon $1s_3$ and $1s_5$ states, on the other hand, have total angular momentum J=0 and J=2 respectfully and are called *metastable* states because they do not spontaneously decay to the argon ground state via photon emission (interactions of the form $J = 0 \rightarrow J = 0$ and $\Delta J = 2$ are dipole forbidden).

Metastable-atoms are chemically different from ground-state atoms

To limit complex chemical reaction pathways between plasma species, basic plasma physics experiments often make use of the noble gasses. Argon plasmas are commonly studied because chemical reactions within the plasma are limited; however, 'chemical' reactions in the noble gasses are still present and must be considered. Even the noble gasses may form molecular compounds when the ground state atom is excited in a plasma — xenon hexafluoride, XeF_6, and the xenon excimer molecule, Xe_2, for example, are common byproducts in

plasma etching reactors.

The noble gasses are unique from the rest of the periodic table as they are the only group with a full valence-level electron shell, and are therefore un-reactive under normal circumstances. When ground-state noble gas atoms are brought into close proximity with each other, they do not form covalent bonds because the combination reaction is not energetically favorable, e.g. the reaction $Ar + Ar \rightarrow Ar_2$ does not occur at room temperature because the reaction is endothermic. Conversely, the formation of oxygen molecules is energetically favorable, i.e., $O + O \rightarrow O_2$ is spontaneous at room temperature because it is an exothermic reaction. This is why O_2 molecules are common at room temperature while Ar_2 are not. When a valance electron in an argon atom, however, is promoted into a more-energetic bound state, (as is the case for a metastable argon atom) the promoted electron becomes the only valence electron, and the argon atom is chemically reactive. The lone electron (with binding energy E=11.5eV for the $1s_5$ metastable argon atom) can now be ionized by contact with a halogen, e.g. $Ar^* + F \rightarrow Ar^+ + F^-$, or can now form an excimer molecule with another excited atom $Ar^* + Ar^* \rightarrow Ar_2$. Here, Ar^* represents an excited argon atom. Both of these reaction pathways, ionization collisions, and charge transfer collisions play a vital role in an argon discharge.

Even in a pure argon plasma, metastable argon atom chemistry must be considered in determining plasma properties. While only high-energy electrons (E=11.5eV) may excite ground-state argon atoms, both high- and low-energy electrons may interact with metastable argon atoms. Metastable argon atoms store 11.5eV of energy (nearly 67% of the ionization energy) as potential energy, and can become an electron-ion pair upon collision with a relatively low energy electron ~5eV. In the most-extreme case, a collision between a $1s_5$ metastable argon atom (E=11.5ev) and a 0.1eV electron may excite the metastable argon atom into the energetically-nearby $1s_4$ state (E=11.6eV). Therefore, even 0.1eV electrons may affect species balance in a plasma when metastable atoms are considered. Metastable-atoms can be excited by a greater percentage of the plasma electrons and have a profound effect on the electron energy distribution

(EED) and, therefore, on the optical emissions generated by the plasma.

The balance between neutral species density, metastable-atom density and ion density are mediated by electron collisions. Electrons produce neutral atoms (recombination), metastable-atoms (excitation), and ions (ionization) at various rates that are governed by the plasma electron energy distribution (EED). Metastable-atoms (by conservation of energy considerations) may only be produced by high-energy (E>11.5eV) electrons, which are produced by large electric fields. Since applied electric fields are diminished by the large mobility of electrons (large conductance) inherent in plasma, metastable-atom generation rates are greatest during the initiation of a plasma; thus, a pulsed plasma is typically more efficient at generating metastable-atoms. The metastable-atoms are, effectively, ground-state atoms with a reduced threshold for ionization (and excitation), and can play a vital role in the Townsend avalanche, and thus the transition from dark-discharge to glow-discharges. Similarly, ions (and their subsequent free-electrons) may only be created by high-energy electrons produced in the initiation of a plasma; thus, a pulsed plasma is typically more efficient at generating ions and electrons as well. These interactions can be used to calculate equilibrium species density and even equilibrium electron energy distributions by including the momentum transfer, ionization, and excitation collisions in the Boltzmann equation. This approach is utilized by the equilibrium Boltzmann solver Bolsig+ [*Hagelaar and Pitchford,* 2005], used in Chapter VI of this dissertation.

Because metastable-atoms are not charged, and cannot be controlled by classical (electrostatic) means, the creation and annihilation reactions of metastable atoms must be understood and controlled in order to control plasma chemistry. Specifically, pulsing a low-temperature plasma perturbs the equilibrium plasma by changing how energy is transferred to the plasma species, which has a drastic effect on plasma properties such as reactive species density, flux, and electron energy distribution; this makes pulsed plasmas a popular tool in the processing community. The bulk of this dissertation examines how pulsing a plasma affects the aforementioned plasma species, offers insight into the

underlying physics, and suggests how these plasmas may be diagnosed.

Metastable-atom density via optical emission spectroscopy

Because metastable-atoms are not charged, they cannot be monitored by conventional means, i.e., metastable-atoms cannot be directly detected by electrostatic probes. The majority of metastable-atom diagnostic techniques are, therefore, optical measurements. Optical measurements, however, may be limited by system geometry and cost. Metastable-atom density, for example, has been spatially and temporally resolved [*Greenburg & Hebner,* 1993; *McMillin and Zachariah,* 1995; *Millard et al.,* 1998, *Belostoskiy et al.,* 2011; *Vitelaru et al.,* 2012, *Niermann et al.,* 2010] via backlight spectroscopy, laser induced fluorescence (LIF), and laser absorption spectroscopy (LAS). These diagnostics are minimally invasive in the sense that they are optical techniques, however, these techniques usually require two optical ports on a device - one for light injection, another for radiation collection - as well as an external light source capable of probing the metastable level in question, which is not always available.

The work presented in this dissertation exploits the fact that metastable-atoms are, effectively, ground-state atoms with a smaller threshold for ionization *and excitation.* Excitation out of metastable levels is drastically different than excitation out of the ground state due to (1) the stored energy in the metastable-atom; and (2) the total angular momentum of the metastable-atom. While the former simply lowers the energy threshold for excitation, the latter changes the excitation pathways out of the metastable level and, thus, changes the optical emission spectra. The most-widely-used optical technique for monitoring metastable-atoms, optical emission spectroscopy (OES), does not require an external light source, rather, it relies on plasma self-emitted light. An emission spectrum diagnostic is non-invasive and does not require a secondary light source. DeJoseph and Demidov [*DeJoseph et al.,* 2005; *Demidov et al.,* 2006] first suggested that using the 420.1-419.8nm emission-line ratio may be used to monitor the presence of metastable-atoms in an argon plasma because the proximity of the spectral lines eliminates wavelength-dependent sensitivity corrections (e.g. quantum efficiency of a photon counter). The first quantitative

measurements of argon metastable-atom density using this technique are the result of a 2012 University of Maryland (UMd) – West Virginia University (WVU) collaboration [*Fox-Lyon et al.,* 2013] using an Ar/H_2 inductively coupled plasma (ICP). Further advancements were made during a 2013 Sandia National Labs (SNL) – WVU collaboration [*Franek et al.,* 2015; *Franek et al.,* 2016].

Drawbacks and workarounds to using emission-line-ratio techniques as a plasma diagnostic

Collisional-radiative [*Bates & Damgaard,* 1949] models have been used to model plasmas and have been tested by experimental observations over a wide range of discharge pressure (see [*Zhu & Pu,* 2010] and references [4–20] therein). Measuring several related argon emission lines may yield similarly accurate information as the 420.1-419.8nm emission-line-ratio technique if a more complex collisional-radiative model is used. While efforts have been made (see *Franek et al., 2015* and references [7–17] therein) to simplify these complex collisional radiative models for extracting diagnostic signatures without sacrificing accuracy, these simplifications still require algebraic overhead that may be eliminated. For example, while the radiation-trapping effects of the often-utilized $2p_x$-to-$1s_y$ transitions (in Paschen's notation) [*Jung et al.,* 2007] are taken into account, or even exploited [*Boffard,* 2009], the alternative to eliminating the need to account for these effects by directly observing the $3p_x$-to-$1s_y$ transitions [19] (e.g. the 420.1nm and 419.8nm emission lines) would be preferable in most cases as this simplifies the analysis [*Boffard,* 2012].

While the use of the 420.1-419.8nm emission-line ratio proved successful in past WVU collaborations [*Fox-Lyon et al.,* 2013; *Franek et al.,* 2015; *Franek et al.,* 2016], and independently at University of Wisconsin [*Boffard et al.,* 2012; *Boffard et al.,* 2015], the proximity of the emission-lines requires a high-resolution spectrometer to resolve the emission-line profiles, thus limiting the technique's availability and affordability. Furthermore, the 419.8nm emission depends sensitively on pressure [*Boffard et al.,* 2007], which may hamper the extrapolation of the technique to higher-pressure systems. This dissertation exploits the 420.1-419.8nm emission-line-ratio technique in the pressure range 0.1-10 Torr using a

high-resolution spectrometer, thus avoiding both of these limitations. Ultimately, this dissertation aims to remove both the resolution and pressure-range limitations and develop a single-line-ratio technique that can be applied by a greater number of plasma scientists. To this end, the dissertation is outlined as such:

The primary drawback to all emission techniques is the difficulty associated with understanding the atomic processes that lead to the observed emissions. To highlight the atomic processes that lead to emission, a rudimentary outline of the pertinent quantum mechanical principles governing the excited states of the argon atom, and allowed transitions between the excited states will be given in Chapter II. This chapter ends with a heuristic derivation for the expected metastable dependence of the 420.1-419.8 emission-line pair and a discussion of why the emission lines make for a good diagnostic.

The understanding outlined in Chapter II provides the theoretical basis for a newly-proposed 420.1-425.9nm line-ratio technique in argon which expands the applicability of the well-studied 420.1-419.8nm line ratio technique. The theoretical basis of predicting this technique and the experimental evidence justifying the use of this technique are given in Chapter III, which describes the corona model of plasma emission, and the extension of the model that is needed to describe non-hydrogen atoms (e.g. the noble gasses). The corona model introduces excitation rate coefficients that correlate plasma excitation dynamics to the electron energy distribution (EED).

Chapter IV details the experimental procedure and configuration. The design, construction, and operation of the argon pulsed positive column, studied here, is discussed. A constant, negative voltage from the power supply provides the negative reference voltage to a pulser. The pulser is connected in series to the cold cathode electrode via the Pulse Conditioning Circuit (PCC). The description of the vacuum system that allows the plasma to form is discussed. A digital delay generator (DDG) is used to synchronize the plasma generation timing with the plasma diagnostics timing.

In Chapter V, typical data from the experiment described in chapter IV are interpreted. A physical interpretation of a typical microwave cavity resonance

spectroscopy (MCRS) is offered, rudimentary behaviors of the metastable-atom population is uncovered, corrections to obtain the plasma-current waveform are discussed, and the anomalous behavior of the emission spectra is explained.

In Chapter VI, the relative intensity of argon emission lines is used to help understand the dynamic nature of atomic kinetics in an argon positive column. The 420.1-419.8nm line ratio is used to empirically define three distinct stages of the discharge: the Initiation Stage, the Transient Stage, and the Post-Transient Stage. From this understanding, a qualitative understanding of dominant excitation and relaxation processes can be formulated. This prompts a quantitative study of the three stages individually, which allows us to detect a supra-thermal electron population in the Initiation stage, determine metastable-atom density in the Post-Transient stage, and estimate reduced electric field in the pulsed positive column.

II. Background

In this chapter, quantum mechanical properties and characteristics of excited states of the noble gasses are discussed. Electron collision-induced excitation of argon atoms is then discussed in detail. The three excitation mechanisms (Dipole-allowed singlet excitation, Dipole-forbidden triplet excitation, and radiative cascade population) for populating excited states are distinguished. Three types of electron-impact cross-sections (direct, apparent, and optical) are distinguished. The three types of electron-impact cross-sections are used to heuristically derive an expression for the 420.1-419.8nm emission-line ratio.

Valence-shell electron structure in excited states of the noble gasses

In argon, promoting one electron from the $(3p)^6\ {}^1S_0$ ground state into the nearby (4s) level results in excited states with electron configuration $(3p)^5(4s)^1$. The total angular momentum of the electron-hole–electron pair add together (couple) to form the four levels of the $1s_x$ manifold. The four predicted states J=1, 0, 1, 2 are empirically labeled $1s_2$, $1s_3$, $1s_4$, and $1s_5$, respectively, in Paschen's notation where $1s_2$ is the most-energetic of the four states, $1s_3$ is the second-most energetic and so forth. The Russel-Saunders coupling scheme, on the other hand, may be used to posit term-symbols ${}^1P_1$, ${}^3P_0$, ${}^3P_1$, and ${}^3P_2$ which are sometimes (regrettably) used to describe the four states. While quantitative knowledge of the energy levels cannot be acquired by knowledge of angular momenta alone, a qualitative picture of the energy level sequence sometimes may be constructed by invoking the various coupling schemes. The utility of various coupling schemes are discussed in appendix I.

Promoting one of the $(3p)^6\ {}^1S_0$ electrons into the next highest level results in excited states with electron configuration $(3p)^5(4p)^1$.The electron-hole–electron pair couple to form the ten levels of the $2p_x$ manifold. Hund's rules for Russel-Saunders coupling produces term symbols ${}^1S_0$, ${}^1P_1$, ${}^1D_2$, ${}^3S_1$, ${}^3P_0$, ${}^3P_1$, ${}^3P_2$, ${}^3D_1$, ${}^3D_2$, and${}^3D_3$. Only the ${}^3D_3$ Russel-Saunders state is a pure triplet state and corresponds exactly to the observed $2p_9$ Paschen state. The nine other levels display some properties of a mixed state. Promoting one of the $(3p)^6\ {}^1S_0$ electrons to the s or p orbitals of higher principal quantum number *n* produce the same energy level structures and term symbols; thus, the ${}^3D_3$ Russel-Saunders term-symbol also describes the Paschen $3p_9$ state, which produces the argon emission-line at 420.1nm.

Excitation mechanisms in argon and their applications to electron-impact cross-sections

According to the collisional-radiative model, the primary source for excited atomic states are electron-impact excitation collisions. Generally, electron-collision-induced excitation of atoms follow the dipole-selection rules of quantum mechanics [*Boffard et al.,* 2007] because Coulomb interactions are mediated by

photon exchange. Dipole-allowed ($\Delta J = 1, or\ \Delta J = 0\ if\ J \neq 0$) electron-impact excitations of the form

$$e^- + Ar \rightarrow e^- + Ar^r \tag{2.1}$$

occur readily in atomic systems, where Ar is a ground state argon atom (J=0), and Ar^r is a resonant-state(*J=0*) argon atom. e^- represents the incident electron. The cross-section profiles for these kind of excitations peak for incident electron energies ~4x greater than their onset energy [*Boffard et al.,* 2004] and have a very broad energy dependence. Singlet excitation is exemplified by direct excitation of the $4d_2$ state of argon [*Boffard et al.,* 2007] as displayed in figure (2.1). Excited-states with a significant singlet component exhibit the singlet excitation profile due to dipole excitation from the ground state.

On the other hand, pure triplet states (e.g. the $3p_9$ state of argon, term-symbol $^3D_3$) have no singlet component in their wavefunction. The triplet-excitation profile is dominated by *electron-exchange* collisions. The electron-exchange peak is not as prominent in singlet-excitation profiles because this excitation mechanism favors the production of triplet states (S=1) [*Hanne & Kessler,* 1976; *Hanne,* 1976]. This mechanism should be thought of as a two-step process where 1) the incident electron ionizes the ground state argon atom, and 2) the electron recombines the argon ion, forming an excited-state argon atom [*Sharpton et al.,* 1970]

$$e^- + Ar \rightarrow Ar^+ + 2e^-, \tag{2.2}$$

$$Ar^+ + 2e^- \rightarrow e^- + Ar^*, \tag{2.3}$$

where Ar^+ is the argon ion and Ar* is an argon excited-state atom. Since electron-ion recombination is not an atomic transition, the dipole selection rules need not apply. In this way, the coupling between the initial and final wavefunctions do not affect the transition probability for electron-exchange excitation. The cross-section profile for this excitation route peaks near the ionization energy of the atom (~16eV for argon) and falls off quickly for higher energies. This process is exemplified by the cross-section for the $2p_9$ level of argon shown in figure (2.2).

Spin-orbit coupling of the argon atom often mixes wavefunctions of the same angular momentum J, and few pure states exist. Therefore, the dipole selection rules for Russel-Saunders coupled atoms are routinely violated. While

Paschen states may (wrongly) be attributed to a single Russel-Saunders state [*Stewart & Smith,* 2002], any excited state in a mixed-coupling atom should be treated as a superposition of allowed Russel-Saunders states of similar J [*Sharpton et al,* 1970]. The J=1 Paschen states in argon, e.g. the $3p_2$ state, are properly described by a superposition of Russel-Saunders terms of J=1 [*Boffard et al.,* 2004] and should be represented as

$$|3p_2\rangle = \alpha|^3S_1\rangle + \beta|^1P_1\rangle + \zeta|^3P_1\rangle + \eta|^3D_1\rangle \quad (2.4)$$

Nine of the ten wavefunctions in the 3p manifold of argon have a singlet component which may contribute to an enhanced high-energy tail in many excitation cross-section profiles, as exemplified by the $3p_2$ state of argon [*Boffard et al.,* 2007] seen in figure (2.3). The peak in these cross-section profiles, however, are still dominated by the electron-exchange mechanism. Both excitation mechanisms (dipole excitation and electron-exchange collisions) are often included when sources report "direct cross-sections."

While direct excitation of an excited state (by either of the mechanisms outlined above) is dominant for most states, another excited-state populating mechanism is radiative cascades. An excited state may relax via photon emission and decay into a lower-lying excited state at its respective rate of spontaneous emission (the Einstein coefficients A_{21}). This also serves as a population mechanism for the lower state *1*. If direct excitation by dipole-allowed excitation and electron-exchange collisions are both relatively small, the cascade component of excitation may be readily observed in optical emission cross-section profiles as exemplified by the optical emission cross-section profile of the $3p_5$ state of argon in figure (2.4).

Unlike electron-exchange collisions and dipole-excitation mechanisms, cascade population mechanism is system dependent. The cascade correction depends on the population of other states in the system, and has strong pressure and energy dependencies. To address these dependencies, a first-order correction for cascade effects may be made by using optical emission cross-sections in calculating excitation rates [*Boffard et al.,* 2004]. 'Direct' cross-sections that have corrections for radiative cascades are known as 'apparent cross-

sections'. Apparent cross-sections are often measured by the 'optical method' of observing wavelengths λ_{ij} (corresponding to relaxation from the excited state *i* into lower state *j*). These cross-sections, when reported in their raw form, are referred to as 'optical emission cross-sections' because the branching ratio out of the excited state *i* is included.

The 'double-humped' profile exhibited in figure (2.4) can usually be observed in optical emission cross-sections for the np_7, np_5 and np_1 states, where n is the principal quantum number of the outermost electron. Normalized optical emission cross-section profiles for the $3p_7$, $3p_5$ and $3p_1$ states of argon are shown in figure (2.5). The $3p_5$ state has the largest relative cascade contribution; the cascade-peak is 82% of the peak due to electron-exchange collisions. The $3p_7$ and $3p_1$ states have cascade-peaks at 78% and 67%, respectively. The other seven states in the $3p_x$ manifold lack a well-defined cascade peak.

Applying excitation dynamics of the $3p_x$ manifold to the extended corona model

The extended corona model [*Boffard et al.,* 2010] (to be discussed in chapter III) indicates the observed photon flux ϕ_{ij} due to relaxation from an upper state i into a lower state j may be produced by electron-impact excitation of any state l at a rate k_{ij}^{l},

$$\phi_{ij} = K n_e \mathcal{R}_{ij} \sum_l n_l k_{ij}^{l}, \tag{2.5}$$

where the summation over l includes all argon states. n_l is the target atom density, (n_o is the ground-state density), n_e is the electron density, K is a constant that includes geometric and conversion factors associated with the collection of the emitted light, and $\mathcal{R}_{ij}$ is the correction factor for line-specific effects that depend on plasma optical thickness.

Previous works by the Boffard group include five states in equation (2.5), the ground state ($l = o$) and the four states from the $1s_x$ manifold, to obtain densities of the four excited states through effective branching ratios. While all of the excited states of argon must be included in equation (2.5) for the equality to be valid, the works performed by Boffard's group have implied that the inclusion of only four intermediate states are sufficient to accurately describe the emission dynamics of the $2p_x$ manifold in a low-temperature argon plasma. A major implication of the

analysis in this section of this dissertation is that only one intermediate state needs to be considered when describing the dynamics of the $3p_x$ manifold.

The summation over states l in equation (2.5) indicates that any number of states $l<i$ may be included to account for other excited states between the ground state o and the emitting state i. Well-informed choices of emission-lines and correlations between plasma parameters can reduce the experimental requirements down to two observed emission-lines. It is evident that observed photon flux is influenced by many plasma parameters including electron density (n_e), atomic species densities (n_l), and the electron energy distribution ($f(e)$). Straightforward algebra says that n equations are necessary (emission-lines need to be observed) in order to solve for n variables (quantify n-many plasma parameters). Here, limiting the analysis to lines that only show dependence on one excited state l means that only two emission lines need to be observed to make meaningful correlations between plasma parameters.

Knowledge of excitation rate dynamics allows one to make an informed choice of emission lines that will be fruitful. The greatest simplification of equation (2.5) results from a smart choice of emission lines. DeJoseph and coworkers [*DeJoseph et al.,* 2005; *Demidov et al.,* 2006] previously identified the 420.1-419.8nm emission-line ratio as a prime candidate for determining metastable-atom density. The 420.1nm emission-line comes from the $3p_9$ excited state. The $3p_9$ excited state (J=3) may dipole decay only by photon emission into a lower excited state of J=2 (there are no states below the $3p_9$ state with J=3 or J=4). This leads to a branching factor near 25% (and a bright emission line). The $3p_9$ state is a pure triplet state ($^3D_3$) and therefore only has a substantial direct excitation from the electron-exchange collision. Total spin J=3 of the excited state allows for stepwise excitation from the J=2 $1s_5$ metastable state of argon.

The 419.8nm emission-line comes from the $3p_5$ state that has significant population from the electron-exchange process and from radiative cascades. It is crucial that optical emission cross-sections are used in this case because they account for the population from radiative cascades. Total spin J=0 only allows for stepwise excitation from the J=1 resonant states, which usually have low enough

density to ignore. Stepwise excitation from the metastable states (J =0, 2) are dipole forbidden and ignorable as well.

Heuristically, the intensity of the 420.1nm and 419.8nm emission-lines can be written as

$$I_{420} = n_o * e^{-}exchange + n_m * stepwise, \text{ and} \quad (2.6)$$

$$I_{419} = n_o * e^{-}exchange + n_o * cascades, \quad (2.7)$$

where *e⁻exchange, stepwise,* and *cascades* represent the population mechanisms outlined above. The observed emission ratio is then

$$Ratio = \frac{I_{420}}{I_{419}} = \frac{n_o * e^{-}exchange + n_m * stepwise}{n_o * e^{-}exchange + n_o * cascades}. \quad (2.8)$$

If the population of the $3p_5$ level due to radiative cascades is smaller than the electron-exchange component, the above equation simplifies to

$$Ratio \sim \frac{n_o * e^{-}exchange}{n_o * e^{-}exchange} + \frac{n_m * stepwise}{n_o * e^{-}exchange},$$

$$Ratio \sim 1 + \frac{n_m}{n_o} \frac{stepwise}{electron-exchange}. \quad (2.9)$$

Ignoring the effect of radiative cascades (even for the $3p_5$ level) is a plausible assumption, considering the effect is seen only for high energy (E>80eV) electrons, which comprises a very small percentage of the electron population. The emission ratio will always be an observed quantity in this work because n_M/n_o contains information about the metastable-atom density and the quotient (stepwise/e⁻exchange) contains information about the EED. Thus, observation of the emission ratio and the metastable-atom density may yield information regarding the EED or observation of the emission ratio and the EED may yield information regarding the metastable-atom density.

III. The Extended Corona Model, and Predicting Emission-Line Intensities.

In the first section, the coronal approximation for plasma-emission is discussed. In this model, photon re-adsorption is insignificant and electron-collision-induced re-excitation of excited states do not occur. The only depopulation mechanism for an excited state is relaxation via photon emission. Observed emission-line intensity is related to excitation rate of excited states, which depend on the electron energy distribution (EED). This model is 'extended' by including stepwise excitation (re-excitation) from the argon metastable-atom which favors 420.1nm emission. The intensity of the 420.1nm emission-line (and ultimately, the 420.1-419.8nm emission ratio) can then be related to the metastable atom density n_M and the electron energy distribution (EED).

In the second section, the emission line at 425.9nm is suggested as a surrogate for the 419.8nm emission line. Theoretical and empirical arguments for the validity of this technique are offered, and the relation between the emission-lines is explored qualitatively. Electron-impact cross-sections for the $3p_1$ and $3p_5$ states suggest the 425.9-419.8nm emission-line ratio depend on the shape of the EED.

The corona model, and the inclusion of metastable-atoms

In coronal equilibrium, the spontaneous decay out of the excited state *i* is equal to the electron-collision-induced excitation of ground state atoms into the excited state [*Cooper,* 1966]

$$\sum_j n_i A_{ij} = n_o n_e k_i^o, \tag{3.1}$$

where the ground-state density, excited-state density, and electron density are n_o, n_i, and n_e, respectively. A_{ij} is the rate of spontaneous decay from state i into state j (Einstein coefficient) and the sum over all states j ensures all relaxation routes via photon emission into lower states j are considered. k_i^o is the excitation rate coefficient describing electron-collision-induced excitation from the ground state o into excited state i and is given by [*Adams et al.,* 2009; *Boffard et al.*, 2010]

$$k_i^o = \int_0^\infty \sigma_i^o(\varepsilon) \left(\frac{2\varepsilon}{m_e}\right)^{1/2} f(\varepsilon) d\varepsilon, \tag{3.2}$$

where σ_i^o is the cross-section for electron-impact excitation from the ground state o into state i, ε is the incident electron energy, m_e is the mass of the electron, and $f(\varepsilon)$ is the EED.

In its current form, experimental implementation of equation (3.1) would be quite tedious. Higher-lying states of argon, such as the $3p_5$ state for example, can decay into multiple lower states, as depicted in figure (3.1). Measuring all of the wavelengths resulting from decay of a $3p_5$ atom usually require two spectrometers (one for visible light, another for infrared light) with absolute intensity calibrations [*Chilton et al.,* 1998]. Equation (3.1) is greatly simplified, however, by choosing a specific final state j for each excited state i. The excitation rate coefficients in equation (3.2) can be assigned to a particular emission line by including the specific $i \rightarrow j$ branching ratio on the right hand side of equation (3.2). The branching ratio for any upper state i into a lower state j can be estimated by

$$\Gamma_{i\rightarrow j} \approx A_{i\rightarrow j}\tau_i, \tag{3.3}$$

where τ_i is the characteristic lifetime of upper state i. The characteristic lifetime τ_i measurements of states in the $3p_x$ manifold are tabulated in [*Klose,* 1968], and are on the order of 100ns for all states of the 3p manifold. The photon flux, ϕ, for a

specific $i \rightarrow j$ transition $\phi_{i\rightarrow j} = n_i A_{i\rightarrow j}$, in terms of this modified excitation rate coefficient $k^o_{i\rightarrow j}$ state, is now

$$\phi_{i\rightarrow j} = n_o n_e k^o_{i\rightarrow j}. \quad (3.4)$$

The photon flux of wavelength 419.8nm from the $3p_5 \rightarrow 1s_4$ transition (hereby denoted by the photon wavelength as $\phi_{419.8}$) can be used to monitor the modified excitation rate (hereby denoted by the photon wavelength as $k^o_{419.8}$). The $3p_5$ state has characteristic lifetime 98ns [*Klose,* 1968], and the $3p_5 \rightarrow 1s_4$ transition has spontaneous excitation rate $2.57 * 10^6 Hz$, which leads to a branching ratio of 25% via equation (3.3). Thus the modified excitation rate in equation (3.4) is simply $k^o_{419.8} \approx 0.25 * k^o_{3p5}$. Since decay out of the excited states i is spontaneous, the density of any excited state i is expected to be small enough that collisions with excited state atoms may be ignored.

While using the coronal-equilibrium model is convenient for low-pressure plasma, describing argon at higher pressure requires an extended corona-equilibrium model [*Zhu & Pu*, 2010, *Boffard* e*t al.,* 2010] by including stepwise excitation from excited states *l* that are energetically below the excited state *i*. The photon flux at wavelength λ_{ij} [*Boffard et al.,* 2010] is expressed as

$$\phi_{ij} = K n_e \mathcal{R}_{ij} \sum_l n_l k^l_{ij}, \quad (3.5)$$

where K is a constant that includes geometric and conversion factors associated with the collection of the emitted light, and $\mathcal{R}_{ij}$ is the correction factor for line-specific effects that depend on plasma optical thickness. In the simplest case, where only the ground state is considered ($l = o$) and experimental corrections are ignored ($K, \mathcal{R}_{ij} \rightarrow 1$), equation (3.5) is simplified and equation (3.4) is recovered. If a second state l=m is considered, equation (3.5) has a second source term. The excitations from both states l=o, m are depicted in figure (3.2).

Perhaps the most problematic term in equation (3.5) is the summation over plasma excited species. While most excited states readily depopulate by photon decay out of the level, the densities of excited species will grow in a high-pressure discharge and it is more likely that excited states are re-excited by an electron collision. Thus, even collisions with resonant states (states with J =1) should be

considered [*Boffard et al.,* 2009; *Boffard et al.,* 2010; *Boffard et al.,* 2012] when modeling a high-pressure discharge. An in-depth analysis of the excited states of the noble gasses, as provided in chapter II, however, greatly simplifies equation (3.5) and removes much of the algebraic bookkeeping inherent in modeling several excited states.

The modeling of *Adams et al.* leads to an expression similar to equation (2.9), albeit by a more-exact numerical treatment of the plasma. The excitation rates depend on the various cross-sections and the EED and must be calculated numerically. Equation (3.5) is simplified if stepwise excitation to an upper state i has a negligible rate compared to direct excitation to the state, i.e., there is only one source term in equation (3.5), as is the case for the $3p_5$ state that produces 419.8nm emission. The stepwise excitation rate from the $1s_5$ metastable-atom state into the $3p_5$ state leading to 419.8nm emission ($k^M_{419.8}$) is much smaller than the corresponding direct excitation rate ($k^o_{419.8}$) and is ignorable in the regime discussed here. Note that $k^o_{419.8} \approx k^o_{420.1}$ [*Adams et al.,* 2012] and is not included in figure (3.3) for clarity. Assuming the ratio of the radiation trapping terms to be unity and the geometrical factors *K* are wavelength independent, equation (3.5) may be used to obtain an expression for the observed emission-line ratio

$$R = \frac{I_{420.1}}{I_{419.8}} = \frac{k^o{}_{420}(f(\varepsilon))}{k^o{}_{419}(f(\varepsilon))} + \frac{n_m}{n_o}\frac{k^m{}_{420}(f(\varepsilon))}{k^o{}_{419}(f(\varepsilon))} = 1 + \frac{n_m}{n_o}\frac{k^m{}_{420}(f(\varepsilon))}{k^o{}_{419}(f(\varepsilon))}. \qquad (3.6)$$

Different approaches to solving this ratio have been reported in the literature. The analysis in [Boffard et al., 2010; Boffard et al., 2012] uses a “two-parameter” EED based on electron temperature and a variable fitting parameter while the numerical analysis in [Adams et al., 2012] considers limiting cases of metastable-atom density nM, and electron density ne to approximate bi-Maxwellian EEDs. These bi-Maxwellian EEDs are then used in equation (3.2) to produce a large array of excitation rates k^I_{ij} as functions of reduced electric field E/N published in Adams et al. [2012]. Select excitation rates are reproduced in figure (3.3). Here the states i and j are replaced by the wavelength of their transition in nanometers for brevity.

This expression for observed emission-line ratio now explicitly depends on normalized metastable-atom density and, through the excitation rate ratio,

implicitly on metastable-atom density, electron density, and reduced electric field. Because the last term in equation (3.6) is always positive, the line ratio, in principle, cannot be less than unity, which is always the case in the post-transient stage of the pulse discussed in this dissertation.

Making the case for the 420.1-425.9nm emission-line ratio

While the 420.1-419.8nm emission-line ratio can be used [*Fox-Lyon et al.,* 2013; *Franek et al.,* 2015; *Franek et al.,* 2016] to determine metastable-atom state density, the proximity of the emission-lines require a high-resolution spectrometer to isolate the emission-lines. Furthermore, the cross-section of the $3p_5$ state (the upper state producing 419.8nm emission) has been shown to have a severe pressure dependence [*Boffard et al.,* 2007]. Both of these factors make it troublesome when extrapolating this line-ratio method in higher pressure systems. The $3p_5$ state, in fact, has the largest (normalized) cascade contribution of the $3p_x$ manifold as seen in figure (2.5). Ideally, the 419.8nm emission-line would be replaced with another emission line that 1) retains (or even improves) the convenience of the 420.1nm, 419.8nm line-pair in theory and in practice (i.e. equation (3.6) remains valid), and 2) mitigates the sensitivity to chamber pressure.

The simplifications leading to equation (3.6) require the intensity of the emission-line in the denominator be dominated by direct excitation, i.e. stepwise excitation into the upper state must be negligible. The stepwise excitation mechanism is well-described by the dipole selection rules as described in chapter II. Specifically, excited states may be readily populated by stepwise electron-collision excitation of a metastable-atom if the transition is dipole allowed ($\Delta J = 1, or\ \Delta J = 0\ if\ J \neq 0$). The $1s_3$ state (J=0) may therefore readily excited into any state of J=1 and the $1s_5$ state (J=2) may readily excite into any state of J=1,2,3. The only excited states of argon that are not readily populated through stepwise excitation of metastable-atoms are states of J=0. The only two excited states of J=0 in the 3p manifold are $3p_5$ (which we are trying to replace) and the $3p_1$ state. The arguments outlined above, which suggest that the $3p_5$ state is useful for observing direct excitation of an argon atom, hold true for the excitation of the $3p_1$

state as well. With appropriate modeling, emissions resulting from the $3p_1$ state may therefore be used as a proxy for the 419.8nm emission.

The $3p_1$ state (J =0) may radiatively decay to the $1s_4$ and $1s_2$ states by emitting a photon of wavelength 398.0nm or 425.9nm respectfully. The former transition is spectrally removed from the wavelengths of interest (which would complicate analysis) and is a 'weak' emission line (the branching ratio is less than 1%) [*Weber et al.,* 2003]. The 425.9nm emission, however, is relatively close to the wavelengths of interest and is (empirically) as intense as the 419.8nm emission. The 425.9nm emission-line may be experimentally easier to use because it is spectrally isolated from neighboring argon emission lines. The nearest argon atomic emission-line is 0.7nm away at 426.6nm. Thus, resolving the argon emission line at 420.1nm with sufficient accuracy implies the 425.9nm emission line will be sufficiently resolved as well. The 425.9nm emission-line may replace the 419.8nm emission-line in the 420.1-419.8nm line ratio technique if the relation between the 425.9nm emission-line and 419.8nm emission-line is quantified. According to equation (3.2), the only variable that relies on the emission-line of interest itself are the excitation cross-sections. Understanding the relation between these cross-sections allows for one to predict the relative intensity of the emission-lines themselves.

Optical emission cross-sections at 1-Torr for the emission lines of interest of this work are given in figure (3.4), where the background shading indicates the region in energy-space where incident electrons are more likely to induce 425.9nm emission than 419.8nm emission. Thus, increasing the number of electrons in this region would increase the 425.9-419.8nm emission-line ratio, while increasing the number of electrons in the unshaded regions decrease the 425.9-419.8nm ratio. Notice that the lowest energy electrons (up to 16eV) preferentially induce 419.8nm emission; this population is responsible for the 425.9-419.8nm emission-line ratio below unity for low E/N. Intermediate energy-range electrons (16eV-30eV) are more likely to induce 425.9nm emission; thus, increasing the number of electrons in this range will increase the 425.9-419.8nm emission-line ratio. Incident electrons with energy greater than 30eV will preferentially induce 419.8nm

emission; this effect, however, is not believed to be significant in this series of experiments.

Considering optical-emission cross-sections only, it should be expected that the intensity of the 419.8nm emission line is greater than the intensity of 425.9nm emission because the bulk of the plasma electrons have energy less than 16eV. ‘Heating’ the distribution may increase the 425.9-419.8nm emission-line ratio if the electron population between 16 and 30eV increases.

Chapter IV: Experimental Device, Diagnostics, and Methodology:

In this chapter the design, construction, and operation of the argon pulsed positive column studied here is discussed. A constant, negative voltage from the power supply supplied the negative reference voltage to a pulser. The pulser is connected in series to the cold cathode electrode via the Pulse Conditioning Circuit (PCC). The description of the vacuum system that allows the plasma to form is discussed. A digital delay generator (DDG) is used to sync the plasma generation with the plasma diagnostics.

In the second section of this chapter, the apparatus required for Optical Emission Spectroscopy (OES), and Tunable Diode Laser Absorption Spectroscopy (TDLAS) are outlined. Measurement of plasma current density is used to determine reduced electric field in the positive column region.

Configuration

In the Sandia experiment, a cold cathode is biased negatively to strike a plasma discharge between the cathode and a grounded (anode) electrode. The experimental setup is given in figure (4.1) and the details of its construction will be discussed in this chapter. The various components of the setup are explained in detail here. Typical, normalized, electron densities are approximately $n_e/n_o \sim 1 * 10^{-6}$ regardless of the pressure explored here. For experiments at 1 Torr this equates to an absolute electron density $n_e \sim 3 * 10^{10}\ cm^{-3}$. Metastable argon atom density is on the same order of magnitude for the experiment described here.

Power delivery

The plasma can be generated in the region of interest by two pulsing methods: single-pulse or double-pulse. The advantages of the double-pulse method will be presented later in this chapter, whereas the details of the experimental implementation of the double-pulse method are recorded here. In the single-pulse experiments, the voltage pulse is generated by a Bertain Series-105 1kW-Power Supply. The power supply is typically operated in current-limited mode at 7.2mA (~-0.93kV). The applied voltage may vary from day-to-day operation by less than 1%. The negative voltage output of the power supply is connected to the negative voltage input of a DEI PVX 4140 High Voltage Pulser (henceforth referred to as the pulser), which supplies a negative voltage pulse to the cold cathode of the discharge. The positive high-voltage input of the DEI pulser is grounded.

The pulser has two high-voltage inputs, one high-voltage output, and an external trigger input. The sign and the magnitude of the voltage at the output of the pulser is determined by the TTL signal at the external trigger input (0 or 5 Volts) and the magnitude of the voltage applied to the high-voltage inputs. By default, the pulser transfers the voltage at the negative high-voltage input when the TTL signal at the external trigger input is “low” (grounded), and transfers the positive high-voltage input when the TTL signal at the external trigger input is “high” (+5V). This default, however, is not adopted as the chosen operational mode for to the negative pulse studied here. The reverse convention is adopted here by soldering

together pins numbered 10 and 13 in the remote access port in the back of the pulser. In this configuration, a positive trigger signal to the pulser applies the voltage at the negative high-voltage input to the pulser output, and a grounded trigger signal transfers the voltage at the positive high-voltage input (ground) to the pulser output. The output of the pulser is connected to the first input of the Pulse Conditioning Circuit (PCC).

Pulse conditioning circuit (PCC)

The Pulse Conditioning Circuit (PCC) , shown in figure (4.2), is a simple electrical circuit, similar to a matching network of a RF plasma device, which helps monitor the input signal to the system and mitigate reflected signals (i.e., prevent signal reflections from damaging the pulser(s)). The elements are described in order starting from the input from the pulser and ending with the output to the cold cathode.

Input signal(s) from the pulser(s) pass through a Zener diode which is used to prevent reflected signal from reaching pulser(s) and reduce the likelihood of electrical damage. Two, 1000 Ohm, 10Watt ballast resistors in parallel (~500 Ohm equivalent resistance, 20 Watt equivalent maximum Wattage) are used to limit current spikes resulting from plasma breakdown (i.e., dramatic increases in conductivity). At this point, the conditioned signals from the inputs of the PCC are combined to form a single waveform. A 50 MOhm resistor and 500 kOhm resistor form the voltage divider which is used to yield a voltage signal approximately 100X less than the applied voltage that can be digitized by the oscilloscope. A 1Volt/1Amp Pearson current transformer is used to measure the transmitted current. Note, the current waveform measured here is not the plasma current. A method for subtracting displacement current from the raw signal is outlined in a later section. The PCC output is delivered to the cold cathode via SHV or MHV high-voltage cables.

Vacuum hardware and gauges

A detailed view of the Vacuum system is given in figure (4.3). The experimental apparatus consists mainly of 2 ¾" diameter stainless steel ConFlat-style (CF) hardware. Viton gaskets are used to seal the CF hardware unless

explicitly noted otherwise. The main discharge chamber is a 1”OD Pyrex tube that confines the positive-column region of the plasma and is supported on both ends by 2 ¾” diameter CF–to–Ultra-Torr fittings.

A Microwave Resonant Cavity (MRC) surrounds the plasma of interest to ensure that the optical diagnostics sample the same plasma region. The aluminum MRC dimensions (outer radius of 57mm, and length 32mm) are chosen such that only the TM_{010} mode is present in the MRC. The cavity has radial access ports to allow the other optical diagnostics (OES, TDLAS) to sample the same plasma. The technique of Microwave Cavity Resonance Spectroscopy (MCRS) will be discussed later in this chapter.

The Ultra-Torr fitting on the high-voltage side (left side of figure(4.3)) of the chamber is connected to a 2 ¾” diameter CF viewport for viewing the r-θ plane of the plasma. The metal body of this flange is connected to the PCC by a high-voltage SHV cable and acts as the cold cathode that produces the positive column. To avoid electrical shock, the cold cathode is surrounded by a Faraday shield made of a grounded aluminum probe box.

The Ultra-Torr fitting on the grounded side of the main discharge chamber is directly connected to two radial 1.33” diameter (“mini”) CF flanges (not shown) used for introducing gas into the chamber and for a Pfeiffer Pirani gauge. Argon gas flow into the system is adjusted and monitored by a MKS flow-meter up to the maximum rate of approximately 50 standard cubic centimeters per minute (sccm). In most experiments, the flow is set to 50 sccm to maximize the purity of the plasma. A 2 ¾” diameter three-way CF tee is used to connect a Bellows-sealed valve, used to regulate the chamber pressure, followed by a scroll-type pump. The final vacuum fitting on the grounded side of the apparatus is a 2 ¾” diameter CF viewport which allows an axial view of the discharge. The base pressure routinely equilibrates below the lower limit, $5.0*10^{-4}$ millibar, or 0.38 milliTorr, of the Pirani gauge.

Digital delay generator (DDG)

Precision in synchronizing the pulsed positive column and the diagnostics is paramount for interpretive accuracy in this work. To attain nanosecond

precision, a Stanford Research Systems model DG 645 Digital Delay Generator (DDG) is used to synchronize all of the measurements in the experimental setup via a LabVIEW interface. The DDG creates four, five-volt square-wave voltage pulses labeled A-B, C-D, E-F, and G-H; the duration of these pulses are controlled by defining the four start-time points (A, C, E, and G) and their respective end-time points (B, D, F, and H). Each time-point may be set with respect to the internal clock of the DDG, to another time-point, or to an external waveform. The three output waveforms used in the single-pulse experiments are shown in figure (4.4).

Channel A-B is dedicated to triggering the oscilloscope. Time-point A is set to a specific delay *after* the DDG's internal clock (t=0) to trigger the oscilloscope. Time-point B is then defined as B=A+10μs to create a 10μs-duration voltage pulse as shown in figure (4.4). This insures that the pulse that triggers the oscilloscope can be recognized by the oscilloscope. Channel E-F is dedicated to triggering the first pulser, which then creates the plasma-generating voltage pulse. Time-points E and A are coincident and the duration of the plasma-creating voltage pulse is determined by time-point F. A 20μs pulse, typical of the single-pulse experiments, is achieved by setting F=E+20μs.

Channel C-D is dedicated to triggering the camera by creating a standard 5V, 5μs duration TTL pulse (D=C+5μs). Camera shutter duration, however, is independent of the triggering voltage waveform and controlled within the camera software. To allow for a background image to be collected for each measurement, a null image is acquired before the primary pulse by starting the data acquisition at time t=E-400ns. To ensure proper operation of the DDG, time-points A and E are set to a specific time after the DDG's internal clock to ensure the voltage pulse from channel C-D is always after the DDG's internal clock trigger at time t=0.

Typically, time-point C is initialized to C=E-400ns (400ns before time-point E) when collecting images at 200ns resolution. This allows for the LabVIEW program to shift its interrogation-time to t=E-200ns, take an image (which will be utilized as a background image in post-processing), and shift its interrogation-time to 0ns (the exact time the plasma is pulsed). This allows the second image in the experimental trial taken from 0-200ns to be background-corrected. This

interrogation-time shift procedure is repeated until spectra from the duration of the voltage pulse are captured.

In the double-pulse experiments, channel G-H is used to trigger the second high-voltage pulser (henceforth referred to as the “plasma-conditioning pulse”). The four output waveforms for the DDG are shown in figure (4.5). The plasma-generating pulse is shortened to 7μs (F=E+7μs) and time-point G is set to G=E+50μs to ensure the plasma-conditioning pulse is triggered 50μs after the plasma-generating pulse is initiated. Time-point H is set to H=G+10μs to ensure the plasma-conditioning pulse is 10μs in duration. To allow for a background image to be collected in the double pulse experiments, a separate background image is taken before the plasma-generating voltage pulse to ensure residual photons from the afterglow of the plasma-generating voltage pulse are not included in the background.

Optical emission spectroscopy (OES)

To collect plasma emission spectrum from the plasma region of interest at each time-point as defined by the DDG, light is collimated and sent through a 200 μm diameter optical fiber. The transmittance of the fiber for the near-ultraviolet wavelengths examined here, although negligible, is considered when measuring the transmittance of the entire system (collimators, fiber, and monochromator) in the blackbody calibration explained later in this section. Light from the fiber is directed into the 150μm slits of a Jobin Yvon HR 460 monochromator using a second collimator. The image of the entrance slit is collimated by the first mirror of the monochromator, dispersed (perpendicularly to the slit’s longest dimension) by a 2400 grooves/mm diffraction grating, and re-focused by the second mirror of the monochromator on the input window of an Andor iStar ICCD camera. The monochromator has a spectral dispersion of 0.88nm/mm when equipped with the 2400 groove/mm grating; the monochromator-ICCD system has a combined dispersion of 0.00935nm per pixel.

Plasma emissions in the range of 415-430nm (using the 2400groove/mm grating) are imaged by an Andor iStar ICCD camera. Location, amplitude, and relative amplitude of these spectral peaks are then examined to help determine

plasma properties. Typically, only seven neutral argon emission lines are present in the OES data; however, observation of other non-argon emissions helps monitor the purity of the discharge. No argon ion lines are observed.

The efficiency (i.e., transmittance) of the collecting, transmitting, dispersing, and measuring elements in the OES-setup must be accounted for before meaningful interpretations of OES data may be made. To do this, a tungsten blackbody source, controlled by an OL65A Programmable Current Source (Optronic Laboratories, a Gooch & Housego company) operated at 6.500A, 31.50V, 204.8W, 5,000K, is observed by the OES setup described above, and compared to the theoretical blackbody curve to obtain the transmittance function of the setup. The transmittance function shown in figure (4.6) is normalized such that the transmittance at the 420.1nm line is unity.

The observed transmittance function of the system is typical for a spectrometer. The primary source of wavelength-dependent (energy-dependent) attenuation of the optical path is the diffraction grating. The expected transmittance from a holographic diffraction grating is shown in figure (4.7 typical). The expected transmittance of a diffraction grating is highest at the blaze wavelength λ_B and falls off gently towards longer wavelengths [*Palmer,* 2005]. The 2400groove/mm diffraction grating used in this experiment is blazed at 400nm, and we expect to see a slight drop-off in transmittance at the longer-wavelength end of the spectrum as seen in figure (4.6).

Tunable diode laser absorption spectroscopy (TDLAS)

Argon excited-state density is determined by Tunable Diode Laser Absorption Spectroscopy (TDLAS). A New Focus model 6200 Tunable-Diode laser produces laser light between 790-820nm, with sub-angstrom precision, which is used to provide the precise energy for an excited state of argon to be further excited into a higher-energy state. A schematic of the laser path is given in figure (4.8); each of the elements of the figure are discussed here.

Laser light emitted from the laser diode first passes through an optical isolator which prevents damage to the laser by ensuring that laser light reflected from any optical element further downstream is not returned to the laser head.

Laser light is then partially absorbed by a neutral-density filter. The utility of the neutral density filter is twofold, it decreases the laser light intensity, and thus power to 1) make the diagnostic safer, and 2) make the diagnostic less perturbative. The latter becomes important in low pressure/low plasma current experiments when absorption of laser light has a noticeable effect on discharge current.

Laser light is next reflected by two steering mirrors to aid in laser alignment (i.e. guiding the laser light through the small opening in the microwave cavity). The laser light then passes through the microwave cavity, is partially absorbed by the plasma, and is re-focused by a collecting lens. The light then passes through a 10nm band-pass filter (centered at 805nm) and is focused on the collecting element of a photodetector. The band-pass filter ensures that only laser light (and not room light or light from neighboring plasma emissions) is measured by the photodetector. The finite-width Gaussian nature of the bandpass filter allows the filter to be used when measuring absorbance of the 794nm and 811nm lines even though these wavelengths are out of the recommended range of the filter.

The double-pulse method

Enhanced adjustment over a wider range of plasma parameters is possible by applying a second voltage pulse to the system called the 'plasma-conditioning pulse'. The plasma-conditioning pulse can be applied at a specific time in the afterglow of the plasma-generating pulse, which allows for the flexible choice of initial electron density, n_e, and at a specific voltage, which allows for the flexible choice of reduced electric field strength E/N. Depending on the choice of time-delay between the pulses and on the choice of the voltage magnitude of the plasma-conditioning pulse, the system responds according to these two empirical rules: 1) if the plasma-conditioning pulse magnitude is greater than the plasma-generating pulse magnitude, then the residual electrons (electrons created during the plasma-generating pulse) will be accelerated to account for the increased E/N) or 2) if the plasma-conditioning pulse voltage magnitude is lower than the plasma-producing pulse voltage magnitude, then additional electrons will be created to account for the increased E/N.

The oscilloscope and determining reduced electric field (E/N)

Voltage signals generated from the Pearson coil and voltage divider are digitized by channels 1 and 2, respectively, of a 1GHz LeCroy WaveRunner (Model 6100A) Oscilloscope. These data are recorded redundantly using a LabView virtual instrument (vi) for both optical emission and microwave cavity data to ensure the repeatability of the datasets. Channel 3 of the oscilloscope is dedicated to the Photodetector used for TDLAS and channel 4 of the oscilloscope is used for MCRS data.

Experiments [*Pack et al.,* 1961; *Raju,* 2011] empirically correlate reduced electric field with electron drift velocity. This relation is exploited to get an experimentally determined value of reduced electric field. A Pearson current monitor is used to measure total current from the power supplies into the experimental apparatus; however, this signal is not the plasma current. Displacement currents from circuit elements other than the positive column must be considered. To determine plasma current, background current measurements are taken at the increased pressure of 10 Torr inside the chamber. This extinguishes the plasma (eliminating the plasma current) but keeps the circuit intact; thus, the background (displacement) current in the circuit can be isolated and measured. The difference between these two signals (Total current minus background current) is the plasma current.

The current waveform measured by the oscilloscope is translated into a current density, J, by assuming the electron current and electron density fills the discharge tube uniformly. The electron drift velocity is then calculated using the relation $J=e^{*}n_e^{*}v_D$. This drift velocity is then translated to reduced electric field using the results in [*Pack et al*., 1961].

Chapter V: Experimental Results, Interpretation

In this chapter, typical data from the experiment described in chapter IV are presented and anomalous behaviors are explained. A typical OES signal is shown, and the effect of contaminants on the spectra are discussed. A basic interpretation of the OES signal is offered. The method for obtaining electron density and collision frequency from MCRS is described, and a physical interpretation of a typical MRCS signal is offered. The method for obtaining excited state density from TDLAS is described, and a physical interpretation of typical TDLAS signal is offered. Anomalous behavior of excited state densities in the plasma are explained. Corrections to obtain the plasma-current waveform are discussed.

Optical emission spectra

Initial OES measurements made during the construction of the experimental apparatus showed unexpected N_2 band emission spectra in the 420nm and 427nm regions in addition to the expected argon spectral lines as shown in figure (5.1). While the presence of these nitrogen bands introduce uncertainty in determining the intensity of the argon spectral lines, the priority for correlating OES measurements to plasma parameters is quantifying the effect of trace N_2 on the shape of the electron energy distribution (EED) [*Lock et al.,* 2016]. This unwanted effect greatly affects the stepwise excitation of argon excited states and care must be taken to ensure that all trace molecular species (e.g. N_2, O_2) are expelled from the system before taking data. The N_2 bands at 427nm [*Pankhurst,* 1939; *Lofthus & Krupenie,* 1977] are helpful here - these bands are spectrally isolated from any other emissions and can be monitored to ensure that there are no leaks in the plasma chamber. Monitoring the (absence of) 427nm emission ensures the measured line intensities at 420.1nm and 419.8nm are only due to the argon emissions and devoid of any complicating N_2 signal or perturbations to the EED.

Trace spectral features in the 421-425nm range are also observed, occasionally, after a thin film was deposited on the cathode-side viewport, indicating that sputtering of the inside of the stainless steel discharge chamber occurred at some point during the course of experiments. The rarity of the signal, however, made the signal's exact origin inconclusive. A quick survey of NIST's database shows that wavelengths associated with Iron, Manganese, or Copper fall in the spectral range and would appear as spectral lines if those contaminants existed in the plasma. It is believed that trace metal impurities do not have a measureable effect on the EED.

Microwave cavity resonance spectroscopy (MCRS)

Electron density and electron collision frequency are measured using Microwave Cavity Resonance Spectroscopy (MCRS). Microwaves are transmitted into the cavity by biasing a copper antenna (length=12mm) located at r=40mm in the cavity body (the largest radius possible given cavity fabrication geometry). Careful choices of the cavity dimensions (outer radius 57mm, and length 32mm)

and applied microwave frequencies (2-3GHz) ensure that a pure TM_{010} mode is present in the cavity. The theoretical resonant frequency for a cylindrical microwave cavity is

$$f_{mnp} = \frac{c}{2\pi}\sqrt{\left(\frac{X_{mn}}{R_c}\right)^2 + \left(\frac{p\pi}{L}\right)^2}, \quad (5.1)$$

where m, n, and p are integers specifying the mode of the resonant frequency, c is the speed of light in a vacuum, X_{mn} are the first zeros of the Bessel function of the first kind of order zero, and R_c and L are the radius and length of the resonant cavity respectively. The resonant frequency for TM_{010} mode (m=0, n=1, and p=0; X_{01}=2.405) in a cavity of radius R_c = 5.7cm is f_o=2.02GHz. A null (no plasma) spectrum is obtained to quantify the cavity's response to the applied frequencies. From the null spectrum, the un-perturbed resonant frequency f_o=2.07Ghz and quality factor Q_o=520 are determined.

Inspection of the null spectrum, however, shows that background subtraction is necessary before reliable resonant frequency shift or quality factor degradation may be determined. A resonant-peak-free spectrum suitable for subtraction is obtained experimentally by deliberately shifting the resonance peak outside of the observed 2-3GHz window. Background spectra are obtained twice by 1) inserting a dielectric rod axially into the microwave cavity such that the resonance peak is shifted below the 2GHz lower limit of the scanned frequencies or 2) inserting conducting material axially into the microwave cavity such that the resonance peak is shifted above the 3GHz upper limit of the scanned frequencies. The background spectra obtained by these two methods are similar, indicating this method is valid, i.e., the introduction of the dielectric or conductor into the system has a negligible effect on the cavity response at the non-resonant frequencies.

Background-corrected spectra can now be analyzed to determine electron density and collision frequency. A shift in resonant-peak frequency and a decrease in resonant-peak amplitude between the observed plasma values and the null values indicate the presence of free electrons and electron collisions, respectively. These effects were first quantified in [*Biondi,* 1951] and later simplified by

[*Buchsbaum and Brown*, 1957]. The later relations are utilized in this work. The resonant frequency shift and quality factor degradation are characterized by

$$\frac{\Delta f}{f_o} = \frac{1}{2}\frac{\langle\eta\rangle}{1+\gamma^2}, \tag{5.2}$$

$$\frac{1}{Q} - \frac{1}{Q_o} = \frac{\gamma\langle\eta\rangle}{1+\gamma^2}, \tag{5.3}$$

where Δf, and f_o are the observed resonant-frequency shift and null resonant-frequency, and Q and Q_o are the observed and null quality factors of the cavity. $\gamma = {\nu_m}/{\omega}$ is a dimensionless quantity representing collision-induced damping in the plasma, where ν_m is the collision frequency, and ω is the angular frequency of applied microwaves $(2\pi f)$. Here, $\eta = {e^2 n_e}/{m_e \epsilon_o \omega^2}$, where e is the elementary charge, m_e is the mass of the electron, and ε_o is the permittivity of free space. The angle brackets <> in the above equations represent a volume integral over the electric field present in the cavity [*Slater,* 1946]. It is evident in these equations for frequency shift and quality factor (Q-factor) degradation that the presence of free electrons has a sensitive effect on the resonant-frequency shift and little effect on the degradation in observed cavity quality factor *Q*. Electron collision frequency, on the other hand, has a sensitive effect on the quality factor degradation while only providing a first-order correction to the resonant-frequency shift.

Buchsbaum and Brown's equations [*Buchsbaum and Brown*, 1957] for observed frequency shift and degradation of cavity quality factor are rearranged to obtain

$$\langle\eta\rangle = 2\left(\frac{\Delta f}{f_o}\right)(1+\gamma^2), \tag{5.4}$$

$$\gamma = \frac{1}{2}\left(\frac{f_o}{\Delta f}\right)\left(\frac{1}{Q} - \frac{1}{Q_o}\right). \tag{5.5}$$

Measured values of Δf and Q are coupled with physically reasonable values for f_0 and Q_0 to create an array of possible values of η and γ. The quantity η is then scaled by an 'overlap factor' (to account for the volume integrals implicit in

equations (5.2) and (5.3)) and matrices of possible values for electron density and collision frequency are created for all physically relevant quantities of observed frequency shift and observed Q-Shift. This procedure produces the 'look-up tables' shown in figure (5.2). Observed frequency shift and quality factor degradation are then used to accurately determine the unique electron density n_e and collision frequency ν_m.

The 'look up table' method is adopted here because accuracy lost in this method is negligible (smaller than the experimental error) and the analysis time is greatly decreased since once the tables are produced, the calculations do not need to be repeated. This removes the need for 2 calculations (electron density, and collision frequency) multiplied by 5000 time points equals 10,000 calculations per data set with negligible loss in accuracy.

A sinusoidal voltage waveform is applied to the antenna in the microwave-resonant cavity and the reflected power is recorded as a function of time on the oscilloscope. An example trace of reflected power vs. time at applied frequency 2.3Ghz is presented in figure (5.3). The microwave-reflected power is background corrected and then converted into a relative cavity-absorbed power, which is displayed on the color axis of figure (5.4). This process is repeated for a range of applied microwave frequencies (2-3.2 GHz) to populate the y-axis in figure (5.4). The location of the resonance (the position of the most-intense color on the y-axis) is a measure of frequency shift and, thus, the electron density. The width of the resonance (the gradient of the color axis near the resonance peak) is a relative measure of the cavity Q factor. The resonant-peak frequency and Q factor are then used in conjunction with the 'look-up tables' to determine the electron density and collision frequency at each time t. Typical electron density and collision frequency as a function of time is displayed as a function of time in figure (5.6).

Before the voltage pulse is applied (t<0μs), the resonance peak is very sharply peaked near the vacuum resonant frequency (f~2100 MHz). The presence of residual electrons from the previous voltage pulse is responsible for resonant frequency at this time being above the null case (f=2070MHz). The cavity Q factor is highest near the resonant frequency as evidenced by the steep gradient in the

color axis for a given time. When free-electrons are created in the Initiation and Transient phases of the pulse, the resonance peak will 1) shift to higher applied frequencies due to the increased conductivity of the plasma column, and 2) decrease in magnitude due to electron collisions in the plasma. In the Post-Transient stage and the afterglow, the resonant peak will re-sharpen as the electron collision frequency decreases. When the applied voltage pulse ends ($t=2*10^{-5}$sec), the resonance peak will begin to return to the vacuum resonant levels as electrons are lost due to recombination.

Excited species densities via TDLAS

The Beer-Lambert law is used to convert raw absorption waveforms into excited-state density waveforms. At any time t, the observed laser light intensity $I(t)$ is proportional to the initial intensity of the laser light I_o (i.e., the observed intensity when the metastable-atom density in the plasma is zero) according to the Beer-Lambert law

$$I(t) = I_o e^{-\Delta x / K(t)}, \tag{5.6}$$

where Δx is the line-integrated absorption path length of the laser in the plasma, and $K(t)$ is the mean-free path for laser photons. The mean-free path may be approximated by

$$K(t) = \lambda_{mfp} \cong (A_{21} \frac{\lambda^2}{8\pi} g(\nu) \frac{g_2}{g_1} n_1(t))^{-1}, \tag{5.7}$$

where A_{21} is the Einstein coefficient that characterizes the electron transition between the lower-state *1* and upper-state *2*, g_1 and g_2 are the statistical weights (2J+1) of excited atomic states *1* and *2* respectfully, $g(\nu)$ is the line-shape profile for photo-absorption from state *1* into state *2*, and n_1 is the density of the lower state *1* (absorbing species). Combining equations (5.6) and (5.7), the density of the absorbing species is

$$n_1(t) = \frac{g_1}{g_2} ln\left(\frac{I(t)}{I_o}\right) \frac{8\pi}{A_{21}\lambda^2 g(\nu)\Delta x}. \tag{5.8}$$

Figure (5.6) shows the typical $1s_5$ metastable-atom population density as a function of time throughout the discharge. The $1s_5$ metastable-atom state typically begins to populate ~5us after the initial voltage pulse is applied and reaches its

maximum value when the absorbed power into the plasma is at its peak, usually in the beginning of the Post-Transient stage of the discharge.

The peak in metastable-atom density indicates the loss mechanisms out of the metastable level dominate the creation mechanisms of the metastable level. Since relaxation of the metastable-atom levels via photon decay is forbidden, the most probable depopulation mechanism of the $1s_5$ metastable-atom is electron-collision-induced excitation of the metastable-atom. Electron collisions can excite the metastable atoms into higher, optically emitting states (e.g., stepwise excitation into the $3p_5$ state) or excite the metastable atoms into the more energetic levels in the $1s_x$ manifold. The selected cross sections for electron-impact excitation out of the $1s_5$ metastable level are shown in figure (5.7) to facilitate understanding of the observed de-population of the $1s_5$ metastable-atom state.

The only electron-collision excitation (depopulation) mechanism for low energy electrons (E<1.5eV) are excitations into the other three states of the $1s_x$ manifold; excitation into the $1s_2$ and $1s_4$ states are the dominant excitation mechanism for incident electron energy up to (E=3eV). Cross sections for dipole-allowed transitions into the resonant states ($1s_2$ and $1s_4$) are orders of magnitude greater than the cross section for the dipole-forbidden, spin-forbidden ($\Delta J = 2, \Delta m_s = 1$) transition into the $1s_3$ metastable state. Excitation into the dipole-allowed states of the $2p_x$ manifold are dominant for large energies (E>3eV), while cross-sections into dipole-allowed states of the $3p_x$ manifold (for example, the $3p_9$ state) are an order of magnitude smaller because of the larger energy gap between the states (change in principle quantum number, $\Delta n = 1$). The dipole allowed, spin allowed cross section into the $3p_9$ state, however, is still greater than the cross-section into the $1s_x$ states in this incident-electron energy region. Cross sections for dipole-forbidden transitions into the $3p_x$ manifold are orders of magnitude lower still for all energies. Experimental findings [*Jung et al.,* 2007] show that dipole-forbidden, spin-allowed transitions (i.e., $3p_5$ level) are orders of magnitude greater than similar dipole-forbidden, spin-forbidden transitions (e.g., $3p_1$ level).

While stepwise excitation into the optically emitting $3p_x$ states forms the crux of this dissertation, the cross-sections presented in figure (5.7) indicate the most-

probable excitation route out of the $1s_5$ metastable-atom level is excitation into the neighboring $1s_2$ and $1s_4$ resonant states. (Even though the $1s_2$ and $1s_4$ states can decay to the ground state by emitting 104.8nm and 106.7nm photons, these wavelengths are in the vacuum-ultraviolet (VUV) range, and are outside of the observable range of most optical spectroscopy systems, and not presented in this work.) Evidence of this stepwise population mechanism, however, can be inferred using TDLAS. Figure (5.8) shows the density of the $1s_5$, $1s_4$, and $1s_3$ states of argon as a function of time in a plasma-conditioned pulse. OES measurements imply the electron collisions throughout the voltage pulse have a net de-populating effect on the $1s_5$ state (stepwise excitation out of the $1s_5$ state decreases, while E/N and electron density are relatively constant). TDLAS measurements confirm that the density of the $1s_5$ metastable state decreases while the density of the $1s_4$ and $1s_3$ states increase, implying that the electron population in the plasma-conditioning pulse favors stepwise excitation into the energetically-nearby states (~0.1eV) of the $1s_x$ manifold over stepwise excitation into the optically emitting $2p_x$ and $3p_x$ manifolds (~2, 3eV). Electron collision-induced de-excitation from the $1s_3$ and $1s_4$ states into the $1s_5$ state is believed to be negligible.

Decreasing the applied voltage in the plasma-generating pulse decreases the initial electron density and initial metastable-atom density for the plasma-conditioning pulse. Decreasing initial electron density and decreasing initial metastable-atom density both decrease the observed excitation $(excitation \sim n_e n_m k_{ij}^l,)$ with excitation rate $k_{ij}^l = \int \sigma_{ij}^l \left(\frac{2\epsilon}{m_e}\right)^{1/2} f(\epsilon) d\epsilon$, thus, decreasing the observed metastable excitation routes $1s_5 \rightarrow 1s_4,\ 1s_5 \rightarrow 1s_3$. Decreasing the electron density increases the electron collision frequency in the pulse and gives rise to a transient phase, causing metastable-atom density to grow, and the conventional OES structure (Initiation, Transient, and Post-Transient stages) to return.

Similar excited species kinetics are observed while adjusting discharge pressure. Increasing discharge pressure decreases initial electron density and initial metastable-atom density, which, in turn, increases the electron collision frequency and the implied $1s_5 \rightarrow 1s_4,\ 1s_5 \rightarrow 1s_3$ excitation routes are no longer

noticeable. This behavior may be expected, considering that decreasing the applied voltage and increasing the discharge pressure have similar effects on the reduced electric field.

Section VI: Analysis/Conclusion

In this section, the relative intensity of argon emission lines is used to help understand the dynamic nature of atomic kinetics in an argon positive column. The 420.1-419.8nm emission-line ratio is used to empirically define three distinct stages of the discharge: the Initiation Stage, the Transient Stage, and the Post-Transient Stage. From this understanding, a qualitative understanding of dominant excitation and relaxation processes can be formulated. This prompts a quantitative study of the three stages individually. The role of electron collisions in the evolution of the discharge stages is discussed.

The relation between the 419.8nm and 425.9nm emission-lines is studied and a low-resolution alternative to the 420.1-419.8nm emission-line-ratio technique is proposed. Furthermore, the 425.9-419.8nm emission-line ratio is used to infer the overall shape and dynamics of the EED throughout the stages of the discharge. Two methods for implementing the 420.1-425.9nm emission-line-ratio technique are explored, and final conclusions are drawn.

The dynamic nature of atomic kinetics in the pulsed positive column

Initial, empirical inspection of the 420.1-419.8nm emission-line ratio suggests the pulse may be divided into three distinct line-ratio-characterized stages named the Initiation Stage, Transient Stage, and Post-Transient stage. The three stages of the pulse are shown in figure (6.1). Each stage is distinguished by a unique magnitude and slope of the observed emission ratio. Comparisons with analogous stages in the signals from other diagnostics suggest that the dynamic kinetics in the positive column may similarly correlate with these stages.

Experiments investigating the pulsed positive column are conducted over a range of pressures to show the three-stage structure is independent of pressure. The highly variable *temporal* dynamics resulting from the change in pressure are negated when the plasma properties are expressed as functions of reduced electric field instead of time. For example, the relationship between observed emission ratio and reduced electric field, as shown in figure (6.2), behaves similarly for the range of pressure explored here. While the temporal dynamics responsible for producing the optical emissions and reduced electric field in figure (6.2) vary significantly with changing pressure, the physics that produce these results are the same within analogous stages of the discharge and will be elucidated by considering the three stages of the discharge separately.

Initiation stage: The Initiation stage of the discharge is defined here as the time-window before the plasma electrons and metastable-atoms in the plasma affect the observed emission ratio. The applied voltage produces a high reduced-electric-field that in turn ionizes the gas and creates the metastable atoms. This stage is characterized by a static (i.e., zero slope) emission ratio that is often less that unity, which suggests a non-negligible population of supra-thermal electrons [*Boffard et al.,* 2015]; therefore, the resulting EEPF cannot be understood by the logic expressed in *Adams et al.,* [2012] and *Hagelaar & Pitchford,* [2005]. The disagreement between the observed emission ratio and the expected emission ratio in the Initiation stage shows the modeling of [*Adams et al.*, 2012] is not valid when considering a non-thermal (non-Druyvesteyn) distribution of electrons.

Transient stage: The Transient stage of the discharge is defined here as the

time-window during which the observed emission ratio increases, due to the presence of electrons and metastable-atoms. E/N decreases as the ionization fraction (i.e., conductivity) increases. While there is agreement between the model predictions and experimental results in the Post-Transient stage, figure (6.3) suggests that the model is not valid in the Transient stage of the discharge. One could, however, include electron heating from metastable-atoms to expand the validity of the model into the Transient stage, and consequentially, throughout the temporal extent of the pulsed discharge.

Post-Transient stage: The Post-Transient stage of the discharge is defined here as the time-window during which the observed line-emission ratio is static, after the plasma electrons and metastable-atoms in the plasma affect the observed emission ratio. Metastable-atom losses become significant; thus, the effect of metastable-atom density on the EED is negligible while electron density continues to increase causing E/N to further decrease. This combination of plasma parameters lead to the agreement between modeling and experiment shown in figure (6.3).

Electron collisions cause the three-stage structure.

The key to a holistic understanding of the atomic kinetics in the pulsed positive column is understanding the Transient stage of the discharge that is responsible for the three-stage evolution of the pulsed positive column. The Transient stage is empirically defined as the stage in the discharge where and electron-metastable collisions have a noticeable effect on the observed emission ratio (non-zero slope when plotted with respect to time). It is intuitive that the Transient stage should be accompanied by an increased collision frequency.

Figure (6.4) displays the time-rate-of-change in 420.1-419.8nm emission ratio as a function of collision frequency over a range of discharge current. The Initiation stage (green squares) is characterized by the highest collision frequency and is responsible for the production of free electrons and excited species (i.e., ionization and excitation). The applied electric field promotes the creation of free electrons via ionization of argon, promotes subsequent energization of free electrons, and promotes excitation of argon excited states through electron

collisions. The production of free-electrons and metastable-atoms in the Initiation stage has a profound effect on the shape of the EED, which plays a substantial role in the transition into the Transient stage.

The electron collisions in the Initiation stage may be understood by examining the momentum transfer cross section for argon in figure (6.5). Excitation and Ionization cross-sections (orange and grey traces, respectfully) are the major contribution to the effective cross section above 15eV. Considering that realistic EEDs have a sharp peak below 10eV, the majority of excitation and ionization collisions occur near the threshold values of 11.5eV and 15.75eV, at which energy the momentum transfer cross-section peaks near 10^{-19} m^2. Near-threshold collisions, such as these, deplete the EED above 11.5eV and convert those electrons to low-energy electrons ~1eV, where the effective cross-section for argon collisions are one to two orders of magnitude smaller. The ionization and excitation collisions that define the initiation stage produce a cooling effect in the plasma that essentially decreases the collision frequency as the discharge evolves, as evidenced in figure (6.4).

Examining the relative magnitudes of the emission-lines in the Initiation stage can offer insight to the EED as well. The Initiation stage is accompanied by a slightly increasing (but less than unity) 420.1-419.8nm emission-line ratio. While a sub-unity 420.1-419.8nm emission-line ratio has been attributed to high energy electrons (*Adams et al.,* 2012*; Boffard et al.,* 2015; *Franek et al.,* 2015; *Franek et al.,* 2016), this cannot be true in the present case of the Initiation Stage, as high-energy electrons would also favor the production of 425.9nm emission-line, which is contrary to observed emission data. In fact, the 425.9nm emission is the weakest of the three emission lines examined here. Instead, it is more likely that the low-energy bulk electron population favors direct excitation of 419.8nm emission the most, and favors 425.9nm emission the least.

In the absence of metastable-atoms (i.e., absence of stepwise excitation), the increasing 420.1-419.8nm emission ratio is attributable to changing direct excitation rates caused by an evolving EED profile. In the absence of stepwise excitation, the increasing 420.1-419.8nm emission-line ratio observed in the

initiation stage can only be caused by an increased moderate-energy (15eV-30eV) electron population that favors excitation of the $3p_9$ state over the $3p_5$ state (i.e., favors 420.1nm emission over 419.8nm emission). Therefore, when considering the dynamics of an EED in the present pulsed discharge, one should consider a low-energy bulk, which heats as the pulsed discharge matures due to increasing electron density or increased metastable-atom density.

Data taken from the Transient stage (blue circles in figure (6.4)) of the discharge are characterized by an increasing observed emission ratio (dR/dt>0). In the transient stage, the metastable-atom population is large enough that stepwise excitation of the $3p_9$ state is significant, which increases the observed emission ratio and adds another cooling mechanism for plasma electrons, further decreasing the collision frequency. The 425.9-419.8nm emission ratio increases in this stage as well, indicating that the intermediate-energy (15eV-30eV) electron population grows.

Data taken from the Post-Transient stage (red triangles) of the discharge are characterized by a static emission ratio (dR/dt~0). In the Post-Transient stage, the metastable-atom population begins to get smaller, however, the 420.1-419.8nm emission ratio remains relatively static because the direct excitation rates (namely, k^0_{419} in equation (3.6)) decrease as the EED continues to cool and the electron collision frequency continues to relax to a static value.

420.1-419.8nm emission-line ratio as a metastable-atom diagnostic

Figure (6.4) illustrates the dynamic kinetics of the pulsed positive column in the Initiation and Transient stages of the discharge, and helps explain how the assumptions implicit in the numerical model of the plasma are violated in these stages. The relatively static nature of the Post-Transient stage however, suggests that the numerical modeling, when coupled with the extended corona model, may be exploited for additional interpretation of the Post-Transient stage. In the Post-Transient stage of the discharge, metastable-atom density decreases and the effects of the metastable-atom population on the EED (and thus, the excitation rates in equation (3.6)) become negligible. Algebraic manipulation of the expression for observed emission-line ratio now yields an expression for

metastable-atom density as a function only of EED and reduced electric field. A numerical Boltzmann solver (Bolsig+) is used to predict the static EED resulting from specific electron densities, n_e, as functions of E/N. Metastable-atom density can consequently be expressed as a function of observed line-emission ratio, electron density, and reduced electric field

$$\frac{n_M}{N} = (R-1)\left(\frac{k_{419}{}^{o}(n_e, {}^{E}/_{N})}{k_{420}{}^{M}(n_e, {}^{E}/_{N})}\right). \quad (6.1)$$

Figure (6.3) compares the observed and model-predicted metastable-atom density for all three stages of the voltage pulse. Deviations between the model-predicted metastable-atom density and observed metastable-atom density are explained through proper analysis of the assumptions in the modeling. The predictions of metastable-atom density in figure (6.3) assume a Druyvesteyn EED with normalized electron density n_e/n_o = 5*10^{-6}. Effects of collisions between electrons and metastable-atoms are not included in determining this EED to best match the depleted metastable-atom conditions in the Post-Transient stage of the discharge. The model-predicted metastable-atom density agrees with the measured metastable-atom density within 20% in this stage of the discharge. The trendline for the red triangles shows the one-to-one relationship (slope = 1, R^2 = 0.9) between the predicted and observed quantities, demonstrating qualitative agreement. The y-intercept indicates that, on average, the model under-predicts the experimentally determined, normalized, metastable-atom density by ~10^{-7} in the Post-Transient stage.

As one should expect when the presence of metastable-atoms are present and their consequential effect on the EED [*Hagelaar & Pitchford,* 2005], the model grossly under-predicts the metastable-atom density in the earlier stages of the discharge. The abundance of metastable-atoms is expected to produce high-energy electrons (increase the effective electron temperature) [*Hagelaar & Pitchford,* 2005] which favor direct excitation, i.e., increasing the direct excitation rate $k^o{}_{419}$ leads to an increased metastable-atom density (assuming the observed emission ratio is constant) according to equation (6.1). A larger percentage of electrons with energies higher than those predicted by considering electron-

electron or electron-metastable collisions, i.e., supra-thermal electrons, in the earlier times of the pulse may lead to larger departures from the model in this stage.

420.1-425.9nm emission-line ratio for low-resolution spectroscopic measurements (in principle)

The utility of the 420.1-419.8nm emission-line ratio method may be restricted by spectral-resolution limitations in the instrumentation; the spectral lines in question are only 0.24nm apart and require a high-resolution system in order to be faithfully represented. Line broadening may make deconvolution of the lines difficult. Even yet, the utility of using neighboring emission lines is no longer a convenience, but more often a hindrance in expanding diagnostic capabilities to lower-budget laboratories. Specifically, with the advent of the affordable ICCD camera, multiple emission lines may be recorded synchronously (e.g., *Franek et al.,* 2015). Applying this technique to higher pressures may also be problematic as the $3p_5$ state (which leads to 419.8nm emission) has noteworthy pressure dependence [*Boffard et al.,* 2004]. The pressure dependence across three orders of magnitude are shown in figure (6.6). For comparison, the pressure dependence of the $3p_1$ state and the $3p_9$ state are shown in figures (6.7) and (6.8).

For lower-resolution spectroscopic systems, the 419.8nm emission line may be approximated by the 425.9nm emission-line to quantify direct electron-impact from the ground state. The 425.9nm emission-line is spectrally isolated from neighboring argon emission-lines and comes from the $3p_1$ upper state, which has been shown to exhibit less pressure dependence than the $3p_5$ state [*Boffard et al.,* 2004] that leads to 419.8nm emission. Earlier works using the 420.1nm-419.8nm emission-line ratio may be applied to lower-resolution systems once the relation between the 419.8nm and 425.9nm lines are quantified, i.e., the 425.9nm-419.8nm emission-line ratio is known. Equation (3.5) is used to show the 425.9-419.8nm emission-line ratio depends solely on the direct excitation rates, which are functions of electron density, metastable-atom density, and E/N.

$$Ratio = \frac{\phi_{425.9}}{\phi_{419.8}} = \left(\frac{{k_{426}}^{o}(f_e)}{{k_{419}}^{o}(f_e)}\right) = \left(\frac{{k_{426}}^{o}(n_e, n_m, {}^{E}/_{N})}{{k_{419}}^{o}(n_e, n_m, {}^{E}/_{N})}\right) \quad (6.2)$$

Producing EEDs using Bolsig+

To solve equation (6.2), plausible values for electron density, metastable-atom density, and E/N are used as inputs for a numerical Boltzmann solver (Bolsig+) as described by [*Hagelaar & Pitchford,* 2005]. The calculations in this dissertation consider ionization, excitation, and momentum transfer collisions between ground state argon atoms and electrons, as well as stepwise excitation and ionization from the four states of the $1s_x$ manifold. In this way, the heating effects of metastable atoms are incorporated into the prediction. The reverse reactions for ionization and excitation (recombination, and relaxation) are also included in the Boltzmann solver.

The calculated EED is used in equation (3.2) to calculate the direct excitation rates ${k_{426}}^{o},\ and\ {k_{419}}^{o}$ in equation (6.2). Typical behavior of the direct excitation ratio $\frac{k^o_{420.1}}{k^o_{420.1}}$ is presented in figure (6.9). Quick inspection of figure (6.9) suggests the observed emission-line intensity ratio may be used as a reduced electric field diagnostic in the limit of low E/N; however, this dependence changes drastically as a function of electron density (ionization fraction) and is unreliable. Figure (6.9) does imply, however, that the 425.9-419.8nm emission-line ratio approaches unity in the limit of large E/N for all electron densities. These trends may be understood after considering how the excitation rates and EEDs are calculated.

Increasing E/N shapes the EED. Specifically, lower-energy electrons are heated to populate the high-energy tail of the distribution and, consequentially, increase direct excitation as shown in figure (6.10). Particularly, the 15-30eV electron population, which favors 425.9nm emission increases; thus, the 425.9-419.8nm emission-line ratio increases with increasing E/N. This point is further illustrated in figure (6.11) where the percentage of electrons in the 15-30eV region is plotted as a function of E/N for a range of electron density. It is shown in figure (6.11) that the electron population responsible for an increasing 425.9-419.8nm emission-line ratio grows as a function of E/N for all electron densities. The 425.9-419.8nm emission-line ratio, however, does not increase for the entire range of E/N; Figure (6.9) shows that the modeled 425.9-419.8nm emission-line ratio

(considering to direct excitation only) increases to unity near 100Td and then levels off. This asymptotic behavior is due to a growing high-energy (>30eV) electron population, as shown in figure (6.12) for a range of electron density. The population of greater-than-30eV-electrons, which favors 419.8nm emission, has a significant and increasing population density above 100Td. Recalling figure (3.4) from chapter III, tells us that these high-energy electrons favor 419.8nm emission more strongly than intermediate-energy electrons favor 425.9nm emissions. Thus, the effect of the smaller, high-energy electron population may off-set the effect of the intermediate-energy electron population, and the 425.9-419.8nm emission ratio begins to level off near 100Td. Note that, for larger electron density, the density of the 15-30eV sub-population of electrons has a weaker E/N dependence and the 425.9-418.9nm emission-line ratio has a weaker E/N dependence as well, suggesting that highly-ionized plasmas are simpler to diagnose. Increasing electron density or increasing metastable-atom density have similar heating effects on the EED, which increases the 425.9-419.8nm emission-line ratio for smaller values of E/N. Overall, the 425.9-419.8nm emission-line ratio will approach unity for large E/N in any electron density or may approach unity for lower E/N values if the EED is sufficiently heated by electron-electron collisions (electron-density dependent) or electron-metastable collisions (metastable-atom-density dependent).

420.1-425.9nm emission-line ratio for low-resolution spectroscopic measurements (in practice)

The proximity of the 419.8nm, 420.1nm, and 425.9nm emission-lines allowed all three line profiles to be measured at once with high resolution. A typical spectrum showing fully-resolved emission-lines is given in Figure (5.1). In lower resolution systems, however, obtaining precise line intensities is not as straightforward because each emission line has a finite width. Thus, the observed peak intensity of an emission line may be affected by the wings of nearby emission-lines (e.g. the observed peak intensity of the 419.8nm emission line may be inflated by the 420.1nm emission-line wing). A more-typical spectrum, using a 1200groove/mm diffraction grating, is shown in figure (6.13), where the 420.1nm

and 419.8nm emission lines overlap. The recommended method to extract the peak intensities of these lines involves modeling the emission from the 425.9nm emission line in the following manner.

Assuming all of the states in the $3p_x$ manifold have the same temperature profile, the width of the emission lines from the manifold should be similar, and the 425.9nm profile may be used to determine scalable the emission-line profile for all emissions out of the manifold. A Matlab code was written to fit a pseudo-Voigt profile to the observed spectral data. The pseudo-Voigt profile is used to simultaneously account for various broadening mechanisms associated with Lorentzian or Gaussian line-shapes. The Lorentzian and Gaussian widths are calculated by a least-squares regression of the 425.9nm spectral line because, conveniently, the 425.9nm emission-line is spectrally isolated from other emissions. This fit (black trace) is superimposed on the observed data (blue circles) to produce figure (6.14). These widths are then used to determine the expected spectral signal created by the 420.1nm and 419.8nm emission-line profiles. This process creates the black trace in figure (6.15). If the calculated spectral profile at 418.9nm is significantly larger than the observed values, as is the case in figure (6.15), the observed peak receives a significant contribution to its intensity from the neighboring 420.1nm emission line, and the observed 420.1-419.8nm emission-line ratio is too small. The empirically-fit data from 425.9nm is then multiplied by an amplitude correction factor and subtracted from the peak at 419.8nm to produce the red trace in figure (6.15). If the peak intensity of the red peak at 420.1nm is equal to the calculated trace (black) and the observed data (blue circles) then there is not a significant contribution from the nearby 419.8nm emission line. Figure (6.15) shows that the 420.1nm emission line inflates the observed 419.8nm emission. Once the 419.8 contribution to the 420.1/419.8nm profile convolution is subtracted, the Gaussian 420.1nm emission-line profile is revealed as shown in the red trace in figure (6.15).

If the emission-line-profile modeling cannot be used to model the 425.9nm emission-line profile, it is still possible to use to raw data from the 425.9nm emission line to correct the 420.1nm-419.8nm emission-line convolution.

Multiplying the 425.9nm emission by an amplitude correction factor, the 425.9nm emission line can be used to remove the 419.8nm line profile from the profile convolution, and the remaining signal resembles a Gaussian distribution produced by the 420.1nm emission-line profile. The results of such a subtraction produce the cyan traces in figure (6.16). Figure (6.16) shows the raw data as well as both subtraction techniques described in this chapter for several spectra throughout a voltage pulse.

Conclusion

The dynamic behavior of the electron-atom collision-induced excitation rate $k^{o}_{419.8}(t)$ is inferred from temporal measurements of the electron density and reduced electric field in an argon pulsed positive column. The dynamic excitation rate, when coupled with the observed 420.1-419.8nm emission ratio, in the context of the extended coronal model, is shown to infer the dynamic metastable-atom density during the Post-Transient stage of the discharge within 20% of measured values. Thereby, the correlation between metastable-atom density, reduced electric field, electron energy distribution, and 420.1-419.8nm line ratio predicted in [*Adams et al.,* 2012] has been experimentally confirmed for the first time.

The observed emission-line ratio agrees quantitatively with the model-predicted line-emission ratio in the Transient and Post-Transient stages of the pulsed discharge and the two agree qualitatively in the Initiation stage of the pulsed discharge. Reasonable assumptions regarding the interpretation of the electron energy probability function, as it starts off being Druyvesteyn and later, as it becomes more Maxwellian with the increasing electron density, is key to interpreting and implementing the correlation for optimally explaining the temporal behavior of the emission-line ratio in all stages of the discharge.

The argon 425.9nm and 419.8nm emissions from the $3p_1$ and $3p_5$ upper states, respectively, are produced by electron-impact excitation of the ground state; the ratio of these emission-lines depends on the electron energy distribution. Low-energy electrons (E<15eV) and high-energy electrons (E>30eV) are more-likely to excite the neutral argon atom into the $3p_5$ state, producing 419.8nm emission, while intermediate-energy electrons (15eV<E<30eV) are more-likely to

excite neutral argon into the $3p_1$ state, producing 425.9nm emission. The 425.9-419.8nm emission-line ratio increases in the Transient stage of the discharge, which implies that the relative population of intermediate-energy electrons increases between the beginning and end of the Transient stage. The increase in intermediate-energy electrons is consistent with the ongoing 'maxwellianization' of the electron energy distribution throughout the pulsed discharge. Once the behavior of the 425.9-419.8nm emission-line ratio is understood, i.e., once the evolution of the electron energy distribution is understood, the 420.1-425.9nm emission-line-ratio technique may be used in lower-resolution spectroscopic systems in conjunction with the results of [*Adams et al*., 2012]. Otherwise, numerical calculation of the direct excitation rates that produce 425.9nm and 420.1nm emissions is necessary.

The observed range of values of electron density and reduced electric field are used to calculate equilibrium electron energy distribution functions from the Boltzmann equation using Bolsig+. These calculated EEDs are used to predict the value of the 425.9-419.8nm emission-line ratio and show that the value falls between 0.5 and 1 for the reported experiment, which is consistent with the observed emission-line ratio. In principle the 425.9-419.8nm emission-line ratio can be used to determine the EED. However, the energy threshold for electron-impact direct excitation for these emission-lines is ~13eV, and only a small percentage of plasma electrons contribute to the observed emission-line intensity. The electron energy distribution is expected to be sharply peaked; therefore, only a very small fraction of the plasma electron population near the 13eV threshold are expected to contribute to the observed emission lines. It is expected that a 425.9-419.8nm emission-line-ratio technique has an inherently large likelihood for error until the optical-emission cross-sections are carefully measured and modeled near this threshold energy. Without knowledge of these precise cross-sections, an emission-line technique, involving two emission-lines that are sensitive to stepwise excitation, would be more successful in determining electron density or reduced electric field. In contrast, the 420.1-419.8nm technique accurately predicts metastable-atom density because the threshold for stepwise excitation is near

3eV, and a majority of the total plasma electrons are expected to contribute to stepwise excitation.

The emission-line-ratio techniques presented in this dissertation may be applied to a range of pressures as long as appropriate corrections are made. For example, while the cross-sections for direct, coulomb-collision induced excitation is independent of pressure, the cascade contribution to an optical-emission cross-section has a drastic pressure dependence. Cross-sections are often measured in low-pressure conditions to minimize the cascade contribution; cascade contributions to the excitation rates can only be approximated as outlined in [*Boffard et al.,* 2007]. Therefore, at higher pressures (i.e., when the photon reabsorption length is comparable to the system size), re-adsorption effects need to be considered. For further information on pressure-dependent corrections to optical-emission cross-sections, see [*Boffard et al.,* 2010]. The work in this dissertation also assumes the plasma is in coronal equilibrium, thus, the rate of spontaneous decay out of an excited state (photon flux) is proportional to the parent-state's population rate, i.e. collisional de-excitation of an excited state is negligible. This is a safe assumption because the electron-metastable collision frequency is much smaller than the radiative relaxation rates for all monitored emission-lines ($\nu_{e^-,m} \ll A_{21}$). ICCD integration times (i.e., camera exposure times) are chosen to exceed the characteristic lifetimes of the excited states (around 100ns) to ensure the collected emissions are representative of existing plasma conditions. This must be considered when interrogation times approach the characteristic lifetimes.

While this dissertation focuses exclusively on argon, the results presented here may be generalized to any other monatomic element with a full valence shell (ns^2np^6). For example, the emission-line pairs for neon, krypton, and xenon that are presented in [*Adams et al.,* 2012] may be used to expand the emission-line-ratio technique to these noble gasses. Other monatomic elements with a full valence shell such as singly-ionized alkali metals and doubly-ionized alkaline earth metals also have two metastable energy levels that produce spectroscopic signatures. An analogous single-emission-line-ratio technique may be developed

for these metastable-ions.

While the emission-line-ratio technique is shown to predict relative metastable density and excitation rates using electron density and reduced electric field, in principle, the technique can also be used to imply an electron density, electron energy distribution, or even reduced electric field based on known relative metastable-atom density and excitation rates. While these milestones have not yet been reached, it is worth noting that this technique only implies *correlations* among plasma parameters, and is not capable of making direct measurements of one plasma parameter without the knowledge (or assumption) of other plasma parameters.

References

Adams S F, Bogdanov E A, V I Demidov, M E Koepke, and A A Kudryavtsev, 2012, Metastable atom and electron density diagnostic in the initial stage of a pulsed discharge in Ar and other rare gases by emission spectroscopy, *Phys. Plasmas.* **19,** 023510.

Adams S, Miles J, Laber A, Demidov V, Williamson J, and Tolson B, 2009, 19th International Symposium on Plasma Chemistry, Bochum (July 26–31, 2009).

Adomovich I V, Choi I, Jiang N, Kim J-H, Keshav S, Lempert W R, Mintusov E, Nishihara M, Samimy M, and Uddi M, 2009, Plasma assisted ignition and high-speed flow control: non-thermal and thermal effects, *Plasma Sources Sci. Technol.* **18,** 034018.

Babaeva N Y, and Kushner M J, 2014, Interaction of multiple atmospheric-pressure micro-plasma jets in small arrays: He/O_2 into humid air, *Plasma Sources Sci. Technol.* **23,** 015007.

Bates D R, and Damgaard A, 1949, The calculation of the absolute strengths of spectral lines, *Phil. Trans. Roy. Soc. London A,* **242,** 842.

Belostotskiy S G, Ouk T, Donnelly V M, Economou D J and Sadeghi N 2011 Time and space-resolved measurements of Ar(1s5) metastable density in a microplasma using diode laser absorption spectroscopy J. Phys. D: Appl. Phys. 44 145202

Biondi M A 1951 Measurement of the electron density in ionized gases by microwave techniques *Rev. Sci. Instrum.* **22,** 500.

Boffard J B, Lin C C, and DeJoseph C A, 2004, Application of excitation cross sections to optical plasma diagnostics, *J. Phys. D.* **37,** R143-R161.

Boffard J B, Chiaro B, Weber T, and Lin C C, 2007, Electron-impact excitation of argon: Optical emission cross sections in the range of 300-2500nm, Atomic Data and Nuclear Data Tables **93,** 831.

Boffard J B, Jung R O, Lin C C, and Wendt A E, 2009, Measurement of metastable and resonance level densities in rare-gas plasmas by optical emission spectroscopy, *Plasma Sources Sci. Technol.* **18,** 035017.

Boffard J B, Jung R O, Lin C C, and Wendt A E, 2010, Optical emission measurements of electron energy distributions in low-pressure argon inductively coupled plasmas, *Plasma Sources Sci. Technol.* **19,** 065001.

Boffard J B, Jung R O, Lin C C, Aneskavich L E, and Wendt A E, 2012, Argon 420.1-419.8nm emission line ratio for measuring plasma effective electron temperatures, *Plasma Sources Sci. Technol.* **45,** 045201.

Boffard J B, Wang S, Lin C C, and Wendt A E, 2015, Detection of fast electrons in pulsed argon inductively-coupled plasmas using the 420.1-419.8nm emission line pair Plasma Sources Sci. Technol. 24, 065005.

Boyd T J M and Sanderson J J, *The Physics of Plasmas*, Cambridge University Press, New York, 2003.

Buchsbaum S J and Brown S C 1957 Microwave measurements of high electron densities *Phys. Rev.* **106,** 196.

Chen F F, 1991, Plasma ionization by helicon waves, *Plasma Phys. Control. Fusion* **33,** 339-364.

Chilton J E, Boffard J B, Schappe R S, and Lin C C,1998, Measurement of electron-impact excitation into the $3p^5 4p$ levels of argon using Fourier-transform spectroscopy, *Phys. Rev. A* **57,** 267-277.

Cooper J, 1966, Plasma Spectroscopy, *Rep. Prog. Phys.* **29,** 35.

DeJoseph C A Jr, Demidov V I, and Kudryavtsev A A, 2005, Modification of a nonlocal electron energy distribution in a bounded plasma, *Phys. Rev. E : Atom. Molec. Phys.***72,** 036410.

Delamere P A, Otto A, Ma X, Bagenal F, and Wilson R J, 2015, Magnetic flux circulation in the rotationally driven giant magnetospheres, *J. Geophys. Res. Space Physics,* **120,** 4229-4245.

Demidov V I, DeJoseph C A Jr, and Kudryavtsev A A, 2006, Nonlocal effects in a bounded afterglow plasma with fast electrons, *IEEE Trans. Plasma. Sci.* **34,** 825-833.

Foster J, Sommers B, Weatherford B, Yee B, and Gupta M, 2011, Characterization of the evolution of underwater DBD plasma jet, *Plasma Sourc. Sci. Technolo.* **20,** 034018.

Fox-Lyon N, Knoll A J, Franek J B, Demidov V I, Godyak V, Koepke M E, and Oehrlein G S, 2013, Determination of Ar metastable atom densities in Ar and Ar/H_2 inductively coupled low-temperature plasmas, *J. Phys. D,* **46,** 485202.

Franek J B, Nogami S H, Demidov V I, Koepke M E, and Barnat E V, 2015, Correlating metastable-atom density, reduced electric field, and electron energy distribution in the post-transient stage of a 1-Torr argon discharge, *Plasma Sources Sci. Technol.* **24,** 034009.

Franek J B, Nogami S H, Demidov V I, Koepke M E, and Barnat E V, 2016, Dynamics of atomic kinetics in a pulsed positive-column discharge at 100Pa, *Plasma Phys. Control. Fusion.* ***59(1),*** 014005.

Gekelman W, Pfister H, Lucky Z, Bamber J, Leneman D, and Maggs J, 1991, Design, construction, and properties of the large plasma research device – The LAPD at UCLA, *Rev. Sci. Instrum.* **62,** 2875.

Graves D B, 2012, The emerging role of reactive oxygen and nitrogen species in redox biology and some implications for plasma applications to medicine and biology, *J. Phys. D* **45,** 263001.

Greenburg K E and Hebner G A 1993 Electron and metastable densities in parallel plate radiofrequency discharges J. Appl. Phys. 73 8126

Hagelaar G J M, and Pitchford L C, 2005, Solving the Boltzmann equation to obtain electron transport coefficients and rate coefficients for fluid models *Plasma Sources Sci. Technol.* **14,** 722-733.

Hanne G F and Kessler J, 1976, Study of exchange excitation in mercury by means of polarized electrons I. experiment, *J. Phys. B: Atom. Molec. Phys.* **9,** 791-804.

Hanne G F, 1976, Study of exchange excitation in mercury by means of polarized electrons II. theory, *J. Phys. B: Atom. Molec. Phys.* **9**, 805-815.

Inan, U and Gołkowski, M, *Principles of Plasma Physics for Engineers and Scientests,* Cambridge University Press, New York, 2011.

Jung R O, Boffard J B, Anderson L W, and Lin C C, 2007, Excitation into $3p^5 5p$ levels from the metastable levels of Ar, *Phys Rev. A* **75,** 052707.

Keidar M, Boyd I D, and Beilis I I, 2001, Plasma flow and plasma-wall transition in Hall thruster channel, *Phys. Plas.* **8,** 5315**-**5322.

Khakoo M A et al., 2002, Differential cross sections and cross section- ratios for the electron-impact excitation of the neon $2p^5 3s$ configuration, *Phys. Rev. A.* **65,** 062711.

Khakoo M A et al., 2004, Electron impact excitation of the argon $3p^5 4s$ configuration: differential cross-sections and cross-section ratios, *J. Phys. B:At. Mol. Opt. Phys.* **37,** 247-281.

Klose J Z, 1968, Experimental lifetimes of the 5p levels in Argon I, *J. Opt. Soc. Am.* **58,** 1509-1512.

Kugel H W et al, 2008, The effect of lithium surface coatings on plasma performance in the National Spherical Torus Experiment, *Phys. Plas*. **15**, 056118.

Liboff R L, *Introductory Quantum Mechanics*, Fourth Edition, Addison Wesley, New York, 2003.

Lieberman M A and Lichtenberg A J *Principles of plasma Discharges and Materials Processing*, John Wiley & Sons, Inc. New York, 1994.

Lock E H, Petrova Tz B, Petrov G M, Boris D R, and Walton S G, 2016, Electron beam-generated Ar/N2 plasmas: The effect of nitrogen addition of the brightest argon emission lines, *Phys. Plasmas* **23,** 043518.

Lofthus A, and Krupenie P H, 1977, The spectrum of molecular nitrogen, *J. Phys. Chem. Ref. Data.* **6,** 113.

Matzen M K “Pulsed-Power-Driven High Energy Density Physics and Inertial Confinement Fusion Research,” American Physical Society, Division of Plasma Physics Meeting Savannah, Georgia, Nov. 15, 2004. *Conference Presentation*

McMillin B K and Zachariah M R 1995 Two-dimensional argon metastable density measurements in a radio frequency plasma reactor by planar laser-induced fluorescence imaging J. Appl. Phys. 77 5538.

McQuarrie D A, and Simon J D, *Physical Chemistry: a molecular approach,* University Science Books, Sausalito, 1997.

Millard M W, Yaney P P, Ganguly B N and DeJoseph C A 1998 Diode laser absorption measurements of metastable helium glow discharges Plasma Sources Sci. Technol. 7 389–94.

Niermann B, Böke M, Sadeghi N and Winter J 2010 Space resolved density measurements of argon and helium metastable atoms in radio-frequency generated He-Ar micro-plasmas Eur. Phys. J. D 60 489–95.

National Research Council Plasma 2010 Committee, “Plasma Science: Advancing Knowledge in the National Interest,” The National Academies Press, Washington, D.C., 2010.

Pack J L, and Phelps A V 1961 Drift velocities of slow electrons in helium, neon, argon, hydrogen, and nitrogen *Phys. Rev.* **121,** 789.

Padial N T, Meneses G D, da Paixão F J, Csanak Gy., and Cartwright D C, 1981, Electron-impact excitation of the lowest four excited states of argon, *Phys. Rev. A* **23,** 2194.

Palmer C, *Diffraction Grating Handbook,* sixth edition, Newport Corporation 2005 http://optics.sgu.ru/~ulianov/Students/Books/Applied_Optics/E.%20Loewen%20Diffraction%20Grating%20Handbook%20(2005).pdf

Pankhurst R C, 1939, Note on the second positive band-system of nitrogen, *Proc. Phys. Soc.* **52,** 388.

Pieper J B, Goree J, and Quinn R A, 1996, Three-dimensional structure in a crystallized dusty plasma, *Phys. Rev. E,* **54,** 5636-5640.

Racah G, 1942, On a new type of vector coupling in complex spectra, *Phys. Rev.* **61,** 537.

Raju G G, *Gaseous Electronics: Tables, Atoms, and Molecules,* CRC Press, Boca Raton, 2011.

Sharpton F A, St. John R M, Lin C C, Fajen F E, 1970, Experimental and theoretical studies of electron-impact excitation of neon, *Phys. Rev. A* **2,** 1305.

Sheehan J P, Kaganovich I D, Wang H, Sydorenko D, Raitses Y, and Hershkowitz N, 2014, Effects of emitted electron temperature on the plasma sheath, *Phys. Plasmas,* **21,** 063502.

Slater J C 1946 Microwave electronics *Rev. Mod. Phys.* **18,** 441.

Stewart R S and Smith D J, 2002, Complementary optical diagnostic modeling of the argon positive column, *J. Phys. D: Appl. Phys.* **35,** 1777-1787.

Vitelaru C, Lundin D, Stancu G D, Brenning N, Bretagne J and Minea T 2012 Argon metastables in HiPIMS: time resolved tunable diode-laser diagnostics Plasma Sources Sci. Technol. 21, 025010

Wallace E, Thomas E, Eadon A, and Jackson J D, 2004, Design and initial operation of the Auburn Linear Experiment for Instability Studies: A new plasma experiment for studying shear driven flows, *Rev. Sci. Instrum.* **75,** 5160.

Weitzner H, 2014 Ideal magnetohydrodynamic equilibrium in a non-symmetric topological torus, *Phys. Plasmas,* **21,** 022515.

Wang S-B, and Wendt A E, 2000, Control of ion energy distribution at substrates during plasma processing, *J Appl. Phys,* **88,** 643.

Weber T, Boffard J B, and Lin C C, 2003, Electron-impact excitation cross sections of the higher argon $3p^5\,np$ (n=5,6,7) levels, *Phys. Rev. A* **68,** 032719.

Yun S, Taylor K, and Tynan G R, 2000, Measurement of radial neutral pressure and plasma density profiles in various plasma conditions in large-area high-density plasma sources, *Phys. Plasmas,* **7,** 3448.

Zhang S, Sobota A, van Veldhuizen E M, and Bruggeman P J, 2015, Gas flow characteristics of a time modulated APPJ: the effect of gas heating on flow dynamics, *J. Phys. D* **48,** 015203.

Zhu X-M and Pu Y-K 2010 A simple collisional-radiative model for low-temperature argon discharges with pressure ranging from 1Pa to

atmospheric pressure: kinetics of Paschen 1s and 2p levels, *J. Phys. D: Appl. Phys.* **43,** 015204.

Zhu W, Sridhar S, Liu L, Hernandez E, Donnelly V M, and Economou D J, 2014, Photo-assisted etching of silicon in chlorine- and bromine-containing plasmas, *J Appl. Phys.* **115,** 203303

Appendix A: Angular momenta considerations in excited states of the noble gasses

Applying the Russel-Saunders methodology for adding angular momenta (the perfidiously named LS coupling), the total orbital angular momentum of the excited atom will be expressed $L = l_{hole} \otimes l_{electron} = 1$ and the total spin angular momentum of the excited atom may take on the values $S = s_{hole} \otimes s_{electron} = \binom{1}{0}$. The total angular momentum of the atom can then manifest as one of four allowed states $J = L \otimes S = 1 \otimes \binom{1}{0} = \binom{2,1,0}{1}$. The S=1 total spin couples with the orbital angular momentum L=1 to allow the triplet states, $^3P_{0,1,2}$. The S=0 total spin couples with the L=1 orbital angular momentum to allow only the singlet state $^1P_1$. Hund's first rule (of maximum multiplicity) dictates that the triplet states have the lowest energy (the triplet wavefunctions are spatially antisymmetric) and the singlet state has a notably higher energy (the singlet wavefunction is spatially symmetric) [*Liboff,* 2003]. According to Hund's third rule (Hund's second rule is not needed because there is only one value of total orbital angular momentum), the spin-orbit effect will energetically distinguish the triplet states by virtue of having different total angular momentum J. This triplet structure can be seen in the first four energy levels of neon in figure (A.1), but is replaced by a doublet structure in heavier noble gasses such as argon (figure (A.2)) and krypton (figure(A.3)). It should be noted that Hund's rules need not apply to the argon system explored in this dissertation because 1) argon is not strictly a Russel-Saunders coupled atom, and 2) Hund's rules are designed to determine an atom's ground state, not the sequence of excited states.

In the Russel-Saunders angular momentum addition scheme, the individual orbital angular momenta of the electron-hole and the promoted electron are added to obtain a discrete state of total orbital angular momentum. Likewise, the spin angular momenta of the electron-hole and the promoted electron are added to obtain discrete values of the total spin angular momentum of the system. These total angular momenta are then combined to obtain four possible values for total angular momenta J. The eigenstates produced by Russel-Saunders coupling (the term symbols) are eigenstates of L^2, S^2, J^2 and J_z [*Liboff,* 2003; *McQuarrie,* 1997] because L, S, and J are defined quantities in the Russel-Saunders convention. The eigenstates of identical J (J=1) must be represented as a superposition of states such that

$$|^3P_2\rangle = |L^2 = 1, S^2 = 1, J^2 = 2, J_z = 2\rangle\,, \tag{A.1.a}$$

$$|^3P_1\rangle = \alpha|L^2 = 1, S^2 = 1, J^2 = 1, J_z = 0\rangle + \beta|L^2 = 1, S^2 = 1, J^2 = 1, J_z = 1\rangle\,, \tag{A.1.b}$$

$$|^3P_0\rangle = |L^2 = 1, S^2 = 1, J^2 = 0, J_z = 0\rangle\,, \tag{A.1.c}$$

$$|^1P_1\rangle = \beta|L^2 = 1, S^2 = 1, J^2 = 1, J_z = 0\rangle - \alpha|L^2 = 1, S^2 = 1, J^2 = 1, J_z = 1\rangle, \tag{A.1.d}$$

where L^2, S^2, J^2 are the combined orbital, spin, and total angular momentum eigenstates for the argon atom, J_z. While this is exact in the absence of spin-orbit coupling (the coupling of orbital angular momentum l_c and spin angular momentum s_c of the ion core), and direction of the total angular momentum is inconsequential, the superposition in equations (A.1.b) and (A.1.d) become evident in higher-mass atoms.

While the energy-level structure predicted by the Russel-Saunders addition scheme can nevertheless reasonably describe the low-energy energy level configurations for neon (z=10), extrapolating this pattern to atoms of greater atomic

mass, where other energy-modifying effects become dominant (e.g. spin-orbit coupling), is of limited accuracy. The four predicted states J=1, 0, 1, 2 are empirically labeled $1s_2$, $1s_3$, $1s_4$, and $1s_5$, respectively, in Paschen's notation where $1s_2$ is the most-energetic of the four states, $1s_3$ is the second-most energetic and so forth. These first four excited states in the $(np)^5(n+1)s$ electron configuration for the noble gasses Ne, Ar, Kr, and Xe (n=2, 3, 4, 5) are collectively referred to as the 1s or $1s_x$ manifold. Paschen notation is used to emphasize the hierarchy of energy states without imposing implications on the energy-level spacing of the states. Paschen's notation is frequently used among spectroscopists (and in much of this dissertation) due to its convenience, while the lack of specific scientific detail allows the notation to remain applicable for any coupling scheme.

It is worth noting that applying Hund's rules to the Russel-Saunders energy levels *quantitatively* predicts the lowest energy level of the $1s_x$ manifold in this specific case – the simplest case - but does not dictate the *qualitative* structure. Argon does not exhibit the triplet-like energy level structure predicted in Russel-Saunders coupling – as exemplified in neon, figure (A.1). Instead, energy-level corrections from the spin-orbit interaction of the ion core become discernable, and the apparent triplet-like structure of the $1s_x$ manifold disappears for the higher-mass noble gasses, as shown in figures (A.2), argon, and (A.3) krypton. In the extreme case of xenon (z=54), the four states of the $1s_x$ manifold have a doublet structure because the spin-orbit energy correction, which is indicative of *j-j* coupling, is larger than the electrostatic repulsion energy correction that is responsible for the singlet-triplet energy level structure.

Cases between these two extremes, such as medium-mass atoms, and highly-excited levels of light atoms, require an intermediate coupling procedure to accurately predict the energy level structure. For the intermediate coupling cases such as those exhibited in the higher-lying states of argon, the *j-K* coupling scheme is most correct, and information regarding angular momenta, concealed by the empirical Paschen notation, may be elucidated by expressing the energy-states using Racah's notation [*Racah,* 1942]. Racah notation explicitly states the term-symbol of the ion core, the orbital of the promoted electron, the intermediate-coupling vector $K = j_h + l_o$, and the total spin of the final state $J = K + s_o$. Accordingly, the $1s_2$ energy-state of argon is denoted $(^2P_{1/2})4s'[1/2]_1$, where the ' signifies that the spin angular momentum of the electron-hole is anti-aligned with the orbital angular momentum of the electron-hole ($j_h = 1/2$). The *j-K* coupling scheme correctly predicts the hierarchy of the four states of the $1s_x$ manifold and nine of the ten states of the $3p_x$ manifold.

While the presence of the aforementioned coupling schemes is ubiquitous throughout the literature, the seamless transition between the various coupling schemes and notations makes the schemes hard to differentiate. It is regrettable that all three coupling schemes and their respective notations will appear sporadically throughout this dissertation in different sections as the utility of each notation has its pros and cons. The empirical Paschen notation, for example, describes the energy levels of the observed states but buries any acknowledgement of the vector-addition of the angular momenta. The well-known term-symbol notation (describing L-S coupling) allows the vector-addition of the

momenta to be understood; however, Hund's rules fail to predict the energy level structure. *j-k* coupling provides the most-clear picture of the addition of angular momenta and accurately predicts the energy-level hierarchy of the excited states. Racha's notation describing *j-k* coupling, on the other hand, is cumbersome, is not well-suited for conveying information, and should be avoided [*Boffard et al.*, 2004] unless the underlying vector-addition picture of Racah's notation is vital to the discussion.

Applying the *j-k* methodology for adding angular momenta (*j-k* coupling), the angular momentum of the ion core can take on two values $j_c = l_{hole} \otimes s_{hole} = \binom{3/2}{1/2}$. The intermediate-coupling vector is then $K = j_c \otimes l_{electron} = \binom{3/2}{1/2}$ because $l_{electron} = 0$. The total angular momentum of the atom can then manifest as one of four allowed states $J = K \otimes S_{electron} = \binom{2,1}{1,0}$. Generalizing Hund's rules to the *j-k* coupling scheme, one may postulate that the state of largest core angular momentum j_c will be the lowest energy state; of these states, the state of largest *K* will have the least energy. (This is empirically true for $K > j_h$, otherwise the state of largest K will have the greatest energy.) Note that the states of larger K are also states of larger L (for $K > j_h$) and have aligned (spatially symmetric) orbital wavefunctions. Thus, states of larger K should have lower energy. This doublet structure predicted by *j-k* coupling can be seen in the 2s and 3p manifolds of argon in figure (A.2) and in the 1s manifold of krypton (figure (A.3)).

To gain a holistic understanding of the relation between the argon excited states, the relations between the above-mentioned coupling mechanisms and their respective notations must be discussed in more detail. The observed $1s_2$ and $1s_4$

states, for example, are considered mixed states because they contain contributions from both the triplet ($^3P_1$) and the singlet ($^1P_1$) wavefunctions predicted by Russel-Saunders coupling. These states can therefore be understood as linear combinations [*Sharpton et al.,* 1970; *Boffard et al.,* 2004; *Pedial et al.,* 1981] of the term symbols as expressed by

$$|1s_2\rangle = \alpha|^1P_1\rangle + \beta|^3P_1\rangle, \tag{2.2}$$

$$|1s_4\rangle = -\beta|^1P_1\rangle + \alpha|^3P_1\rangle, \tag{2.3}$$

where the (empirical) Paschen wavefunctions $|1s_2\rangle$ and $|1s_4\rangle$ are used to denote that the observed energy levels and the Russel-Saunders state wavefunctions are eigenstates of combined angular momenta as evidenced in equation (A.1). α and β are mixing coefficients [*Kahkoo et al.,* 2002], normalized such that $\alpha^2 + \beta^2 = 1$, and describe the degree to which the states mix. In the case of the hydrogen atom (where there is no spin-orbit coupling of an ion core) the states do not mix, and the pair (α, β) would simply be (1, 0). In neon, calculations [Kahkoo et al., 2002] estimate the mixing coefficients as (0.94, 0.34) and (0.985, 0.175) from a unitarized first-order many-body theory calculation and an R-Matrix calculation, respectively. Similar calculations for argon [Kahkoo et al., 2004] estimate the mixing coefficients as (0.893, 0.450) and (0.95, 0.31).

The Paschen states represent the observed energy levels and are written as linear-combinations of Russel-Saunders states because the L^2, S^2, J^2 J_z basis is not sufficient to describe the spin-orbit coupling of the ion core [*Liboff,* 2003] The orbital angular momentum projection and spin angular momentum projection for the ion core (electron-hole) must be known for the spin-orbit energy correction

[*Liboff,* 2003] because the spin-orbit interaction for the promoted electron (L_e=0) is zero. The excited state mixing in equations (A.2) and (A.3) may be understood by considering the following: The electron-repulsion correction (which leads to Hund's first rule) depends on the total spin angular momentum $S=s_1+s_2$ of the atom which is an eigenvalue of the Russel-Saunders eigenstates. The spin-orbit interaction of the ion core, however, depends on the angular momentum of individual electron (or electron-hole), which requires a change of basis states from the Russel-Saunders states into states that define the angular momenta of the ion core,

$$|L^2S^2J^2J_z\rangle, \rightarrow |L^2L_ZS^2S_Z\rangle_{hole} \oplus |L^2L_ZS^2S_Z\rangle_{electron}, \qquad \text{(A.4)}$$

where the new wavefunctions of the right hand side are eigenstates of the orbital and spin angular momenta of the electron-hole (first term) and the promoted electron (second term). In this new basis, the total angular momentum J of the atom is no longer a defined quantity and, thus, the observed (Paschen) state must be a mixed state of these two eigenstates as shown in equations (A.2) and (A.3).

The $^3P_{0,}$ and $^3P_2$ term symbols are referred to as "pure" triplet states in this context because they have unique and well-defined values of total angular momentum. These terms are pure triplet states with definite total spin angular momentum $\langle S\rangle = \langle s_1 + s_2\rangle = 1$ and, thus, the spin-orbit correction to the energy levels do not mix the states. These states correspond to the observed $1s_3$ and $1s_5$ Paschen levels exactly.

Aside from the qualitative structure of excited energy levels, an effect of increasing atomic mass is also seen in the profile of the energy dependence of

excitation cross sections into the excited states of the $1s_x$ manifold. For example, triplet excitation, i.e. excitation from the $^1S_0$ (singlet) ground state into a ^3P (triplet) state by electron collision, typically peaks near the ionization energy of the atom and quickly falls off for larger energies, while singlet excitation, i.e. excitation from the $^1S_0$ (singlet) ground state into a $^1P_1$ (singlet) state by electron collision, is characterized by a broadly peaked cross-section profile. The $1s_3$ and $1s_5$ states (J=0 and J=2) corresponding to the $^3P_0$ and $^3P_2$ states are pure triplet states that display the expected triplet behavior for all of the noble gasses and will not be examined further. In contrast, the $1s_2$ and $1s_4$ states (J=1 and J=1) are linear superpositions of J=1 Russel-Saunders states ($^3P_1$ and $^1P_1$) and exhibit a "mixed" excitation profile. For light atoms such as neon, the Russel-Saunders behavior is dominant – the $1s_4$ state is dominated by the triplet component while the $1s_2$ state is dominated by the singlet component – and the cross-section profiles for the states are visibly different. For heavier atoms, such as argon and krypton, the Russel-Saunders mixing becomes prevalent and the Paschen states have equal triplet and singlet components as shown in figure (A.5).

Figure (A.5) shows excitation cross-sections into the $1s_2$ and $1s_4$ states for several noble gasses. The $1s_2$ state is predominantly a singlet state and shows a singlet-like excitation profile predicted by Russel-Saunders coupling, whereas the $1s_4$ state is predominantly a triplet state when considering low atomic masses such as neon. The cross-section for the $1s_4$ state exhibits a triplet-like (sharply-peaked) profile for small atomic mass whereas the cross section for the $1s_2$ state exhibits a singlet-like (broadly-peaked) profile. For increasing atomic mass, the Paschen

states become increasingly mixed. In the extreme case of krypton, the mixing is complete and the cross-section profiles for excitation into the $1s_2$ and $1s_4$ states are nearly identical.

Appendix B

IOP Publishing Plasma Sources Science and Technology

Plasma Sources Sci. Technol. **24** (2015) 034009 (8pp) doi:10.1088/0963-0252/24/3/034009

Correlating metastable-atom density, reduced electric field, and electron energy distribution in the post-transient stage of a 1-Torr argon discharge

J B Franek[1], S H Nogami[1], V I Demidov[1,2], M E Koepke[1] and E V Barnat[3]

[1] West Virginia University, Morgantown, WV 26505-6315, USA
[2] ITMO University, St Petersburg 197101, Russia
[3] Sandia National Labs, Albuquerque, NM 87123, USA

E-mail: jfranek@mix.wvu.edu

Received 31 January 2015, revised 26 April 2015
Accepted for publication 6 May 2015
Published 5 June 2015

Abstract

Temporal measurement of electron density, metastable-atom density, and reduced electric field are used to infer the dynamic behavior of the excitation rates describing electron-atom collision-induced excitation in the positive column of a 1 Torr argon plasma by invoking plausible assumptions regarding the shape of the electron energy distribution function performed in Adams *et al* (2012 *Phys. Plasmas* **19** 023510). These inferred rates are used to predict the 420.1 nm to 419.8 nm argon emission ratio, which agree with experimental results when the assumptions are applicable. Thus the observed emission ratio is demonstrated to be dependent on the metastable-atom density, electron density, and reduced electric field. The established confidence in the validity of this emission-line-ratio model allows us to predict metastable argon-atom density during the post-transient phase of the pulse as suggested by De Joseph *et al* (2005 *Phys. Rev.* E **72** 036410). Similar inferences of electron density and reduced electric field based on readily available diagnostic signatures may also be afforded by this model.

Keywords: optical emission spectroscopy (OES), 420.1–419.8 nm emission-line ratio, $1s_5$ metastable argon atom, reduced electric field (E/N), electron energy distribution, time-resolved, extended corona model

(Some figures may appear in colour only in the online journal)

1. Introduction

As the practice of plasma processing has grown in the past few decades, so has the desire to elucidate the influential plasma parameters and reactive species in the plasma; especially those at the sheath of the plasma-surface interface. Methods have been developed to monitor reactive plasma species, however, the use of the associated diagnostics may be limited by system geometry and cost. Metastable-atom densities for example have been spatially and temporally resolved in many works [1–6] via backlight spectroscopy, laser induced fluorescence (LIF), or laser absorption spectroscopy (LAS). These diagnostics are minimally invasive in the sense that they are optical techniques, however, these techniques usually require two optical ports on a device—one for light injection, another for radiation collection—while the LIF and LAS require a laser capable of probing the metastable level in question, which is not always readily available. Finding correlations between plasma parameters and alternate means to measure these plasma parameters may therefore be of great utility to the plasma scientist who is without these capabilities. Emission spectrum diagnostics are non-invasive and do

not require a secondary light source. The primary drawback to emission techniques is the difficulty associated with understanding the atomic processes that lead to these emissions.

Impressively accurate collisional-radiative models have been used to model plasmas and have been tested by experimental observations in various discharges and pressures (see [7], and [4–20] therein). Efforts have been made [7–17] to simplify these complex collisional radiative models for extracting diagnostic signatures without sacrificing accuracy, however, these simplifications still require algebraic overhead. While the radiation-trapping effects of the often-utilized $2p_x \rightarrow 1s_y$ transitions (in Paschen's notation) [18] are taken into account, or even exploited [9], eliminating the need to account for these effects by directly observing the $3p_x \rightarrow 1s_y$ transitions [19] would be preferable in most cases as this simplifies the analysis. DeJoseph *et al* [20] first suggested that the argon 420.1–419.8 nm ratio may be useful in detecting metastable argon atoms because of the proximity of the lines. These emission lines have proven to be useful in determining time-averaged electron temperature [19] by assuming a Maxwellian-like EEDF, and in determining metastable-atom density [21] by incorporating a measured EEDF.

In section 2 of this work we briefly discuss the extended corona model put forth by Boffard *et al* [8, 9, 19], the analytic form of the excitation rates k_{ij}^l, and how plasma parameters are used to predict the observed emission-line ratio. In section 3 we discuss the experimental configuration including the apparatus used to produce the positive column and the diagnostics. In section 4 we demonstrate the validity of the analysis outlined in section 2 in two equivalent ways: (1) we use the calculated excitation rates from Adams *et al* [22] in conjunction with measured metastable-atom density and electron density to predict the 420.1–419.8 nm emission-line ratio and compare the predictions to observed data; and (2) we use measured emission-line ratio, metastable-atom density, and electron density to experimentally determine the excitation rates in [22]. Both of these ways are used to validate the model and bear their own utility. We also show how this model can be properly exploited to predict the metastable-atom density directly from the model within experimental error. Conclusions are drawn in section 5.

2. The corona model and the inclusion of metastable-atoms

In corona equilibrium [23], the only source for a given excited-state population is electron-impact excitation from the ground state and the only sink (relaxation or decay process) is electron transition via photon emission. Whereas using the corona-equilibrium model is convenient for low-pressure plasma, describing argon at higher pressure requires an extended corona-equilibrium model [8] to account for the presence of metastable-atoms. The photon flux ϕ_{ij} (number of photons per second) is proportional to observed intensity I_{ij}, (watts per unit area) given by Adams *et al* [22] as

$$I_{ij} = Kn_e\mathcal{R}_{ij}[n_o k_{ij}^o + n_M k_{ij}^M + ...], \quad (1)$$

where K is a constant that includes geometric and conversion factors associated with the collection of the emitted light, n_e is the electron number density, $\mathcal{R}_{ij}$ is the correction factor for line-specific effects that depend on plasma optical thickness, n_o represents the number density of atoms in the ground state, and n_M represents the number density of atoms in the $1s_5$ metastable-atom state. The excitation rates k_{ij}^l describe the rate at which atoms in the state $l = o, M$ become excited to the emitting state of interest i and relax to the state of interest j, thus emitting a photon having the observed wavelength λ_{ij}.

The excitation rates k_{ij}^l from the numerical model [22] are given by Adams *et al* [24]

$$k_{ij}^l = \int_0^\infty \sigma_{ij}^l(\epsilon)\left(\frac{2\epsilon}{m_e}\right)^{1/2} f(\epsilon)\mathrm{d}\epsilon, \quad (2)$$

where σ_{ij}^l is the optical emission cross section for the state l, ϵ is the electron energy, m_e is the mass of the electron, and $f(\epsilon)$ is the assumed EEDF. The optical emission cross-section of Jung *et al* [18] is used to describe excitation into the emitting level i, and subsequent emission into lower state j, thus accounting for cascade effects and branching ratios for a given choice of cross-section. Interested readers are referred to [19, 23] for an extensive discussion on the use of optical emission cross sections in the extended corona model.

The EEDF in equation (2) can be taken from experimental data [21] or estimated. The analysis in Boffard *et al* [8, 19] uses a 'two-parameter' EEDF based on electron temperature and a variable fitting parameter to estimate the excitation rate of equation (2). Whereas the electron temperature has an unambiguous physical meaning, the fitting parameter describes only the shape of the EEDF. The numerical analysis [22] of the plasma, considered here, incorporates the effects of three important plasma parameters (electron density, metastable-atom density and reduced electric field) to determine the EEDF. Briefly, the effect of electron heating is included in the Boltzmann equation by the operators associated with the electric field, and electron collisions [22]. The use of these operators in the Boltzmann equation thereby produces EEDFs consistent with the plasma electron density, metastable-atom density, and reduced electric field [25]. These EEDFs are then used in equation (2) to produce the excitation rates published in Adams *et al* [22] and employed here. The selected excitation rates are reproduced in figure 1. Here, for brevity, the states i, j are replaced by the wavelength of their transition in nanometers. Specifically, the $3p_5 \rightarrow 1s_4$ transition is denoted by 419.8 nm and the $3p_9 \rightarrow 1s_5$ transition is denoted by 420.1 nm.

It is worth noting that predicting a simple change of the observed emission-line ratio as the metastable-atom density and electron density are increased or decreased is not straightforward. An increased metastable-atom density may increase the amount of inelastic metastable-electron collisions that, in turn, will cool the EEDF. On the other hand, an increased electron density n_e will affect the EEDF differently depending on how the electrons are added into the system [22].

Equation (1) suggests that any excited state may serve as the source for electron-collision-induced excitation of a

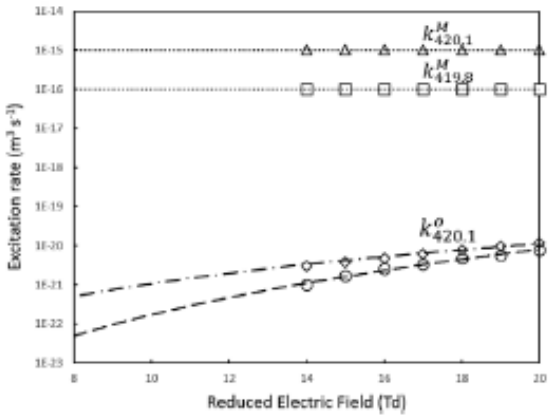

Figure 1. Stepwise, $k^M_{420.1}$ (triangle), and direct, $k^o_{420.1}$ (square), excitation rates leading to 420.1 nm emission. The bounds of the direct excitation rate are shown for the range of normalized electron density explored here ($n_e/n_o = 10^{-5}$ cm^{-3} diamond, and $n_e/n_o = 10^{-6}$ cm^{-3} circle). Note that $k^o_{419.8} \approx k^o_{420.1}$ in the range presented here [22]. Data points are taken from [22].

more-energetic state. Specifically, the analysis in [22] shows the rate at which a population of argon atoms in the $1s_5$ metastable-atom state is excited into various states of the $3p_x$ manifold (called stepwise excitation). These rates are several orders of magnitude greater than the rate of excitation out of the ground state of argon into the various states of the $3p_x$ manifold (called direct excitation) and depend on plasma conditions. If the stepwise excitation from a sparsely populated, intermediate, excited state is comparable to the direct excitation - after the excitation rates are weighted by their respective population densities - then the intermediate state must be included in the brackets of equation (1). For example, the stepwise excitation rate out of the $1s_5$ metastable-atom state into the $3p_9$ state, which subsequently relaxes into the $1s_5$ metastable-atom state resulting in 420.1 nm emission ($k^M_{420.1}$), is 6 orders of magnitude greater than the direct excitation rate from the ground state into the $3p_9$ state, and subsequent relaxation into the $1s_5$ state ($k^o_{420.1}$), for the range of electron density explored here and must be included in equation (1) despite the limited population of metastable-atoms. Thus, for a first-order correction, the $1s_5$ metastable-atom state is included as a source in equation (1) for interpreting 420.1 nm emission. The electron transitions associated with relevant photon emission are now written in terms of the two greatest atomic argon populations - the ground state and the first metastable-atom state ($1s_5$) that will serve as the only intermediate state in the analysis of an argon plasma employed here.

Interpretation of equation (1) largely depends on the excitation rates and ultimately the EEDF used in the calculation of these rates. Both the analysis performed here and the analysis performed in [8, 9, 19] include a second source term in equation (1) for stepwise excitation from the first metastable level $1s_5$; however, the ellipsis in equation (1) indicates where the two analyses differ: The analysis in [8, 9, 19] explicitly includes tertiary source terms in equation (1) corresponding to the second metastable-atom state ($1s_3$) and the resonant states ($1s_4$ and $1s_2$). This approach has been used to determine both metastable-atom density from an observed branching ratio of the $2p_x \rightarrow 1s_y$ transitions [9] and an effective electron temperature from a 420.1–419.8 nm emission-line-ratio technique [19]. All of the excited states of argon must be included in equation (1) for the equality to hold; however, the works performed in [8, 9, 19] have shown that the use of only four intermediate states are sufficient to accurately describe a low-temperature argon plasma. A major indication of our analysis here is that only one intermediate state may be necessary.

Equation (1) is further simplified if stepwise excitation to an upper state i has a negligible rate compared to direct excitation to the state, i.e. there is only one source term in equation (1), as is the case for the $3p_5$ state that produces 419.8 nm emission. The stepwise excitation rate from the $1s_5$ metastable-atom state into the $3p_5$ state leading to 419.8 nm emission ($k^M_{419.8}$) is much smaller than the corresponding direct excitation rate ($k^o_{419.8}$) and is ignorable in the regime discussed here. Note that $k^o_{419.8} \approx k^o_{420.1}$ [22] and is not included in figure 1 for clarity; this $k^o_{419.8} \approx k^o_{420.1}$ simplification will be used in equation (3). Assuming the ratio of the radiation trapping terms to be unity and the geometrical factors K are wavelength independent, the observed emission-line ratio is

$$R = \frac{I_{420.1}}{I_{419.8}} = \frac{k^o_{420.1}(\epsilon)}{k^o_{419.8}(\epsilon)} + \frac{n_M}{n_o}\frac{k^M_{420.1}(\epsilon)}{k^o_{419.8}(\epsilon)} = 1 + \frac{n_M}{n_o}\left(\frac{k^M_{420.1}(\epsilon)}{k^o_{419.8}(\epsilon)}\right) \quad (3)$$

This expression for observed emission-line ratio now explicitly depends on normalized metastable-atom density and, through the excitation rate ratio, implicitly on metastable-atom density, electron density, and reduced electric field. Because the last term in equation (3) is always positive, the emission-line ratio in principle cannot be less than unity, which is always the case in the post-transient stage of the pulse discussed here.

3. Experimental set-up

Figure 2 is a schematic of the experimental set-up. Spectrally pure argon entered the chamber through a mass flow controller at 30.0 sccm and was manually throttled by a butterfly valve to achieve a pressure of 1 ± 0.1 Torr. The positive column studied in this work was produced by a 40μs-duration, 2.0 kV-height square-wave voltage pulse at a repetition rate of 500 Hz. The repetition rate was chosen to ensure that the pulse occurs frequently enough to maintain a stable plasma but occurs infrequent enough that the metastable-atom state depopulates before the onset of the next voltage pulse. Multiple diagnostic measurements were sampled synchronously at positions on the cylindrical axis of a 300 mm Pyrex tube with a 2.54 cm inner diameter. The plasma was assumed to uniformly fill the entirety of the tube. The line of sight for OES and LAS measurements intersected perpendicularly the cylindrical axis

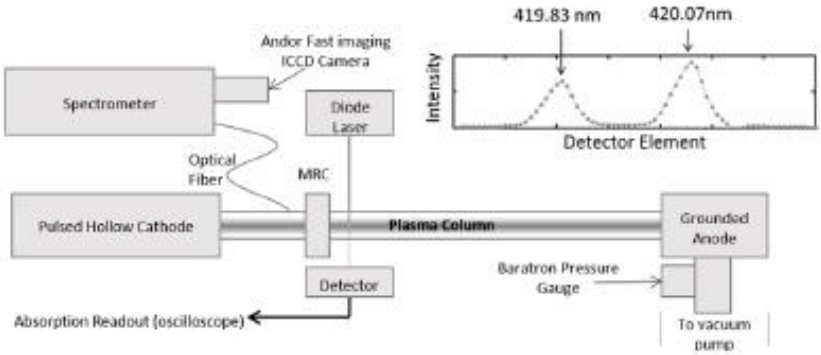

Figure 2. Three diagnostics OES, MRC, and LAS are placed perpendicular to the cylindrical axis of the discharge so they all probe identical plasma. Inlay: The 419.8 nm and 420.1 nm emission lines are shown at an arbitrary moment during the pulse. The Gaussian-like distributions shown do not overlap, permitting a true emission profile to be straightforwardly obtainable.

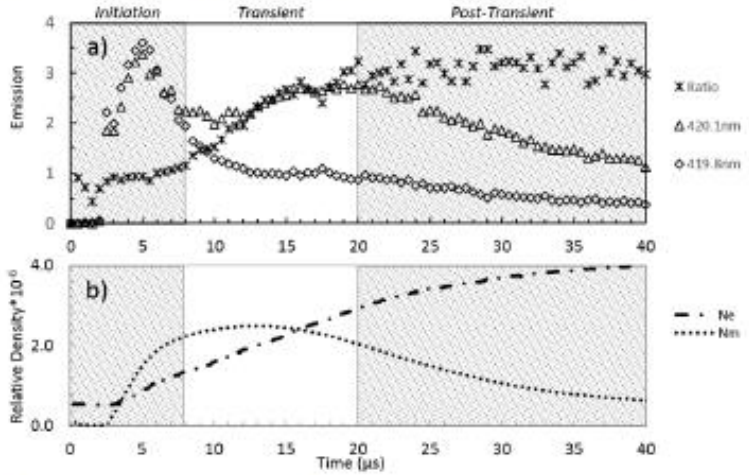

Figure 3. (a) The observed emission intensity of the argon 420.1 nm (triangle) and 419.8 nm (diamond) emission lines and their ratio (asterisk) are plotted on the y axis as functions of time in arbitrary units. Time $t = 0$ is defined as the time at which the voltage is applied. The emission ratio can be used to divide the pulse into three distinct regions: (1) The initiation stage; (2) The transient stage; and (3) The post-transient stage. The 420.1 nm emission dominates the 419.8 nm emission in the post-transient stage discussed here. (b). Relative metastable-atom and electron densities are normalized to chamber pressure ($3.22^{*}10^{16}$ cm^{-3}), which is assumed constant throughout the experiment, and shown as functions of time. Textured trend lines are shown instead of raw data for clarity. The relative electron density is greater than the relative metastable-atom density in the post-transient stage of the discharge.

in the positive-column region of the discharge to probe the plasma diameter.

3.1. Optical emission spectroscopy

Light from the positive-column region was collected by a 6.8 mm-core diameter fiber bundle that terminated at the 200 μm entrance slit of a 0.5 m Jobin Yvon spectrometer equipped with a 2400 lines/mm diffraction grating. Diffracted light is focused on the detecting elements of a gated intensified Andor iStar ICCD camera with an adjustable optical gate width held at 500 ns throughout the course of these experiments. The camera is triggered by a digital delay generator in order to precisely time the sampling of the plasma with respect to the applied voltage pulse. The spectrograph has dispersion better than 0.1 Å per detector element (pixel) which allowed both emission lines to be sufficiently resolved, without the need of a de-convolution step as shown in the inset of figure 2. Background-corrected observed emission intensities from the camera and the emission-line ratio are presented in figure 3 as a function of time. Significant emission levels do not occur until 3 μs, before which there is significant uncertainty in the emission ratio. Three different parts of the voltage pulse are examined separately as indicated by background shading in figure 3 and called the initiation, transient, and post-transient phases of the discharge. Each is distinguished by the magnitude (small or large) and slope (zero or non-zero) of the observed emission ratio. While the equation (3) offers insight into all three of stages of the voltage waveform, interpretation of the initiation and transient stages is beyond the scope of this work's validation of the model and numerical analysis of [22] and those interpretations will be discussed in future works.

3.2. Diode laser absorption spectroscopy

Laser light provides atoms in the metastable-atom state with the excitement energy required to populate the $2p_8$ state. The laser wavelength is scanned on either side of 801.5 nm to identify a maximum in the absorbed signal to determine the $1s_5$ metastable-atom density in the plasma. By averaging the metastable-atom distribution over the entire volume of the plasma column, and temporally resolving intensity of the tunable diode laser beam by a detector isolated from electrostatic noise, the density of the metastable-atom state can be determined by the Beer-Lambert law:

$$I(t) = I_o e^{-K(t)\Delta x} \tag{4}$$

where $I(t)$ is the intensity of the laser light at time t, I_o is the intensity of the laser light in the absence of metastable-atoms, Δx is the line-integrated path in the plasma, and $K(t)$ is given by

$$K(t) = \frac{1}{\lambda_{mfp}} \cong A_{21}\frac{\lambda^2}{8\pi}g(\nu)\frac{g_2}{g_1}n_M(t) \tag{5}$$

The Einstein coefficient A_{21} characterizes the transition of electrons into the $2p_8$ state from the metastable-atom state, λ characterizes the incident radiation (801.5 nm), and $g(\nu)$ is a function that characterizes the line shape of the absorbing species. g_2 and g_1 are the statistical weights of the $2p_8$ and $1s_5$ states, respectively, and our objective is to determine n_M, the density of the metastable-atom state. The maximum metastable-atom density, as shown in figure 3, is $n_M \sim 8 * 10^{10}\,\mathrm{cm}^{-3}$.

3.3. Microwave resonant cavity

Electron density was obtained using a metal microwave resonant cavity that surrounded the Pyrex tube. An antenna couples the TM_{010} mode into the cavity. The frequency of the emitted radiation is swept to identify the vacuum-cavity-resonance frequency in the absence of plasma. The applied frequency ω is then swept during the plasma duration to observe how the resonant frequency changes during a discharge. At any time, the shift in resonance frequency that is attributable to the presence of plasma is proportional to the electron density via [26]

$$\frac{\Delta f}{f} = \frac{n_e e^2}{2m_e\varepsilon_o\omega(1+\gamma^2)}, \tag{6}$$

where Δf is the shift in resonance frequency, f is the vacuum resonance frequency, e is the elementary charge, ε_o is the permittivity of free space, and $\gamma = \nu_m/\omega$ where ν_m is the momentum transfer collision frequency. Electron density increases as a function of time as shown in figure 3.

3.4. Reduced electric field

The results of Pack *et al* [27] (tabulated in Pack *et al* [28] and Raju *et al* [29]) show the relation between electron drift velocity and reduced electric field in an argon positive column. We utilize this result to estimate the reduced electric field in our positive column in the method outlined here: The plasma discharge current is resolved on a digital storage oscilloscope.

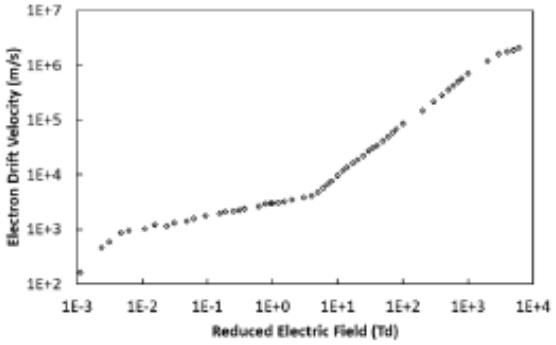

Figure 4. The relation between reduced electric field as a function of plasma current (plot similar to [27], data taken from [28]) makes measurement of E/n_o trivial.

This current is then used to determine the discharge current density J by assuming the plasma fills the entire cross-sectional area of the Pyrex tube. This current density is then converted into a drift velocity via

$$J = en_e v_d, \tag{7}$$

where J is the current density of the plasma, e is the magnitude of the electron charge, n_e is the density of the electrons measured by the microwave cavity and v_d is the average (fluid) drift velocity of the electron population. This equation assumes the ion contribution to the current density is negligible. The results of Pack *et al* [28] (reproduced in figure 4) are then used to relate the drift velocity to the reduced electric field.

4. Predictive nature of the model

The measurement of reduced electric field E/n_o, electron density n_e, and metastable-atom density n_M, are combined with equation (2) to infer the values of the excitation rates at each time sample throughout the pulse. Documenting where this model agrees with the experimental data offers insight into the experimental conditions.

Because only the post-transient stage conditions are consistent with the limiting cases of Adams *et al* [22], only this stage of the discharge will be interpreted here. During the post-transient stage of the discharge, $20\,\mu s < t < 40\,\mu s$, when the electron density and, consequently, electron–electron collisions are increasing, a greater number of electrons become available in the positive column for direct excitation of ground state argon atoms. During this stage, the experimentally relevant excitation rates are expected to approach the predicted excitation rates calculated in the negligible-metastable-atom-density (n_M) limit (figure 3 of [22]), thereby lending confidence to the use of the predicted excitation rates in accurately predicting the observed emission line throughout the post-transient stage. Adequate evidence for this logic is presented in figure 5 where the experimentally observed emission-line ratio (asterisks) as a function of time is completely bounded by the two sets of predicted emission-line ratio values for relative electron density $n_e/n_o = 10^{-6}$ (squares) and $n_e/n_o = 10^{-5}$ (triangles), where each set uses the predicted excitation rate

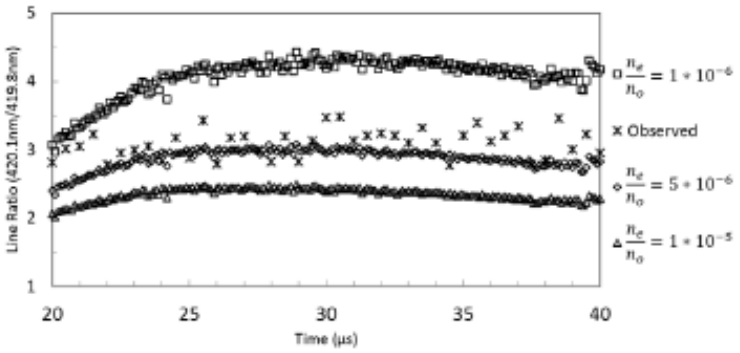

Figure 5. Predicted emission ratios are shown in the negligible—n_M limit. The predictions for normalized electron density $n_e/n_o = 10^{-5}$ (triangles) and $n_e/n_o = 10^{-6}$ (squares) under-predicts and over-predict the observed emission ratio (asterisks). The inferred excitation rate for the $n_e/n_o = 5 * 10^{-6}$ (diamonds) agrees well with the observed values $n_e/n_o \approx 3 * 10^{-6}$ as expected.

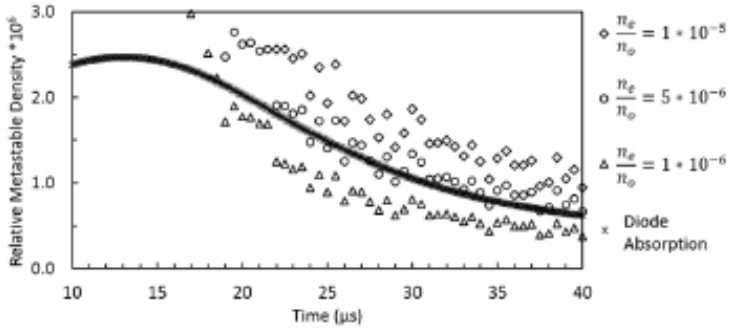

Figure 6. Predicted values for post-transient metastable-atom density. The predictions for $n_e/n_o = 10^{-5}$ (diamonds) and $n_e/n_o = 10^{-6}$ (triangles) over-predict and under-predict, respectively, the actual metastable-atom densities as expected. The inferred excitation rate for $n_e/n_o = 5 * 10^{-6}$ (circles) agrees with the observed values within experimental uncertainty in the post-transient region.

prescribed by the specific relative-electron-density value. Seeing good agreement between the observed emission-line ratio as a function of time with a prediction of emission-line ratio as a function of time based on an interpolated value of excitation rate would reinforce the confidence in this logic, so this interpolation is carried out. The two predicted excitation rates for $n_e/n_o = 10^{-6}$ and $n_e/n_o = 10^{-5}$ are averaged to produce a predicted excitation rate for the case $n_e/n_o \sim 5 * 10^{-6}$ (diamonds). It is noted that the observed value of $n_e/n_o \approx 3 * 10^{-6}$ is consistent with the $n_e/n_o \sim 5 * 10^{-6}$ within experimental uncertainty. Suitably, the thus-interpolated $n_e/n_o \sim 5 * 10^{-6}$-predicted emission-line ratio is consistently slightly below the $n_e/n_o \approx 3 * 10^{-6}$ observed values of emission-line ratio and in agreement within experimental uncertainty. Therefore, the assumption has been validated that the inferred value of the electron density is a function of both the observed emission-line ratio R and the reduced electric field E/n_o as long as inelastic processes between metastable-atoms and electrons can be ignored. Validating this assumption implies that this model is able to predict either electron density or metastable-atom density from observed emission-line ratio. As long as the metastable-atom densities are sufficiently low, the ratio of excitation rates $\left(\frac{k^o_{419.8}}{k^M_{420.1}}\right)$ is no longer a function of metastable-atom density and the observed emission-line ratio expression in equation (3) can be used to determine the normalized metastable-atom density $\frac{n_M}{n_o}$ as a function of reduced electric field and electron density.

$$\frac{n_M}{n_o} = (R-1)\left(\frac{k^o_{419.8}}{k^M_{420.1}}\right). \tag{8}$$

The observed emission-line ratio R, combined with an excitation rate ratio taken from [22] for a given electron density and reduced electric field, can predict the metastable-atom density in the plasma. Note that all three of these factors have an implicit time dependence.

Further simplification may arise here since the stepwise excitation rate constant k^M_{420} remains relatively unchanged over a broad range of reduced electric field and electron density in the negligible — n_M limit [22]. The comparison between the predictions from equation (8) and experimental data is shown in figure 6. According to figure 3 after 20 μs, the electron

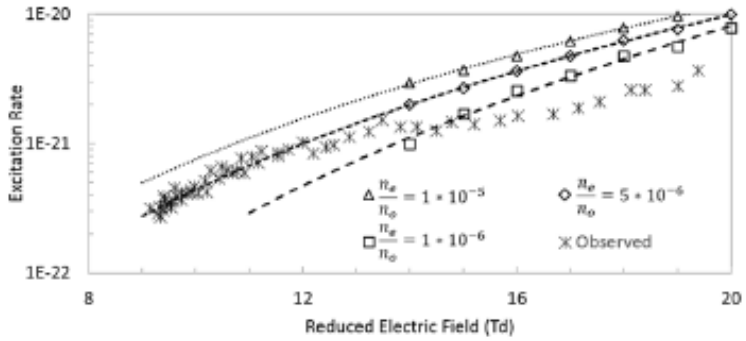

Figure 7. Observed and theoretical direct excitation rates for 0 μs < t < 40 μs. The asterisks are experimental data using equation (9) while the hollow points are data extracted from Adams *et al* [22]. The resulting trend lines are of the form $k^o_{419.8} = \alpha(E/n_o)^\beta$ where α and β are fitting parameters. The post-transient stage is associated with E/n_o < 14Td.

density sufficiently exceeds the metastable-atom density and the electron can be considered the dominant species in determining excitation rates. The observed metastable-atom density agrees, within uncertainty, with the predicted density as can be seen in figure 6.

Just as the model was used to predict the ratio of argon emissions, we can re-arrange equation (3) to gain an experimental measure of the direct-excitation rate and compare our experimental values to the direct-excitation rates extracted from [22]. Once again, this is most valid in the post-transient region; however, this model may be tested in the earlier stages of the pulse if appropriate excitation rates are known. Manipulation of equation (3) gives

$$k^o_{419.8} = \frac{n_M k^M_{420.1}}{n_o(R-1)}, \qquad (9)$$

where the value of the stepwise excitation rate is given in the post-transient region by the numerical model [22]. Both the theoretical values [22] and experimental values are presented in figure 7. The analytical form of the excitation rates $k^o_{419.8} = \alpha(E/n_o)^\beta$ where α and β are fitting parameters is empirical. Experimental excitation rates agree with the theoretical calculations, within experimental uncertainty, in the post-transient stage (E/n_o <14 Td).

5. Conclusion

These findings support the correlation suggested in Adams *et al* [22] between metastable-atom density, electron density, reduced electric field, and the 420.1–419.8 nm emission-line ratio. We have demonstrated the ability to accurately estimate metastable-atom density if the reduced electric field, electron density, and the 420.1–419.8 nm emission-line ratio are known by assuming the EEDF [22]. Once validated with the knowledge of an EEDF, this model can be used as a substitute for one of the diagnostics for a wide range of electron density, metastable-atom density, and reduced electric field. Validation of the model in the earlier stages of the discharge, 0 μs < t < 20 μs, is currently underway. Future experiments to validate this model in the initiation and transient phases are planned. It has been suggested in separate analyses that the observed emission-line ratio less than unity is indicative of high reduced electric field E/n_o >500 Td [22] or high-energy electrons of energy > 30 eV. Validation of the model over a range of metastable-atom density may be possible with the addition of gasses such as N_2 [30] or H_2 [21] that have been shown to decrease the argon metastable-atom density, or the addition of SF_6, Cl_2, or BCL_3 [31] that have been shown to increase argon metastable-atom density.

The accuracy and ability of this model to be used as a diagnostic tool is limited primarily by the known values of the excitation rates k^i_{ij}. In the metastable-atom density predictions of figure 7, the excitation rates provided by the model [22] for the order-of-magnitude values of electron density bound the observed metastable-atom densities after 20 μs and lead to predicted metastable-atom density within a factor of 2. The metastable-atom density predicted by the inferred case for a relative electron density $n_e/n_o = 5 * 10^{-6}$ are accurate within 40% for all sample-times after 20 μs. The average error across the sample-times however is less than 10%. The availability in the literature of excitation rates is limited, requiring the interpolation of the reaction rates in the manner adopted in section 5.

Slight systematic error is expected in this model however because the optical emission cross-sections used in [22] are measured at 5 milliTorr. The optical emission cross-section of the 451.1 nm decay channel (also out of the $3p_5$ state) has been shown to rise slightly (less than a factor of 2) between 5 and 15 milliTorr [23]. Because of these factors, the emission ratio and, consequently, the metastable-atom density will be underestimated in this model, however, these errors are comparable to the error bars associated with the determination of metastable-atom density imposed by the coarseness of the numerical model.

Acknowledgments

The authors gratefully acknowledge financial support of this work by the US Department of Energy Office of Fusion Energy Sciences (DE-SC0001939). The research of VID has

also been partially supported by a National Research Council Research Associateship Award at AFRL and by ITMO Grant No. 713577.

References

[1] Greenburg K E and Hebner G A 1993 Electron and metastable densities in parallel plate radiofrequency discharges *J. Appl. Phys.* **73** 8126

[2] McMillin B K and Zachariah M R 1995 Two-dimensional argon metastable density measurements in a radio frequency plasma reactor by planar laser-induced fluorescence imaging *J. Appl. Phys.* **77** 5538

[3] Millard M W, Yaney P P, Ganguly B N and DeJoseph C A 1998 Diode laser absorption measurements of metastable helium glow discharges *Plasma Sources Sci. Technol.* **7** 389–94

[4] Belostotskiy S G, Ouk T, Donnelly V M, Economou D J and Sadeghi N 2011 Time and space-resolved measurements of Ar($1s_5$) metastable density in a microplasma using diode laser absorption spectroscopy *J. Phys. D: Appl. Phys.* **44** 145202

[5] Vitelaru C, Lundin D, Stancu G D, Brenning N, Bretagne J and Minea T 2012 Argon metastables in HiPIMS: time-resolved tunable diode-laser diagnostics *Plasma Sources Sci. Technol.* **21** 025010

[6] Niermann B, Böke M, Sadeghi N and Winter J 2010 Space resolved density measurements of argon and helium metastable atoms in radio-frequency generated He-Ar micro-plasmas *Eur. Phys. J.* D **60** 489–95

[7] Zhu X M and Pu Y K 2010 A simple collisional-radiative model for low-temperature argon discharges with pressure ranging from 1Pa to atmospheric pressure: kinetics of Paschen 1s and 2p levels *J. Phys. D: Appl. Phys.* **43** 015204

[8] Boffard J B, Jung R O, Lin, C C and Wendt A E 2010 Optical emission measurements of electron energy distributions in low-pressure argon inductively coupled plasmas *Plasma Sources Sci. Technol.* **19** 065001

[9] Boffard J B, Jung R O Lin C C and Wendt A E 2009 Measurement of metastable and resonance level densities in rare-gas plasmas by optical emission spectroscopy *Plasma Sources Sci. Technol.* **18** 035017

[10] Schulze M, Yanguas-Gil A, von Keudell A and Awakowicz P 2008 A robust method to measure metastable and resonant state densities from emission spectra in argon and argon-diluted low pressure plasmas *J. Phys. D: Appl. Phys.* **41** 065206

[11] Mariotti D, Shimizu Y, Sasaki T and Koshizaki N 2006 Method to determine argon metastable number density and plasma electron temperature from spectral emission originating from four 4p argon levels *Appl. Phys. Lett.* **89** 201502

[12] Wang S, Wendt A E, Boffard J B, Lin C C, Radovanov S and Persing H 2013 Noninvasive, real-time measurements of plasma parameters via optical emission spectroscopy *J. Vac. Sci. Technol.* A **31** 021303

[13] Lee Y K, Moon S Y, Oh S J and Chung C W 2011 Determination of metastable level densities in a low-pressure inductively coupled argon plasma by the line-ratio method of optical emission spectroscopy *J. Phys. D: Appl. Phys.* **44** 285203

[14] Navrátil Z, Trunec D, Hrachová V and Kaňka A 2007 Collisional-radiative model of neon discharge: determination of E/N in the positive column of low pressure discharge *J. Phys. D: Appl. Phys.* **40** 1037–46

[15] Kano K, Suzuki M and Akatsuka H 2000 Spectroscopic measurement of electron temperature and density in argon plasmas based on collisional-radiative model *Plasma Sources Sci. Technol.* **9** 314–22

[16] Zhu X M, Pu Y K, Celik Y, Siepa S, Schüngel E, Luggenhölscher D and Czarnetzki U 2012 Possibilities of determining non-Maxwellian EEDFs from the OES line-ratios in low-pressure capacitive inductive plasmas containing argon and krypton *Plasma Sources Sci. Technol.* **21** 024003

[17] Siepa S, Danko S, Tsankov, T V, Mussenbrock T and Czarnetski U 2014 On the OES line-ratio technique in argon and argon-containing plasmas *J. Phys. D: Appl. Phys.* **47** 445201

[18] Jung R O, Boffard J B, erson L W and Lin C C 2007 Excitation into $3p_5 5p$ levels from the metastable levels of Ar *Phys. Rev.* A **75** 052707

[19] Boffard J B, Jung R O, Lin C C, Aneskavich L E and Wendt A E 2012 Argon 420.1–419.8 nm emission line ratio for measuring plasma effective electron temperatures *J. Phys. D: Appl. Phys.* **45** 045201

[20] DeJoseph C A, Demidov V I and Kudryavtsev A A 2005 Modification of a nonlocal electron energy distribution in a bounded plasma *Phys. Rev.* E **72** 036410

[21] Fox-Lyon N, Knoll A J, Franek J B, Demidov V I, Godyak V A, Koepke M E and Oehrlein G S 2013 Determination of Ar metastable atom densities in Ar and Ar/H2 inductively coupled low-temperature plasmas *J. Phys. D: Appl. Phys.* **46** 485202

[22] Adams S F, Bogdanov E A, Demidov V I, Koepke M E, Kudryavtsev A A and Williamson J M 2012 Metastable atom and electron density diagnostic in the initial stage of a pulsed discharge in Ar and other rare gasses by emission spectroscopy *Phys. Plasmas* **19** 023510

[23] Boffard J B, Lin C C and DeJoseph C A 2004 Application of excitation cross sections to optical plasma diagnostics *J. Phys. D: Appl. Phys.* **37** R143–R161

[24] Adams S F, Miles J, Laber A, Demidov V I, Williamson J M and Tolson B 2009 Determination of argon metastable density from relative emission intensity measurements combined with optical emission cross section data *19th Int. Symp. on Plasma Chemistry Bochum*

[25] Bogdanov E A, DeJoseph C A, Demidov V I, Kudryavtsev and Serditov K Y 2007 Influence of an additional ballast volume on a pulsed ICP discharge *Plasma Sources Sci. Technol.* **16** 697–702

[26] Buschman S J and Brown S C 1957 Microwave measurements of high electron densities *Phys. Rev.* **106** 196–209

[27] Pack J L and Phelps A V 1961 Drift velocities of slow electron in helium, neon, argon hydrogen and nitrogen *Phys. Rev.* **121** 798

[28] Pack J L, Voshall R E and Phelps A V 1962 Tables of drift velocities of slow electrons in helium, neon, argon, krypton, xenon, hydrogen, deuterium, nitrogen, carbon monoxide, carbon dioxide, water vapor, nitrous oxide, and ammonia *Technical Report*

[29] Raju G G 2011 *Gaseous Electronics: Tables, Atoms, and Molecules* (Boca Raton, FL: CRC)

[30] Muñoz J, Margot J and Chaker M 2013 Argon metastable and resonant densities in a low pressure Ar–N2 inductively coupled plasma *J. Phys. D: Appl. Phys.* **46** 455205

[31] Scheller G R, Gottscho R A, Intrator T and Graves D B 1988 Nonlinear excitation and dissociation kinetics in discharges through mixtures of rare and attaching gasses *J. Appl. Phys.* **64** 4384–4397

IOP Publishing Plasma Physics and Controlled Fusion

Plasma Phys. Control. Fusion 59 (2017) 014005 (5pp) doi:10.1088/0741-3335/59/1/014005

Dynamics of atomic kinetics in a pulsed positive-column discharge at 100 Pa

J B Franek[1], S H Nogami[1], M E Koepke[1], V I Demidov[1,2] and E V Barnat[3]

[1] West Virginia University, Department of Physics and Astronomy, Morgantown, WV 26505-6315, USA
[2] ITMO University, St. Petersburg 197101, Russia
[3] Lasers, Optics, and Remote Sensing Department, Sandia National Laboratories, 1128, Albuquerque, NM 87123, USA

E-mail: jfranek@mix.wvu.edu

Received 28 July 2016, revised 22 August 2016
Accepted for publication 25 August 2016
Published 18 October 2016

Abstract

Temporal measurements of the electron density, metastable-atom density, and reduced electric field demonstrate that four orders of magnitude variation in the dynamic range of the electron-atom collision-induced excitation rates takes place during the 2.0 kV height, 40 μs duration repeating pulse applied to a 100 Pa (1 Torr), argon positive column in a hollow-cathode discharge. Correlation between metastable-atom density and emission-line ratio is demonstrated to be sufficiently reliable to infer one quantity based on the measurement of the other quantity during the Initiation, Transient, and Post-Transient spectroscopic stages of the pulse. Observed emission-line ratio and the predicted emission-line ratio are in quantitative agreement with each other in the Transient and Post-Transient stages of the discharge and are in qualitative agreement with each other in the Initiation stage of the discharge. Reasonable assumptions regarding the interpretation of the electron energy probability function (EEPF), as it starts off being Druyvesteyn and becomes more Maxwellian later with the increasing electron density, is key to interpreting the correlation and explaining the temporal behavior of the emission-line ratio in all stages of the discharge.

Keywords: optical emission spectroscopy (OES), reduced electric field, metastable argon atoms, emission-line ratio, pulsed DC plasma

(Some figures may appear in colour only in the online journal)

1. Introduction

Diagnostic convenience and sensitive discrimination in detecting the presence of metastable atoms, having density N_m, motivated the development of a technique for turning an emission-line ratio measurement into a unique value of metastable-atom density [1] for weakly ionized (electron/neutral-atom ratio $N_e/N \sim 10^{-6}$) plasma. Properly interpreting emission-line ratio measurements to get metastable-atom density requires stage-to-stage knowledge of the excitation-rate dependence on the electron energy probability function (EEPF) from a collisional-radiative model [2] as well as knowledge of the stepwise excitation from metastable atoms [3, 4]. Based on direct and stepwise atomic excitation, Adams *et al* [5] predict electron-atom collision-induced excitation rates to the $3p_9$ and $3p_5$ states (in Paschen's notation), which lead to 420.1 nm and 419.8 nm emission, respectively, as a function of reduced electric field E/N for a specific value of electron density N_e and metastable density N_m. This optical method has been shown [6] to be useful for obtaining Ar metastable densities with satisfactory accuracy and precision at different plasma pressures and with H_2 gas additions, in agreement with rigorous quantitative diagnostics seen in literature.

Franek *et al* [7] compare emission-line-ratio predicted metastable-atom density from the numerical model of Adams *et al* [5] with metastable-atom density measurements. In the experiment, the plasma-discharge current and the electron density are combined to obtain electron drift speed which, in turn, is translated into values of reduced electric field using the relationship reported by Pack *et al* [8]. By applying the results of the numerical model [5] to 100 Pa plasma, the WVU–SNL collaboration showed how metastable-atom density correlates with reduced electric field and emission-line ratio in the late

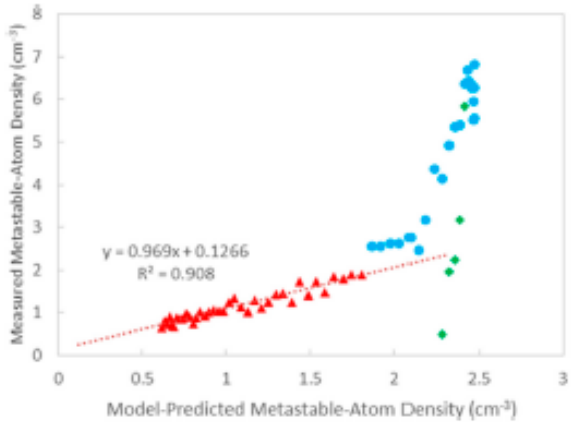

Figure 1. Measured metastable atom density versus model-predicted metastable atom density for all stages of the pulsed positive column. Predictions are made using the calculated reaction rates of [5] assuming metastable-atoms have no effect on the EEPF. Green diamonds, blue circles, and red triangles represent the Initiation, Transient, and Post-Transient stages respectively. The comparison between densities in the Post-Transient stage show a nearly one-to-one relation between experiment and theory. Both axes are 10^6 times actual values.

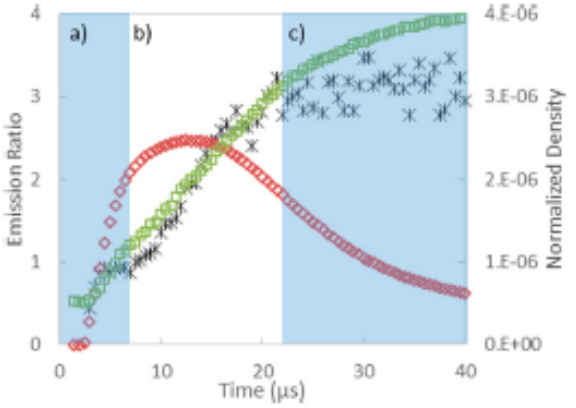

Figure 2. The observed emission-line ratio (black asterisks) is used to separate the plasma into three stages: (a) the Initiation stage, (b) the Transient stage, and (c) the Post-Transient stage. Electron density (green squares) and metastable-atom density (red diamonds) are normalized to the neutral argon background ($3.22 * 10^{22}$ cm^{-3}).

stage of a 1 Torr pulsed argon discharge [7]. The relationship can be used to predict the metastable-atom density from the emission-line ratio during the earlier two stages (Initiation and Transient) of a pulsed discharge, reducing the need for determining metastable-atom density with a diode laser. We found that inferring metastable-atom density from emission-line ratio measurements using predicted excitation rates for a given value of reduced electric field works even in plasmas having orders-of-magnitude different pressures for the same range because, here, the excitation rate is independent of pressure.

In this paper, we consider the dynamics of the atomic excitation and ionization that take place as the neutral gas state changes into the weakly-ionized state in the pulsed positive-column discharge. We present quantities of interest in all stages of a pulsed argon discharge, emphasizing the correlations, and compare to models. Correlations using the numerical modeling [5] leading to a metastable-atom diagnostic as presented in [7] in the Post-Transient stage of the discharge are outlined in section 3. We expand this model into the Initiation and Transient phases of the discharge in section 4 to further correlate the dynamics of atomic processes to observable plasma parameters in the pulsed positive column.

2. Attributes of the 100 Pa argon pulsed positive column in a hollow-cathode discharge

While a detailed description of the experimental apparatus is given in [7], salient details of the experiment are outlined here. Spectrally pure argon enters the cylindrical chamber (Pyrex tube) through a mass flow controller at 30.0 sccm. Chamber pressure is controlled by a butterfly valve. A 40 μs duration, 2.0 kV height square-wave voltage pulse is utilized here to produce the positive column studied in this work. The positive column is pulsed at a repetition rate of 500 Hz, in order for the metastable-atom state to depopulate before the next voltage pulse.

The diagnostics employed in this work are sampled synchronously along on the cylindrical axis of the 30 cm long Pyrex tube with a 2 cm inner diameter. Optical emission spectroscopy (OES) and tunable diode laser absorption spectroscopy (TDLAS) measurements are line-integrated across the plasma diameter. Plasma emissions are collected by a 6.8 mm core fiber bundle that terminates at the 200 μm entrance slit of a 0.5 m spectrometer, which is equipped with a 2400 groove mm^{-1} grating and 1024 $\times$ 1024 pixel ICCD camera. Laser light (centered around 801.5 nm) from a tunable diode laser is absorbed by metastable-atoms in the $1s_5$ state to populate the $2p_8$ state. The laser light is tuned (~0.1 Å) to find the wavelength of maximum absorption; this absorbed signal is proportional to the density of the metastable-atoms in the $1s_5$ state. Metastable-atom density is calculated by assuming the plasma uniformly fills the discharge tube. An aluminum microwave resonant cavity is utilized here to determine electron density. A microwave signal is applied to an axial 18 AWG copper antenna to excite the TM_{010} mode in the resonant cavity. The microwave signal is then swept to determine the cavity resonant frequency without plasma. Electron density (electron collision frequency) is proportional to the shift in resonant frequency (decrease in signal amplitude) due to plasma electrons. The electron collision frequency is proportional to the width of the resonance peak as discussed in [9].

3. Correlation between metastable-atom density and emission-line ratio is demonstrated

A brief overview of previous work is offered here to introduce the reader to the topic and make the conclusions in this work more meaningful. We utilize the argon 420.1 nm and 419.8 nm emissions, which are produced by the $3p_9$–$1s_5$ and $3p_5$–$1s_4$

Table 1. Coarse descriptors for emission-line ratio (R) electron density (N_e), metastable-atom density (N_m), reduced electric field (E/N), and direct excitation rate of the $3p_5$ state are displayed here for the three stages of the discharge.

Stage	Ratio	N_e	N_m	E/N	k^o_{419} ($m^3 s^{-1}$)
Initiation	1	Low	Low	High	$>10^{-20}$
Transient	1–3	Medium	High	Medium	10^{-20}–10^{-21}
Post-Transient	3	High	Medium	Low	$<10^{-21}$

transitions (in Paschen's notation) respectively. These transitions have weak optical oscillator strength, which lead to insignificant reabsorption of the emission lines [10] and which ultimately reduces the necessary algebraic overhead required to achieve credible results. This is evident in figure 1 where the emission-line-ratio inferred metastable-atom density is compared to measurements via TDLAS. Excellent agreement between the model-predicted and observed metastable-atom density is shown for the latter stage of the discharge (red triangles) and is emphasized by the trendline. While a comprehensive discussion of the assumptions made in the model may be found in [7], only the key findings are reproduced here. The metastable-atom density in the latter-half of the discharge, the Post-Transient stage, is given by

$$\frac{n_m}{n_o} = (R-1)\left(\frac{k^o_{419}}{k^m_{420}}\right), \quad (1)$$

where n_m and n_o are the argon metastable-atom and argon ground state densities, R is the observed emission ratio, k^o_{419} is the direct excitation rate into the $3p_5$ state that leads to 419.8 nm emission, and k^m_{420} is the stepwise excitation rate into the $3p_9$ state that leads to 420.1 nm emission.

Deviations between the model-predicted metastable-atom density and observed metastable-atom density are explained through proper analysis of the assumptions in the modeling. Adams *et al* [5] predicts electron-atom collision-induced excitation rates as a function of reduced electric field, E/N, for a specific value of electron density, N_e, and metastable-atom density, N_m. The predictions of metastable-atom density in figure 1 assume a Druyvesteyn EEPF with normalized electron density $N_e/N_o = 5 * 10^{-6}$. Effects of collisions between electrons and metastable-atoms are not included in determining this EEPF to best match the depleted metastable-atom conditions in the latter half of the discharge. The model-predicted metastable-atom density agrees with the measured metastable-atom density within 20% in this stage of the discharge. The trendline for the red triangles shows the one-to-one relationship (slope = 1, $R^2 = 0.9$) between the predicted and observed quantities, demonstrating qualitative agreement. The y-intercept indicates that, on average, the model under-predicts the experimentally determined normalized metastable-atom density by ~10^{-7} in the latter half of the 40 μs pulse width.

As one should expect from the presence of metastable-atoms and their consequential effect on EEPF shape [11], the model grossly under-predicts the metastable-atom density in the earlier stages of the discharge. The abundance of metastable-atoms is expected to produce high energy electrons [11] which favor direct excitation, i.e. increasing the direct excitation rate k^o_{419} leads to an increased metastable-atom density according to equation (1). A larger percentage of electrons with energies higher than those predicted by considering electron–electron or electron-metastable collisions, i.e. suprathermal electrons, in the earlier times of the pulse may lead to larger departures from the model in this stage. With this in mind, examination of the 420.1/419.8 nm emission-line ratio suggests the discharge may be examined in three distinctly different stages.

These different stages of the voltage pulse are evaluated separately, as indicated by background shading in figure 2, and called the Initiation, Transient, and Post-Transient stages of the discharge. Each is distinguished by the magnitude (small or large) and slope (zero or non-zero) of the observed emission ratio. The three stages of the discharge can also be characterized by the other plasma parameters of interest; their coarse descriptors are given in table 1. These descriptors may be used to categorize quantitative correlations between parameters.

We emphasize here the dynamics of the atomic excitation and ionization that take place as the neutral gas state changes into the weakly-ionized state in the pulsed positive-column discharge in response to the high-voltage pulse and the accompanying current waveform (figure 3(a)). We process this current waveform and the electron-density waveform by converting them into an electron-drift-velocity waveform which is translated into the reduced-electric-field waveform, i.e. E/N versus time, (figure 3(b)). Next, this E/N waveform is converted into an excitation rate waveform (figure 3(c)) using the numerical model [5]. The four waveforms of reduced electric field, electron density, metastable-atom density, and 420.1 nm/419.8 nm emission-line ratio are correlated using the numerical model [5–7]. The four orders of magnitude variation in the dynamic range of the electron-atom collision-induced excitation rates and emission-line ratio are inferred from temporal measurements of the co-dependent plasma parameters: electron density, metastable-atom density, reduced electric field, and emission-line ratio. Figure 2 shows the co-dependent parameters as a function of time during the discharge pulse. Using these correlations, the direct excitation rate for 419.8 nm emission is determined via emission-line ratio measurement [7].

4. Interpretations

The above experiment is performed over a range of pressures (100–500 Pa) to produce figure 4 which shows the relation between reduced electric field and emission-line ratio for all

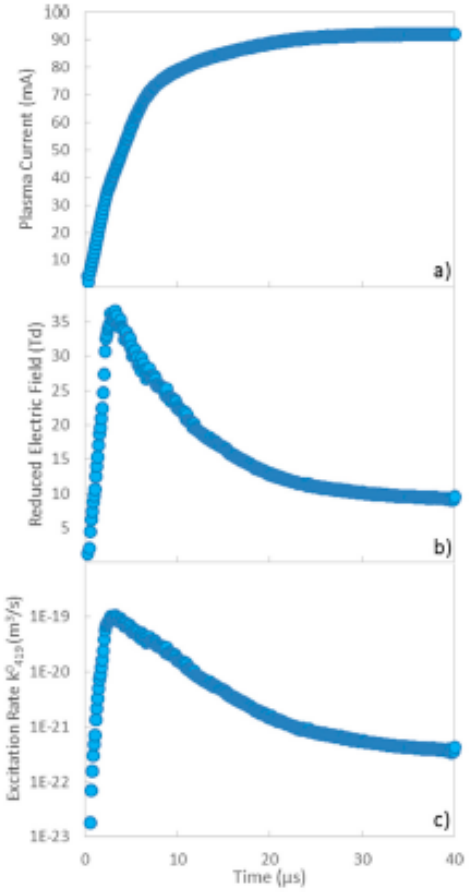

Figure 3. (a) Plasma current, (b) reduced electric field, and (c) direct excitation rate are plotted as functions of time. A −2 kV, 40 μs duration voltage pulse is applied at time $t = 0$ s.

stages of the voltage pulse. The statistical uncertainty shown in figure 2 indicates the good precision associated with the correlations observed in this work. While the temporal dynamics presented in figure 2 vary significantly with changing pressure, the physics that produce these results are the same within analogous stages, and will be elucidated by considering the three stages of the discharge separately.

4.1. Initiation stage

The Initiation stage of the discharge is defined here as the time-window before the electrons and metastable-atoms in the plasma affect the observed emission-line ratio. The applied voltage produces a high reduced-electric-field which in turn ionizes the gas and creates the metastable atoms. This stage is characterized by a static (i.e. zero slope) emission-line ratio that is often less that unity, which suggests a non-negligible population of supra-thermal electrons [12]; therefore, the resulting EEPF cannot be understood by the logic expressed in [5, 11]. The disagreement here shows the modeling of Adams *et al* [5] cannot be used when considering a non-thermal (non-Druyvesteyn) distribution of electrons.

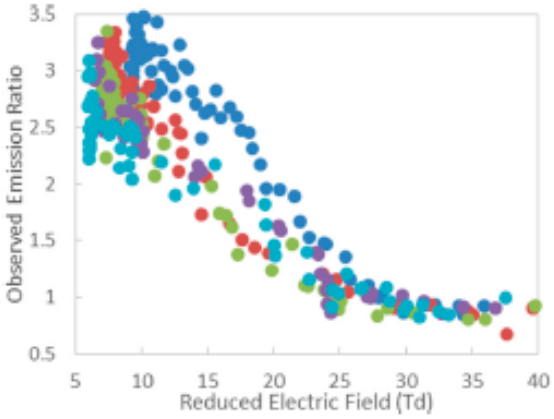

Figure 4. Observed emission ratio as a function of reduced electric field. Data taken at 1 Torr (dark blue), 2 Torr (red), 3 Torr (green), 4 Torr (purple) and 5 Torr (light blue) overlap for the range of *E/N* presented here.

4.2. Transient stage

The Transient stage of the discharge is defined here as the time-window during which the observed emission-line ratio increases due to the presence of electrons and metastable-atoms. *E/N* decreases as the ionization fraction (i.e. conductivity) gets larger. While there is agreement between the model predictions and experimental results in the Post-Transient stage, figure 1 suggests that the model is not valid in the Transient stage of the discharge. One could, however, include electron heating from metastable-atoms to expand the applicability of the model into the Transient stage [13].

4.3. Post-Transient stage

The Post-Transient stage of the discharge is defined here as the time-window during which the observed emission-line ratio is static. Metastable-atom losses become significant, thus, the metastable-atom density returns to negligible levels while electron density continues to increase causing *E/N* to further decrease. This combination of plasma parameters leads to the agreement between modeling and experiment shown in figure 1.

5. Conclusion

We acquired validation data and found a correlation between metastable-atom density, reduced electric field, and emission-line ratio [7, 13]. We re-expanded the expression of the emission-line ratio as a function of the metastable-atom density and as a function of the direct and stepwise atomic excitation rates. The expression is utilized to infer the time dependence of the metastable-atom population from the time dependence of the reduced electric field. From these results, the emission-line ratio dependence on metastable-atom density and on the stepwise excitation rate for 419.8 nm emission allow for a simplified determination of the direct excitation rate for 419.8 nm emission [7]. The time dependence of emission-line

ratio is shown to follow predictably the time dependence of metastable-atom density.

Observed emission-line ratio agrees, either quantitatively or qualitatively, with the predicted emission-line ratio throughout a pulsed discharge. Factors incorporated into the interpretation include the EEPF and the electron-atom collision-induced excitation rates. Once the reduced electric field is known, the emission-line ratio measurements yield metastable-atom density in plasmas that have similar reduced electric field, even over a range of pressures. The advantage of the emission-line ratio diagnostic is its passive implementation and its ability to faithfully replicate tunable-diode laser absorption spectroscopy measurements for determining metastable-atom density. Besides offering this utilitarian convenience for diagnosing pulsed discharges at a significantly lower diagnostic cost, these results illustrate the multi-order-of-magnitude dynamic range of the excitation rate coefficients in play in a pulsed traveling ionization wave.

Acknowledgments

The authors gratefully acknowledge financial support of this work by the US Department of Energy Office of Fusion Energy Sciences (DE-SC0001939, DE-SC0012515, and SCGSR). Office of Science Graduate Student Research (SCGSR) program is administered by ORISE which is managed by ORAU under contract number DE-AC05-06OR23100. A part of this research was performed while one author (VID) held a National Research Council Research Associateship Award at AFRL, Wright-Patterson Air Force Base, OH. Sandia National Laboratories is a multi-program laboratory operated by Sandia Corporation, a Lockheed Martin Company, for the US DOE NNSA under contract DE-AC04-94AL85000.

References

[1] Demidov V I, DeJoseph C A and Kudryavtsev A A 2006 *IEEE Trans. Plasma Sci.* D **34** 825

[2] Bates D R, Kingston A E and McWhirter R W P 1962 Recombination between electrons and atomic ions I. Optically thin plasmas *Proc. R. Soc.* A **267** 297

[3] Boffard J B, Jung R O, Lin C C and Wendt A E 2010 Optical emission measurements of electron energy distributions in low-pressure argon inductively coupled plasmas *Plasma Sources Sci. Technol.* **19** 065001

[4] Jung R O, Boffard J B, Anderson L W and Lin C C 2007 Excitation into 3p55p levels from the metastable levels of Ar *Phys. Rev.* A **75** 052707

[5] Adams S F, Bogdanov E A, Demidov V I, Koepke M E, Kudryavtsev A A and Williamson J M 2012 Metastable atom and electron density diagnostic in the initial stage of a pulsed discharge in Ar and other rare gasses by emission spectroscopy *Phys. Plasmas* **19** 023510

[6] Fox-Lyon N, Knoll A J, Franek J B, Demidov V I, Godyak V, Koepke M E and Oehrlein G S 2013 *J. Phys. D: Appl. Phys.* **46** 485202

[7] Franek J B, Nogami S H, Koepke M E, Demidov V I and Barnat E V 2015 Correlating metastable-atom density, reduced electric field and electron energy distribution in the post-transient stage of a 1 Torr argon discharge *Plasma Sources Sci. Technol.* **24** 034009

[8] Pack J L and Phelps A V 1961 Drift velocities of slow electron in helium, neon, argon hydrogen and nitrogen *Phys. Rev.* **121** 798

[9] Franek J B, Nogami S H, Koepke M E, Demidov V I and Barnat E V 2015 Reply to comment on 'Correlating metastable-atom density, reduced electric field and electron energy distribution in the post-transient stage of a 1 Torr argon discharge, Plasma Sources Sci. Technol. 24, 034009' *Plasma Sources Sci. Technol.* **25** 038002

[10] Boffard J B, Jung R O, Lin C C, Aneskavich L E and Wendt A E 2012 Argon 420.1–419.8 nm emission line ratio for measuring plasma effective electron temperatures *J. Phys. D: Appl. Phys.* **45** 045201

[11] Hagelaar G J M and Pitchford L C 2005 Solving the Boltzmann equation to obtain electron transport coefficients and rate coefficients for fluid models *Plasma Sources Sci. Technol.* **14** 722–33

[12] Boffard J B, Wang S, Lin C C and Wendt A E 2015 Detection of fast electrons in pulsed argon inductively-coupled plasmas using the 420.1–419.8 nm emission line pair *Plasma Sources Sci. Technol.* **24** 065005

[13] Franek J B, Nogami S H, Koepke M E, Demidov V I and Barnat E V in preparation

Power supply and impedance matching to drive technological radio-frequency plasmas with customized voltage waveforms

James Franek,[1] Steven Brandt,[1] Birk Berger,[1,2] Martin Liese,[3] Matthias Barthel,[3] Edmund Schüngel,[1] and Julian Schulze[1]

[1)] *Department of Physics, West Virginia University, Morgantown, West Virginia 26506-6315, USA*

[2)] *Institute for Theoretical Electrical Engineering, Ruhr-University Bochum, Germany*

[3)] *Barthel HF-Technik GmbH, Walkmühlenstrasse 16, 52074 Aachen, Germany*

(Dated: 16 March 2015)

We present a novel radio-frequency (RF) power supply and impedance matching to drive technological plasmas with customized voltage waveforms. It is based on a system of phase-locked RF generators that output single frequency voltage waveforms corresponding to multiple consecutive harmonics of a fundamental frequency. These signals are matched individually and combined to drive an RF plasma. Electrical filters are used to prevent parasitic interactions between the matching branches. By adjusting the harmonics' phases and voltage amplitudes individually any voltage waveform can be realized as a customized finite Fourier series. This RF supply system is easily adaptable to any technological plasma for industrial applications and allows the commercial utilization of process optimization based on voltage waveform tailoring for the first time. Here, this system is tested on a capacitive discharge based on three consecutive harmonics of 13.56 MHz. According to the Electrical Asymmetry Effect, tuning the phases between the applied harmonics results in an electrical control of the DC self-bias and the mean ion energy at almost constant ion flux. A comparison with the reference case of an electrically asymmetric dual-frequency discharge reveals that the control range of the mean ion energy can be significantly enlarged by using more than two consecutive harmonics.

I. INTRODUCTION

The manufacturing of many high technological products requires processing steps that involve a surface modification via plasma treatment, e.g. anisotropic dielectric etching of integrated circuits and the Plasma Enhanced Chemical Vapor Deposition (PECVD) of nano structures and of biocompatible surfaces[1–10]. The corresponding plasma sources are typically driven by a voltage oscillating in the MHz regime, which is supplied by a generator and applied to an electrode or a coil via an impedance matching network. Such single frequency capacitively and/or inductively coupled RF discharges are most frequently used in industry. The control and the optimization of the flux of the electrons, ions, and neutral radicals at the substrate surface as a function of energy is essential for these applications; thus, means of customizing the flux-energy distribution functions (FEDF) of these species are strongly required.

In capacitively coupled radio frequency (CCRF) plasmas operated at a single frequency (e.g. 13.56 MHz), such control is strongly limited. For example, the shape of the ion FEDF at the substrate cannot be customized and independent control of the mean ion energy and flux is impossible. In traditional, single-frequency systems an increase in the driving voltage amplitude results in a stronger electric field in the sheaths, thus, increasing the particle flux as well as the mean ion energy. Dual-frequency plasmas operated at two substantially different frequencies (e.g. 2 MHz and 27 MHz) provide an improved control[11–16]. This approach is based on the idea that the charged particle generation, density, and fluxes mainly depend on the amplitude of the high-frequency component, whereas the energy gain of ions in the plasma-substrate sheath mainly depends on the amplitude of the low-frequency component. However, the control of the ion FEDF is again limited due to the effects of frequency coupling and secondary electrons[11,16–19] as well as the limited control of the voltage drop across the sheaths as a function of time.

An efficient way to realize an advanced control of distribution functions and to improve their lateral uniformity across large substrates is driving RF plasmas with customized voltage waveforms[8,20–39]. The individual voltage drops across the plasma-electrode sheaths can be customized within the fundamental RF period, resulting in control of the ion and electron heating dynamics on a nanosecond timescale. Furthermore, this approach allows control of the symmetry of the discharge, which translates into a convenient method of tuning the mean ion energy at both the powered and the grounded electrode. In general, such voltage waveforms, $\tilde{\phi}(t)$, can be generated as a finite Fourier Series consisting of multiple consecutive harmonics of a fundamental driving frequency:

$$\tilde{\phi}(t) = \sum_{k=1}^{N} \phi_k \cos\left(2\pi k f t + \theta_k\right) \qquad (1)$$

Here, N is the total number of applied consecutive harmonics, f is the fundamental frequency, ϕ_k is the amplitude of the k-th harmonic and θ_k is its phase. The total amplitude of the driving voltage waveform is $\phi_{tot} = \sum_{k=1}^{N} \phi_k$. This waveform can be tailored by individually adjusting the harmonics' amplitudes and phases.

For a sufficient number of harmonics any driving voltage waveform can be generated in this way.

The idea of voltage waveform tailoring is based on earlier work of Wendt et al.[40,41] and Baloniak et al.[42], who introduced unmatched customized low frequency (kHz) voltage waveforms as a substrate bias to control the shape of the ion FEDF in high density remote plasma sources. As many manufacturers cannot modify their capacitive RF plasma reactors to include remote plasma sources, however, this technology is not widely used in industry.

Previous works on RF voltage waveform tailoring without remote sources have demonstrated its enormous potential and advantages for process control compared to conventional methods[8,24,29–31]. The recent discoveries of the Electrical Asymmetry Effect (EAE)[8,20–28,32,33,37–39] and the Slope Asymmetry Effect[35,36] in CCRF discharge driven by customized voltage waveforms solve some of the most critical limitations of plasma processing such as the lack of separate control of the ion mean energy and the ion flux at the wafer[20–23,25–27,32,33,39] as well as the lack of concept to prevent lateral inhomogeneities of the ion flux across large substrates[37].

However, all these previous works suffered from strong technical limitations caused by the absence of a multi-frequency RF power supply and impedance matching for more than 2 consecutive harmonics. The first experimental works on the EAE made use of two consecutive harmonics combined with classical dual-frequency impedance matchings[22,23,25]. While these experiments demonstrated the functionality of the EAE, its full performance - predicted to occur in the presence of multiple driving harmonics by simulations and models[27,28] - could not be tested experimentally. This was later done by Lafleur et al. using multi-frequency waveforms without impedance matching[29–32]. This simplified scheme facilitated important fundamental investigations of the particle heating dynamics and the control of distribution functions in such multi-frequency plasmas. The absence of impedance matching, however, makes practical implementations in industrial applications impossible due to high reflected powers of about 90 % and the restriction to low voltage amplitudes.

Here, we present a novel RF supply system with impedance matching that solves this important problem. It allows technological plasmas to be driven with customized voltage waveforms at low reflected powers and, therefore, allows RF voltage waveform tailoring to be used at an industrial level for the first time. Utilizing this system, we demonstrate that increasing the number of consecutive harmonics in a CCRF plasma significantly improves the performance of the EAE, i.e, the control ranges of the DC self-bias and the mean ion energy are increased significantly. This is examined by direct measurements of the DC self-bias, thereby probing the discharge asymmetry, and of the ion FEDF at the electrodes. We show that by varying the relative phases of the applied harmonics for a given total voltage amplitude the controllable ranges of the DC self-bias and the mean ion energy are increased if three instead of two consecutive harmonics are used, while the ion flux remains almost constant. These results agree with previous simulation and experimental results without impedance matching, while proving the feasibility of this technology for the plasma processing industry.

The RF supply system, which is commercially available[43], is described in detail in the next section. There, we also provide a description of the plasma source and the diagnostics as well as the model of the EAE in CCRF plasmas. The results are presented and discussed in section 3, where first the measured and modeled DC self-bias and then the ion FEDF measurements are analyzed. Finally, conclusions are drawn in the fourth section.

II. EXPERIMENTAL SETUP AND MODEL

A. Multi-frequency RF power supply and impedance matching

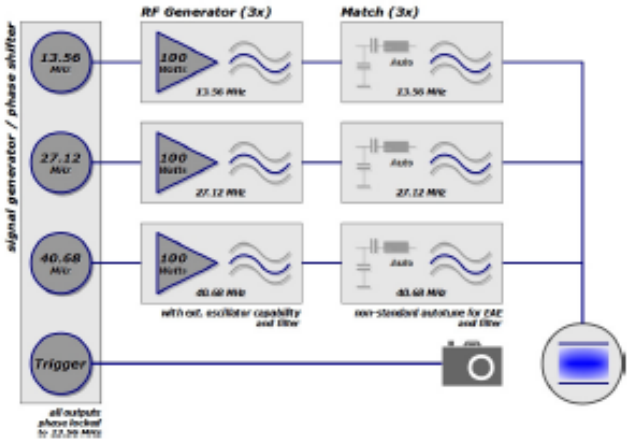

FIG. 1. Schematic of the novel multi-frequency RF power supply and impedance matching shown exemplarily for 3 consecutive harmonics of 13.56 MHz (100 W per harmonic) and including an additional phase-locked trigger output. The number of frequencies, its absolute values and maximum power levels are variable and can be customized according to the requirements of a given plasma process and reactor.

Figure 1 shows the novel multi-frequency RF power supply and impedance matching that allows technological plasmas to be driven with customized RF voltage waveforms with low reflected power for the first time. It can be combined with capacitive, inductive, or hybrid combinations of both reactor types. Existing reactors can be upgraded by adding this system without modifying the reactor itself. The multi-frequency system used in this work is shown in figure 1 and is designed to drive a CCRF discharge with 3 consecutive harmonics of 13.56 MHz with independent relative phase and voltage ampli-

tude control for each harmonic. This multi-frequency RF supply system is designed to provide a maximum degree of flexibility, i.e. it can be customized according to the requirement of a given application: the number of harmonics (1 - 8 harmonics), their absolute values (1 MHz - 200 MHz), and maximum power levels are variable and can be customized. In particular there is no principle upper power limit. This makes this RF supply system highly relevant for high power applications of CCRF discharges, where large surface areas are processed and the control of the ion FEDF at the substrate is crucial. For powers above 600 W per harmonic the required electrical filters become larger and might not be integrated into the generator and matching unit.

The multi-frequency RF supply system consists of independent matching branches, consisting of a single-frequency RF generator, an impedance matching circuit, and electrical filters, for each frequency. In figure 1, the topmost branch provides the 13.56 MHz signal, the middle branch provides the 27.12 MHz signal, and the lowest branch provides the 40.68 MHz signal. A signal generator provides phase-locked trigger signals at the respective frequency to each generator. By adjusting the relative phases between these trigger signals via the signal generator the phase control is realized. The signal generator also provides a trigger channel that can be used to synchronize external equipment, e.g. an ICCD camera for Phase Resolved Optical Emission Spectroscopy (PROES)[44]. The output signals of all matching branches are combined and directly applied to an electrode located inside the plasma reactor. An electrical filter is installed at the output of each matching network to block signals from other matching branches. In this way parasitic coupling between the matching branches is minimized, ensuring the functionality of the automatic matching. Each matching network is equipped with a band pass filter. Alternatively, the 13.56 MHz matching could have been equipped with a low pass filter and the 40.68 MHz matching network could have been equipped with a high pass filter. In order to facilitate future extensions of the system to more frequencies (lower and higher frequencies) band pass filters were chosen.

Each matching network uses an L-type[2] configuration. While most conventional matching networks employ phase–magnitude–detectors that measure the phase difference and magnitude of the RF current and voltage, we use directional couplers, which are more robust against signal distortion, and are better suited to handle stray, reflected signals from the other matching branches. As a result parallel auto–matching remains functionable when all RF sources are switched on simultaneously.

For the RF generators it is even more important to block signal fractions originating from the other matching branches compared to the matching units. Otherwise frequency conversion products and instabilities could occur. Thus, an additional bandpass filter is placed at the output of each RF generator.

The RF generators are triggered by an external RF signal. Modern RF generators often provide this feature; however, these signals are usually fed to a TTL circuit. As such circuits would cause phase jitter, no TTL circuits were used here. Instead the signal is amplified by linear RF stages where an analog RF attenuator is used as a correcting element for the control loop; thus, the dependence of the phase relationship between the output signal and the input signal on the output power level is minimized.

Ultimately, the phase response between the RF generator's input and the matching network's output for a given frequency is most important. Although the RF generator's phase response is almost constant and independent of the amplitude, the matching network inserts a phase shift that depends on its capacitor settings. The final voltage waveform at the electrode surface is, therefore, determined by measuring the voltage waveform in front of the electrode by a high-voltage probe and applying the calibration procedure described in section II.B[22]. The amplitude and relative phases of each of the applied frequencies are adjusted iteratively to obtain the desired voltage waveform at the electrode surface.

The heart of the system is the signal generator and phase shifter. The signals are generated with a Direct Digital Synthesize (DDS) chip. This integrated circuit provides four synchronized DDS channels with 14 bit phase resolution, very low phase noise, and independent control of frequency, phase, and amplitude. To provide eight channels (for up to 8 consecutive harmonics), two of these integrated circuits must be synchronized using a stable and identical clock signal produced by a dedicated integrated circuit with low phase noise. The signal generator and phase shifter can provide reliable signals up to 200 MHz.

The additional trigger channel provides a trigger signal at $f/1000 = 13.56$ kHz that can be used to synchronize plasma diagnostics such as an ICCD camera for PROES[44] with the driving voltage waveform. Such diagnostics often require a phase-locked trigger at frequencies lower than the applied fundamental RF. Although the output frequency is much lower than the lowest RF frequency, it is still synchronized to the RF signal. While the trigger channel is also based on the DDS chip, the voltage level must be adapted to drive logical circuits that standard equipment, e. g. cameras, require. High Speed circuits are used to avoid phase jitter.

The entire system is controlled by a LabVIEW control panel. It allows the relative phase and amplitude of each harmonic to be set separately and independently. It also allows independent control of the matching networks in each frequency branch.

This novel multi-frequency RF power supply reduces the reflected power from more than 90 % (previous works) to about 5 % of the total applied power. This is an enormous and extremely important improvement, since it allows to transfer the technology of RF voltage waveform tailoring to industrial applications. For such applications 90 % reflected power are unacceptable, but

5 % correspond to typical levels of reflected power found in single frequency CCRF discharges.

B. Plasma Source and Diagnostics

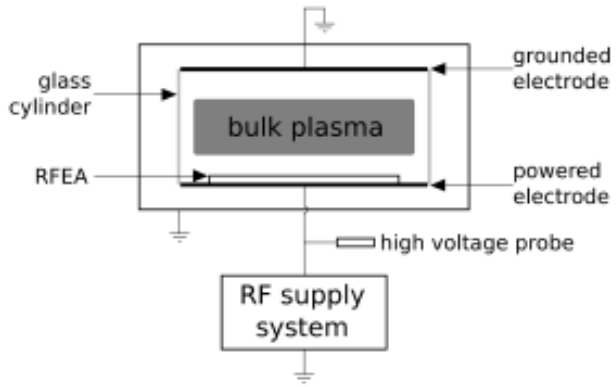

FIG. 2. Sketch of the experimental setup including the capacitively coupled GEC reference cell and the diagnostics (RFEA and high voltage probe). For details of the RF power supply system see figure 1.

The experimental setup including the diagnostics is shown in figure 2. A multi-frequency voltage waveform according to equation (1) is applied to the powered electrode of a modified Gaseous Electronics Conference (GEC) reference cell. Here $N = 3$ consecutive harmonics of $f = 13.56$ MHz, and a total voltage amplitude of $\phi_{tot} = 120$ V are used. The harmonics' amplitudes are chosen according to the following criterion to maximize the electrical control range of the DC self-bias[27]:

$$\phi_k = \phi_{tot} \frac{2(N-k+1)}{N(N+1)} \tag{2}$$

Thus, $\phi_1 = 60$ V, $\phi_2 = 40$ V, and $\phi_3 = 20$ V are used here for the voltage amplitudes of the 13.56 MHz, the 27.12 MHz, and the 40.68 MHz RF signals respectively.

The discharge is operated in argon at 5 Pa within the adjustable gap between two circular, stainless steel electrodes, with a diameter of 10 cm. The gap length, d, has been set to 4 cm by adjusting the height of the top grounded electrode, while the position of the bottom powered electrode is fixed. A glass cylinder radially confines the plasma between the electrodes. Nevertheless, this discharge configuration is geometrically asymmetric due to the capacitive coupling between the glass cylinder and the grounded side wall of the vacuum chamber[22,45,46].

Two diagnostics are utilized to investigate this triple frequency discharge. Firstly, a high voltage probe is attached to the cable connecting the combiner behind the the matching branches with the powered electrode. The amplitudes and phases of the voltage waveforms corresponding to the three applied frequencies at the electrode surface are determined based on a calibration routine, which has been used on dual-frequency systems before[22]: The chamber is vented and the high voltage probe is attached to the powered electrode surface. By comparing the voltage waveform at the measurement position (on the cable) with the voltage waveform at the electrode surface, calibration factors for the amplitudes and phases are determined for each of the individual harmonics. These calibration factors are system dependent and different for each applied frequency. Care has been taken both during the calibration procedure and during the actual measurements that any disturbance due to reflections of the applied power, i.e. due to an improper matching, is minimized.

Secondly, a Retarding Field Energy Analyzer (RFEA, Impedans Semion[47]) is placed on the powered electrode surface. Ions and electrons enter the device through eight orifices facing the plasma. The RFEA basically consists of three grids and a collector plate. The first grid remains on the potential of the housing, i.e. the oscillating potential of the electrode, to prevent any disturbance of the plasma. The second grid is on a potential of about -60 V with respect to the first grid to repel the electrons. The potential of the third grid is varied, thereby varying the minimum kinetic energy of the ions, which are detected at the collector plate. A voltage of about -60 V is applied to this plate to attract all ions that have overcome the potential of the third grid. The first derivative of the ion current onto the plate as a function of the discriminator voltage (of the third grid) yields the ion flux-velocity distribution function, which is conveniently plotted in energy units[48]. Details on the RFEA technique to measure this ion distribution function (ion FEDF) can be found elsewhere[47–50]. The measured ion FEDF, $f(\epsilon_i)$, is further analyzed by calculating the total ion flux, Γ_i, as well as the mean ion energy, $< \epsilon_i >$[22,25,26]:

$$\Gamma_i = \int_0^{\epsilon_{i,max}} f(\epsilon_i) d\epsilon_i, \tag{3}$$

$$< \epsilon_i > = \Gamma_i^{-1} \int_0^{\epsilon_{i,max}} \epsilon_i f(\epsilon_i) d\epsilon_i. \tag{4}$$

Here, $\epsilon_{i,max}$ is the maximum energy of the ions.

C. Model of the Electrical Asymmetry Effect

We compare the measured DC self-bias with the analytical model of the EAE, which has been introduced in Ref. 20 and extensively discussed in Ref. 23. In brief, the electrical circuit of the discharge is modeled by the voltage balance

$$\bar{\phi} + \eta = \phi_{sp} + \phi_b + \phi_{sg}, \tag{5}$$

where $\bar{\phi}$, η, ϕ_{sp}, ϕ_b, and ϕ_{sg}, are the applied voltage waveform, the DC bias self-developed by the plasma, and

the individual voltage drops across the powered electrode sheath, the plasma bulk, and the grounded electrode sheath, respectively. Typically, the bulk voltage, ϕ_b, can be neglected in low pressure electropositive plasmas[23]. Furthermore, it is assumed that both sheaths totally collapse at least once within the fundamental RF period. These collapses occur at the times of maximum, $\bar{\phi}_{max}$, and minimum, $\bar{\phi}_{min}$, applied voltage. Then, examining the voltage balance at these two specific times yields a simple equation for the DC self-bias, η[20,23]:

$$\eta = -\frac{\bar{\phi}_{max} + \varepsilon\bar{\phi}_{min}}{1+\varepsilon}. \tag{6}$$

Hence, the DC self-bias depends on the global extrema of the applied voltage waveform, i.e. it can be controlled by tuning the phases between the applied harmonics, and on the symmetry parameter, ε, which is defined as[20,23]

$$\varepsilon = \left|\frac{\phi_{sg}^{max}}{\phi_{sp}^{max}}\right| \approx \left(\frac{A_p}{A_g}\right)^2 \frac{\bar{n}_{sp}}{\bar{n}_{sg}}. \tag{7}$$

The symmetry parameter relates the maximum voltage drops across the powered and grounded sheath, ϕ_{sp}^{max} and ϕ_{sg}^{max}, to each other. In a good approximation, it can also be expressed as the product of the squared ratio of the powered and grounded electrode surface areas, A_p and A_g, and the ratio of the mean ion densities in the respective sheaths, $\bar{n}_{sp}$ and $\bar{n}_{sg}$. Therefore, ε provides further insights into the discharge asymmetry induced via the EAE. As already performed in Ref. 25, we determine the symmetry parameter in the experiment by rearranging equation (6) for ε and using the measured values of η, $\bar{\phi}_{max}$, and $\bar{\phi}_{min}$.

III. RESULTS

A. Electrical control of the DC self-bias

Figure 3 shows the DC self-bias normalized by the total applied voltage amplitude, ϕ_{tot}, as a function of the phase of the second and third harmonics resulting from experiment and model. In the model, the symmetry parameter $\varepsilon = 0.63$ is taken to be constant for all phase angles and is determined by averaging over ε obtained from the experiment for each combination of θ_2 and θ_3. In this way the model is simplified. In reality, ε varied by up to $\pm$ 40 % around this averaged value as a function of the harmonics' phases. We find good agreement between the experiment and the model of the DC self bias. The overall shape is very similar and resembles the outcome of a previous simulation study on geometrically symmetric triple-frequency discharges[27]. In contrast to these previous simulations, the measured DC self-bias and the model's prediction of the DC self-bias are shifted towards negative values due to the geometric discharge asymmetry that was not accounted for in the simulation[27]. This shift is caused by the deviation of the symmetry parameter from unity (see equation (7)) caused by the capacitive coupling between the glass cylinder and the grounded chamber walls[22,45,46]. Moreover, the control range is slightly smaller in the experiment

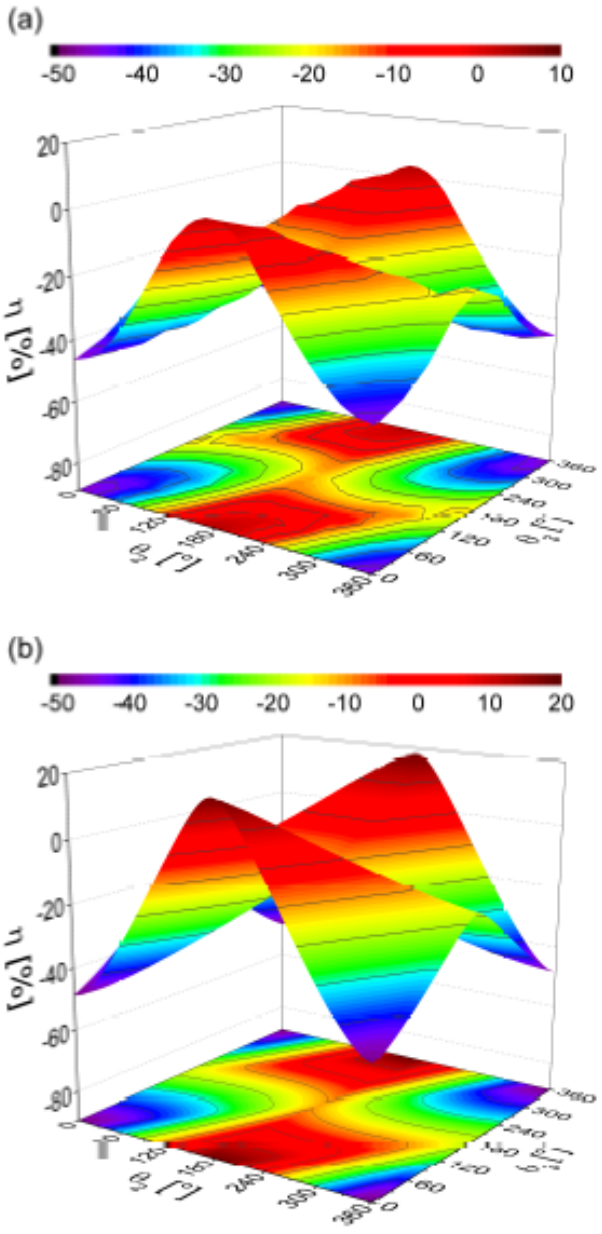

FIG. 3. Normalized DC self-bias as a function of the phases of the second and third harmonic resulting from (a) the experiment and (b) the analytical model. In the model, a symmetry parameter of $\varepsilon = 0.48$ is used. Discharge conditions: Ar, 5 Pa, $d = 4$ cm, $\phi_{tot} = 120$ V, harmonics' amplitudes according to equation (2).

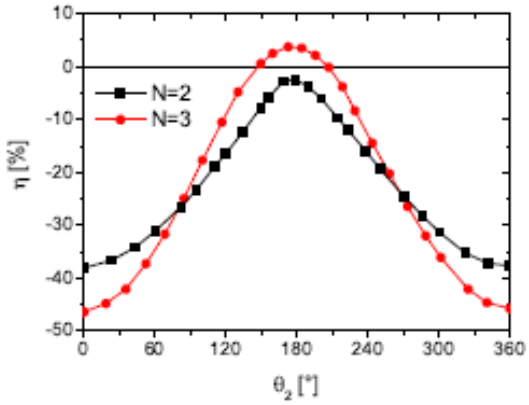

FIG. 4. Normalized DC self-bias as a function of the phase of the second harmonic for two ($N = 2$) and three ($N = 3$) applied consecutive harmonics resulting from the experiment ($\theta_1 = \theta_3 = 0°$). Discharge conditions: Ar, 5 Pa, $d = 4$ cm, $\phi_{tot} = 120$ V, harmonics' amplitudes according to equation (2).

compared to the model assuming a constant symmetry parameter, independent of the phases. This is caused by the fact that the ratio of the mean ion densities in equation (7) and, thus, the symmetry parameter vary as a function of θ_2 and θ_3 in the experiment, but are taken to be constant in the model. In the experiment, we find ε to vary between 0.37 at $\theta_2 \approx 0°$ and $\theta_3 \approx 0°$ and 0.87 at $\theta_2 \approx 0°$ and $\theta_3 \approx 180°$, causing a slight reduction of the total DC self-bias control range[25]. The minimum DC self-bias is found at $\theta_2 \approx 0°$ and $\theta_3 \approx 0°$, while the maximum DC self-bias is found around $\theta_2 \approx 180°$ and $\theta_3 \approx 0°$. There are multiple ways to tune η between these extrema via phase control, but the easiest option is to set $\theta_3 = 0°$ and vary θ_2, i.e. the phase of the second harmonic[27,28]. This is done in the following to control the DC self-bias and the mean ion energy at the electrodes.

A comparison of the DC self-bias in electrically asymmetric dual- and triple-frequency discharges is shown in figure 4 under otherwise identical discharge conditions. In both cases, the control parameter for η is the phase of the second harmonic, θ_2 ($\theta_1 = \theta_3 = 0°$). Again, η is normalized by the total applied voltage amplitude. In a dual-frequency discharge ($N = 2$), the DC self-bias is negative for all phases due to the geometrical asymmetry and the control range is about 35 %, between $\eta \approx -38$ % at $\theta_2 \approx 0°$ and $\eta \approx -3$ % at $\theta_2 \approx 180°$. By adding the third frequency ($N = 3$), it is possible to tune the bias from a minimum of $\eta \approx -46$ % at $\theta_2 \approx 0°$ to a positive value of $\eta \approx 4$ % at $\theta_2 \approx 180°$; thus, the interval over which the DC self-bias can be controlled via the EAE is about 50 %. This means that the electrical control range of η is significantly extended by about 43 % by increasing the number of applied harmonics from $N = 2$ to $N = 3$. This is an important results, since it is the basis for a significantly broader range of ion energy control via the EAE such as described in the next section.

B. Electrical control of the ion energy

Figure 5 shows the ion FEDFs measured at the powered electrode as a function of θ_2 in a dual- and a triple-frequency discharge ($\theta_1 = \theta_3 = 0°$). Under our experimental conditions, the ion mean free path is smaller than the width of the powered electrode sheath; Therefore, the probability of collisions within the sheath is relatively high and, subsequently, the ion FEDFs exhibit a broad shape between $\epsilon_i = 0$ and $\epsilon_i = \epsilon_{i,max}$[25,47–50]. The mean ion energy as well as the shape of the ion FEDF can be controlled by tuning the phase of the second harmonic. At $\theta_2 = 0°$ the DC self-bias is most negative and, accordingly, the time averaged voltage drop across the powered electrode sheath is largest, whereas at $\theta_2 = 180°$ the DC self-bias is maximum and, accordingly, the time averaged voltage drop across the powered electrode sheath is smallest. Therefore, the ion FEDF is relatively broad for $\theta_2 = 0°$ and becomes narrower with increasing θ_2. Meanwhile, for $N = 2$ (figure 5(a)) the maximum ion energy changes from 108 eV to 58 eV. In agreement with the enlarged DC self-bias control interval discussed above, adding the 40.68 MHz component (N = 3, see figure 5(b)) leads to a larger change of the ion FEDF as a function of θ_2 at fixed total voltage amplitude. We find that the maximum possible ion energy is increased to $\epsilon_{i,max} = 118$ eV and the minimum width of the ion FEDF is decreased to $\epsilon_{i,max} = 50$ eV. Furthermore, the total ion flux becomes larger due to the enhanced electron heating in a triple-frequency discharge compared to a dual-frequency discharge[27,28] and the ion flux fraction at relatively high energies becomes larger. This is due to the fact that the sheath width is reduced, as the plasma density increases as a function of N due to the enhanced electron heating dynamics at higher frequencies[27,28,38,39]. Thus, the sheath gets less collisional and more ions hit the electrode at higher energies. This mechanism explains the change of the shape of the ion FEDF. For applications these results mean that the mean ion bombardment energy at the substrate can be controlled over a larger range at higher ion flux (process rate) by adding a third harmonic without increasing the total driving voltage/power. Moreover, the shape of the ion FEDF can be controlled more effectively.

Thus, an advanced customization of the driving voltage waveform results in a significant improvement of the control over the ion properties at the surface. The enhanced control can be quantified in terms of the mean ion energy, $< \epsilon_i >$, and the total ion flux, Γ_i, as shown in figure 6. The mean ion energy can be tuned between about 43 eV (51 eV) and 23 eV (20 eV) by tuning θ_2 from 0° to 180° in a discharge operated at $N = 2$ ($N = 3$) frequencies, respectively. This corresponds to an extension of the $< \epsilon_i >$ control range by more than 50 %. The

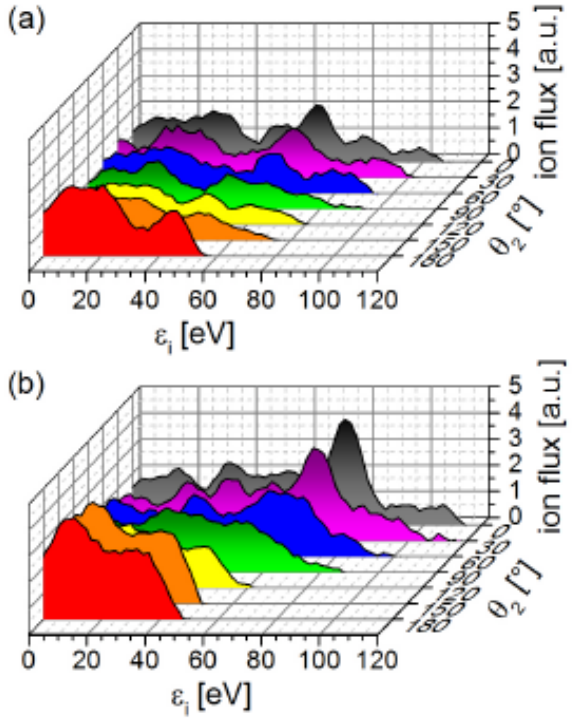

FIG. 5. Ion flux-energy distribution functions measured at the powered electrode as a function of the phase of the second harmonic for (a) two ($N = 2$) and (b) three ($N = 3$) applied frequencies ($\theta_1 = \theta_3 = 0°$). Discharge conditions: Ar, 5 Pa, $d = 4$ cm, $\phi_{tot} = 120$ V, harmonics' amplitudes according to equation (2).

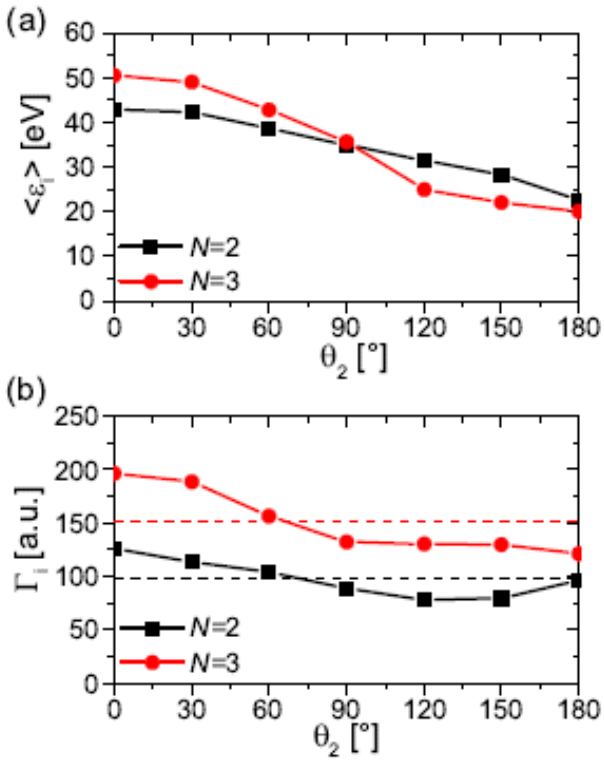

FIG. 6. (a) Mean ion energy, $< \epsilon_i >$, and (b) total ion flux, Γ_i, as a function of θ_2 resulting from the measured ion FEDF in electrically asymmetric dual- and triple-frequency plasmas ($\theta_1 = \theta_3 = 0°$). The dashed lines indicate the ion flux averaged over the measurements at all phases. Discharge conditions: Ar, 5 Pa, $d = 4$ cm, $\phi_{tot} = 120$ V, harmonics' amplitudes according to equation (2).

difference between the mean ion energy for $N = 2$ and $N = 3$ is larger at $\theta_2 = 0°$ than at $\theta_2 = 180°$. This is due to the fact that the sheath is smaller and, therefore, less collisional in the triple-frequency discharge, causing an increase of $< \epsilon_i >$ at all values of θ_2 in the triple- compared to the dual-frequency discharge. In addition to this effect the electrical control range of $< \epsilon_i >$ is enlarged due to the larger control range of η in triple- compared to dual-frequency plasmas. Thus, the enhanced control interval of the DC self-bias and, hence, of the mean sheath voltage as well as the reduced collisionality of the ions inside the sheath due to the smaller sheath width are the mechanisms behind the enhanced ion energy control at a greater number of applied frequencies.

In general, the ion flux is larger for $N = 3$ than for $N = 2$ due to the enhancement of the electron heating dynamics by the added high frequency component (see figure 6(b))[27,28,38]. In both the dual- and the triple-frequency case, the ion flux varies by about ±23 % as a function of the phase. More importantly, there is a tendency of decreasing Γ_i with increasing θ_2. This is due to the following effect: at $\theta_2 = 0°$, the DC self-bias is most negative and, hence, the sheath voltage adjacent to the powered electrode is largest. Thus, at this phase the heating of electrons by their interaction with the electric field of this sheath is maximum (sheath expansion heating in the α-mode[51–65]), leading to a high ionization rate. If θ_2 is increased, the discharge asymmetry is reduced, so that the electron heating and ionization near the powered electrode sheath is reduced. At the same time, the sheath voltage at the grounded electrode increases, only partially compensating the decrease of the electron heating and of the ionization. Thus, the total electron-electron heating, the ionization, and, subsequently, the plasma density and the particle fluxes are smaller for $\theta_2 = 180°$ compared to the $\theta_2 = 0°$ case. A very similar behavior has been observed before in a geometrically and electrically asymmetric discharge[25]. It is important to keep in mind the strongly non-linear dependence of the ionization rate on the electron heating, which itself shows a complex dependence on the sheath dynamics. Based on the findings reported in Ref. 25 and Refs. 22 and 26, this effect on the total ion flux occurs only at the powered electrode of electrically asymmet-

ric discharges, which exhibit an additional geometrical asymmetry due to the electrode configuration, and vanishes for electrically asymmetric but geometrically symmetric discharges. In the latter cases, variations in $\Gamma_i(\theta_2)$ of less than ± 10 % have been achieved experimentally in dual-frequency plasmas as well as in simulations of CCRF plasmas driven by multiple consecutive harmonics.

IV. CONCLUSIONS

A novel RF supply system including impedance matching is presented that allows technological RF plasmas to be driven with customized multi-frequency voltage waveforms and without high reflected powers for the first time. This allows the transfer of this technology from fundamental research to applications on an industrial level and to use its enormous advantages for process control to optimize a variety of applications ranging from plasma etching to PECVD and RF sputtering. These are only a few examples for the diverse potential applications of this multi-frequency supply system. Its commercial availability also fosters further fundamental research in the field of low temperature plasma physics, since it demonstrates that this technology is applicable on industrial levels.

Here, we used the prototype of this novel multi-frequency RF supply system to demonstrate that the Electrical Asymmetry Effect is strongly enhanced by using three instead of two consecutive harmonics of 13.56 MHz in a CCRF plasma. For a given total voltage amplitude and neutral gas pressure we demonstrated that the DC self-bias and the mean ion energy as well as the shape of the ion FEDF at the substrate can be controlled over a much larger range by tuning the harmonics' phases in triple- compared to dual- frequency electrically asymmetric CCRF plasmas operated in argon. The results are in good agreement with model results and previous computational and experimental investigations (performed without impedance matching) of the EAE in multi-frequency capacitive discharges.

The RF supply system can be extended to more than three consecutive harmonics, other fundamental driving frequencies, and higher RF powers depending on the application of interest.

[1] Makabe T and Petrović Z 2006 Plasma Electronics: Applications in Microelectronic Device Fabrication *Taylor & Francis* New York

[2] Lieberman M A and Lichtenberg A J 2005 *Principles of Plasma Discharges and Materials Processing* Wiley, New York (2nd ed.)

[3] Donnelly V M and Kornblit A 2013 Plasma etching: Yesterday, today, and tomorrow *J. Vac. Sci. Technol. A* **31** 050825

[4] Yu L, ODonnell B, Alet P-J, Conesa-Boj S, Peiró F, Arbiol J and Roca i Cabarrocas P 2009 Plasma-enhanced low temperature growth of silicon nanowires and hierarchical structures by using tin and indium catalysts *Nanotechnology* **20** 225604

[5] Rath J 2003 Low temperature polycrystalline silicon: a review on deposition, physical properties and solar cell applications *Solar Energy Mater. Sol. Cells* **76** 431

[6] Hrunski D, Mootz F, Zeuner A, Janssen A, Rost H, Beckmann R, Binder S, Schüngel E, Mohr S, Luggenhölscher D, Czarnetzki U and GraboschG 2013 Deposition of microcrystalline intrinsic silicon by the Electrical Asymmetry Effect technique *Vacuum* **87** 114

[7] Vetterl O, Finger F, Carius R, Hapke P, Houben L, Kluth O, Lambertz A, Mück A, Rech B, Wagner H 2000 Intrinsic microcrystalline silicon: A new material for photovoltaics *Solar Energy Mater. Sol. Cells* **62** 97

[8] Schüngel E, Hofmann R, Mohr S, Schulze J, Röpcke J and Czarnetzki U 2015 Evaluation of the Electrical Asymmetry Effect by spectroscopic measurements of capacitively coupled discharges and silicon thin film depositions *Thin Solid Films* **574** 60

[9] Chu P K, Chen J Y, Wang L P and Huang N 2002 Plasma-surface modification of biomaterials *Materials Science and Engineering R* **36** 143

[10] Gomathi N, Sureshkumar A and Neogi S 2008 RF plasma-treated polymers for biomedical applications *Current Science* **94** 1478

[11] Donkó Z, Schulze J, Czarnetzki U, Derzsi A, Hartmann P, Korolov I and Schüngel E 2012 Fundamental investigations of capacitive radio frequency plasmas: simulations and experiments *Plasma Phys. Cont. Fusion* **54** 124003

[12] Kitajima T, Takeo Y, Petrović Z Lj and Makabe T 2000 Functional separation of biasing and sustaining voltages in two-frequency capacitively coupled plasma *Appl. Phys. Lett.* **77** 489

[13] Georgieva V and Bogaerts A 2006 Plasma characteristics of an Ar/CF4/N2 discharge in an asymmetric dual frequency reactor: numerical investigation by a PIC/MC model *Plasma Sources Sci. Technol.* **15** 368

[14] Lee S H,Tiwari P K and Lee J K 2009 Control of ion energy distribution in low-pressure and triple-frequency capacitive discharge *Plasma Sources Sci. Technol.* **18** 025024

[15] Boyle P C, Ellingboe A R and Turner M M 2004 Electrostatic modelling of dual frequency rf plasma discharges *Plasma Sources Sci. Technol.* **13** 493

[16] Schulze J, Gans T, OConnell D, Czarnetzki U, Ellingboe A R and Turner M M 2007 Space and phase resolved plasma parameters in an industrial dual-frequency capacitively coupled radio-frequency discharge *J. Phys. D: Appl. Phys.* **40** 7008

[17] Waskoenig J and Gans T 2010 Nonlinear frequency coupling in dual radio-frequency driven atmospheric pressure plasmas *Appl. Phys. Lett.* **96** 181501

[18] Gans T, Schulze J, OConnell D, Czarnetzki U, Faulkner R, Ellingboe A R and Turner M M 2006 Frequency coupling in dual frequency capacitively coupled radio-frequency plasmas *Appl. Phys. Lett.* **89** 261502

[19] Donkó Z, Schulze J, Hartmann P, Korolov I, Czarnetzki U and Schüngel E 2010 The effect of secondary electrons on the separate control of ion energy and flux in dual-frequency capacitively coupled radio frequency discharges *Appl. Phys. Lett.* **97** 081501

[20] Heil B G, Czarnetzki U, Brinkmann R P and Mussenbrock T 2008 On the possibility of making a geometrically symmetric RF-CCP discharge electrically asymmetric *J. Phys. D: Appl. Phys.* **41** 165202

[21] Donkó Z, Schulze J, Heil B G and Czarnetzki U 2009 PIC simulations of the separate control of ion flux and energy in CCRF discharges via the electrical asymmetry effect *J. Phys. D: Appl. Phys.* **42** 025205

[22] Schulze J, Schüngel E and Czarnetzki U 2009 The electrical asymmetry effect in capacitively coupled radio frequency discharges measurements of dc self bias, ion energy and ion flux *J. Phys. D: Appl. Phys* **42** 092005

[23] Czarnetzki U, Heil B G, Schulze J, Donkó Z, Mussenbrock T, and Brinkmann R P 2009 The Electrical Asymmetry Effect - A novel and simple method for separate control of ion energy and flux in capacitively coupled RF discharges *J. Phys. Conf. Ser.* **162** 012010

[24] Bienholz S, Styrnoll T and Awakowicz P 2014 On the electrical asymmetry effect in large area multiple frequency capacitively coupled plasmas *J. Phys. D: Appl. Phys.* **47** 065201

[25] Schüngel E, Eremin D, Schulze J, Mussenbrock T and Czarnetzki U 2012 The electrical asymmetry effect in geometrically asym-

metric capacitive radio frequency plasmas *J. Appl. Phys.* **112** 053302
[28]Schüngel E, Mohr S, Schulze J, Czarnetzki U and Kushner M J 2014 Ion distribution functions at the electrodes of capacitively coupled high-pressure hydrogen discharges *Plasma Sources Sci. Technol.* **23** 015001
[27]Schulze J, Schüngel E, Donkó Z and Czarnetzki U 2011 The electrical asymmetry effect in multi-frequency capacitively coupled radio frequency discharges *Plasma Sources Sci. Technol.* **20** 015017
[28]Derzsi A, Korolov I, Schüngel E, Donkó Z and Schulze J 2013 Electron heating and control of ion properties in capacitive discharges driven by customized voltage waveforms *Plasma Sources Sci. Technol.* **22** 065009
[29]Johnson E V, Verbeke T, Vanel J-C and Booth J-P 2010 Nanocrystalline silicon film growth morphology control through RF waveform tailoring *J. Phys. D: Appl. Phys.* **43** 412001
[30]Johnson E V, Delattre P A and Booth J-P 2012 Microcrystalline silicon solar cells deposited using a plasma process excited by tailored voltage waveforms *Appl. Phys. Lett.* **100** 133504
[31]Johnson E V, Pouliquen S, Delattre P A and Booth J-P 2012 Hydrogenated microcrystalline silicon thin films deposited by RF-PECVD under low ion bombardment energy using voltage waveform tailoring *J. Non-Cryst. Solids* **358** 1974
[32]Lafleur T, Delattre P A, Johnson E V and Booth J P 2012 Separate control of the ion flux and ion energy in capacitively coupled radio-frequency discharges using voltage waveform tailoring *Appl. Phys. Lett.* **101** 124104
[33]Diomede P, Economou D J, Lafleur T, Booth J P and Longo S 2014 Radio-frequency capacitively coupled plasmas in hydrogen excited by tailored voltage waveforms: comparison of simulations with experiments *Plasma Sources Sci. Technol.* **23** 065049
[34]Lafleur T and Booth J P 2012 Control of the ion flux and ion energy in CCP discharges using non-sinusoidal voltage waveforms *J. Phys. D: Appl. Phys.* **45** 395203
[35]Bruneau B, Novikova T, Lafleur T, Booth J P and Johnson E V 2014 Ion flux asymmetry in radiofrequency capacitively-coupled plasmas excited by sawtooth-like waveforms *Plasma Sources Sci. Technol.* **23** 065010
[36]Bruneau B, Novikova T, Lafleur T, Booth J P and Johnson E V 2015 Control and optimization of the slope asymmetry effect in Tailored Voltage Waveforms for Capacitively Coupled Plasmas *Plasma Sources Sci. Technol.* **24** 015021
[37]Schüngel E, Mohr S, Schulze J and Czarnetzki U 2015 Prevention of ion flux lateral inhomogeneities in large area capacitive radio frequency plasmas via the electrical asymmetry effect *Appl. Phys. Lett.* **106** 054108
[38]Lafleur T, Boswell R W and Booth J P 2012 Enhanced sheath heating in capacitively coupled discharges due to non-sinusoidal voltage waveforms *Appl. Phys. Lett.* **100** 194101
[39]Delattre P A, Lafleur T, Johnson E and Booth J-P 2013 Radio-frequency capacitively coupled plasmas excited by tailored voltage waveforms: comparison of experiment and particle-in-cell simulations *J. Phys. D: Appl. Phys.* **46** 235201
[40]Patterson M M, Chu H Y, and Wendt A E 2007 Arbitrary substrate voltage wave forms for manipulating energy distribution of bombarding ions during plasma processing *Plasma Sourc. Sci. Technol.* **16** 257
[41]Wang S B and Wendt A E 2000 Control of ion energy distribution at substrates during plasma processing *J. Appl. Phys.* **88** 643
[42]Baloniak T, Reuter R and von Keudell A 2010 Fundamental aspects of substrate biasing: ion velocity distributions and nonlinear effects *J. Phys. D* **43** 335201
[43]http://www.barthel-hf.de
[44]Schulze J, Schuengel E, Donko Z, Luggenhoelscher D, and Czarnetzki U 2010 Phase resolved optical emission spectroscopy: a non-intrusive diagnostic to study electron dynamics in capacitive radio frequency discharges *J. Phys. D* **43** 124016
[45]Coburn J W and Kay E 1972 *J. Appl. Phys.* **43** 4965
[46]Lieberman M A and Savas S E 1990 *J. Vac. Sci. Technol. A* **8** 1632
[47]Gahan D, Dolinaj B and Hopkins M B 2008 *Rev. Sci. Instrum.* **79** 033502
[48]Ingram S G and Braithwaite N St J 1988 *J. Phys. D: Appl. Phys.* **21** 1496
[49]Böhm C and Perrin J 1993 *Rev. Sci. Instrum.* **64** 31
[50]Baloniak T, Reuter R, Flötgen C, von Keudell A 2010 Calibration of a miniaturized retarding field analyzer for low-temperature plasmas: geometrical trans- parency and collisional effects *J. Phys. D: Appl. Phys.* **43** 055203
[51]Belenguer Ph and Boeuf J P 1990 Transition between different regimes of rf glow discharges *Phys. Rev. A* **41** 4447
[52]Lieberman M A and Godyak V A 1998 From Fermi acceleration to collisionless discharge heating *IEEE Trans. Plasma Sci.* **26** 955
[53]Surendra M and Graves D B 1991 Electron acoustic waves in capacitively coupled, low-pressure rf glow discharges *Phys. Rev. Lett.* **66** 1469
[54]Gozadinos G, Turner M M and Vender D 2001 Collisionless Electron Heating by Capacitive rf Sheaths *Phys. Rev. Lett.* **87** 135004
[55]Vender D and Boswell R W 1990 Numerical modeling of low-pressure RF plasmas *IEEE Trans. Plasma Sci.* **18** 725
[56]Schulze J, Donkó Z, Luggenhölscher D, Czarnetzki U 2009 Different modes of electron heating in dual-frequency capacitively coupled radio frequency discharges *Plasma Sources Sci. Technol.* **18** 034011
[57]Schulze J, Heil B G, Luggenhölscher D, Brinkmann R P and Czarnetzki U 2008 Stochastic heating in asymmetric capacitively coupled RF discharges *J. Phys. D: Appl. Phys.* **41** 195212
[58]Dittmann K, Matyash K, Nemschokmichal S, Meichsner J and Schneider R 2010 Excitation Mechanisms and Sheath Dynamics in Capacitively Coupled Radio-Frequency Oxygen Plasmas *Contrib. Plasma Phys.* **50** 942
[59]Küllig C, Dittmann K, Wegner T, Sheykin I, Matyash K, Loffhagen D, Schneider R and Meichsner J 2012 Dynamics and Electronegativity of Oxygen RF Plasmas *Contrib. Plasma Phys.* **52** 836
[60]Gans T, O'Connell D, Schulz-von der Gathen V and Waskoenig J 2010 The challenge of revealing and tailoring the dynamics of radio-frequency plasmas *Plasma Sources Sci. Technol.* **19** 034010
[61]Mahony C M O, Wazzan R Al and Graham W G 1997 Sheath dynamics observed in a 13.56 MHz-driven plasma *Appl. Phys. Lett.* **71** 608
[62]Boeuf J P and Belenguer Ph 1992 Transition from a capacitive to a resistive regime in a silane radio frequency discharge and its possible relation to powder formation *J. Appl. Phys.* **71** 4751
[63]Schulze J, Derzsi A, Dittmann K, Hemke T, Meichsner J and Donkó Z 2011 Ionization by Drift and Ambipolar Electric Fields in Electronegative Capacitive Radio Frequency Plasmas *Phys. Rev. Lett.* **107** 275001
[64]Schulze J, Schüngel E, Derzsi A, Korolov I, Mussenbrock T, Donkó Z 2014 Complex Electron Heating in Capacitive Multi-Frequency Plasmas *IEEE Trans. on Plasma Sci.* **42** 2780
[65]Schulze J, Donkó Z, Derzsi A, Korolov I and Schüngel E 2015 The effect of ambipolar electric fields on the electron heating in capacitive RF plasmas *Plasma Sources Sci. Technol.* **24** 015019

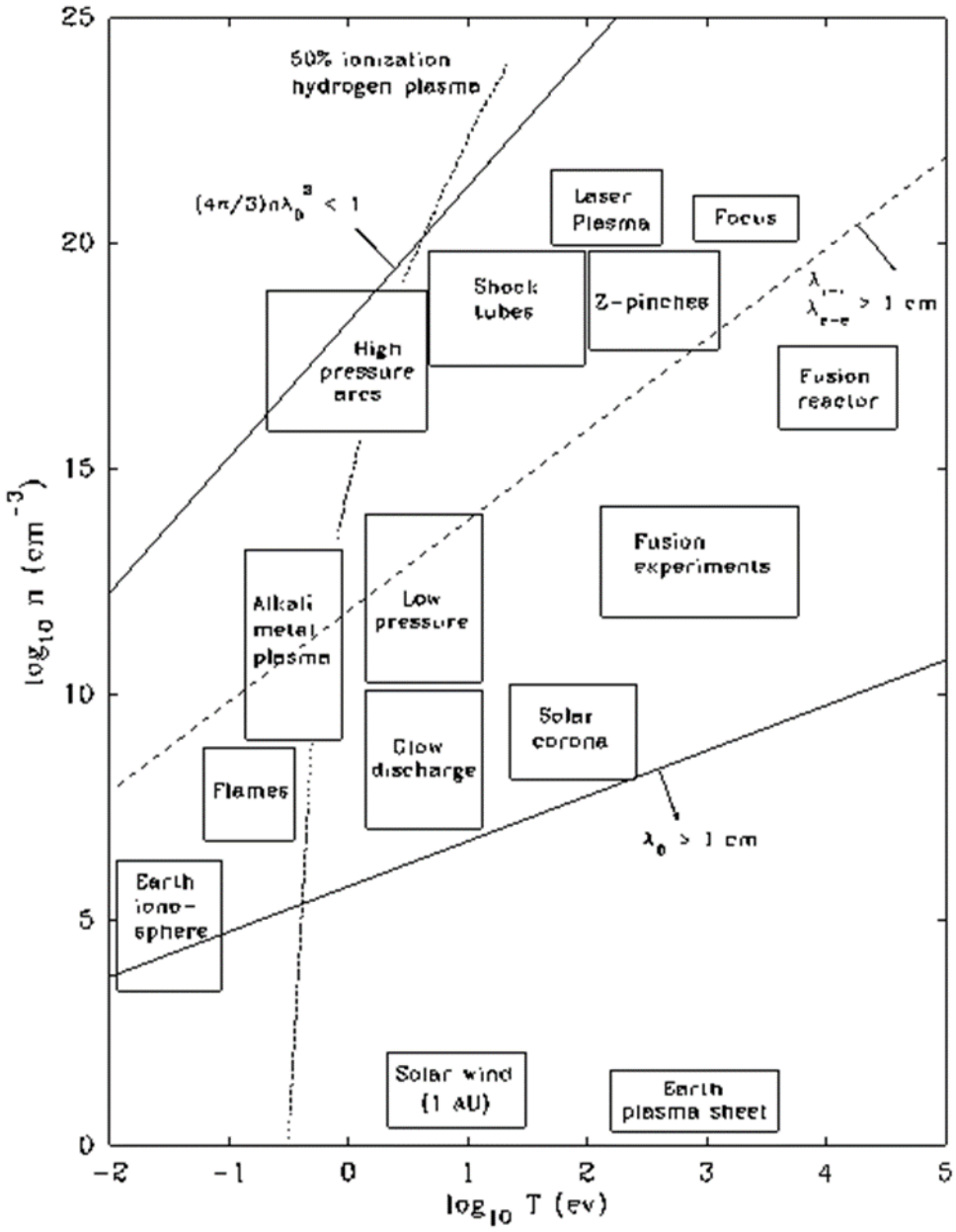

Figure 1.1 This chart provides specific examples of plasmas across a broad range of density and temperature. (reprinted from NRL's plasma formulary, 2013)

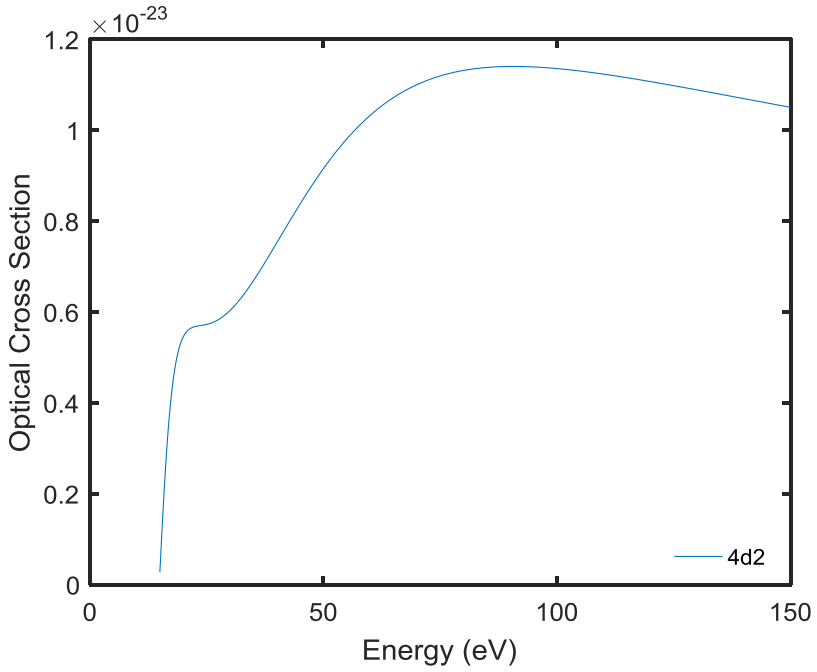

Figure 2.1 Dipole allowed, spin-allowed excitation cross-sections (exemplified by the $4d_2$ state here) have broad cross-section profiles in energy space peaked at several times their onset energy. The small 'peak' near 20eV is due to electron-exchange collisions. Data taken from [*Boffard et al.,* 2004, 2007].

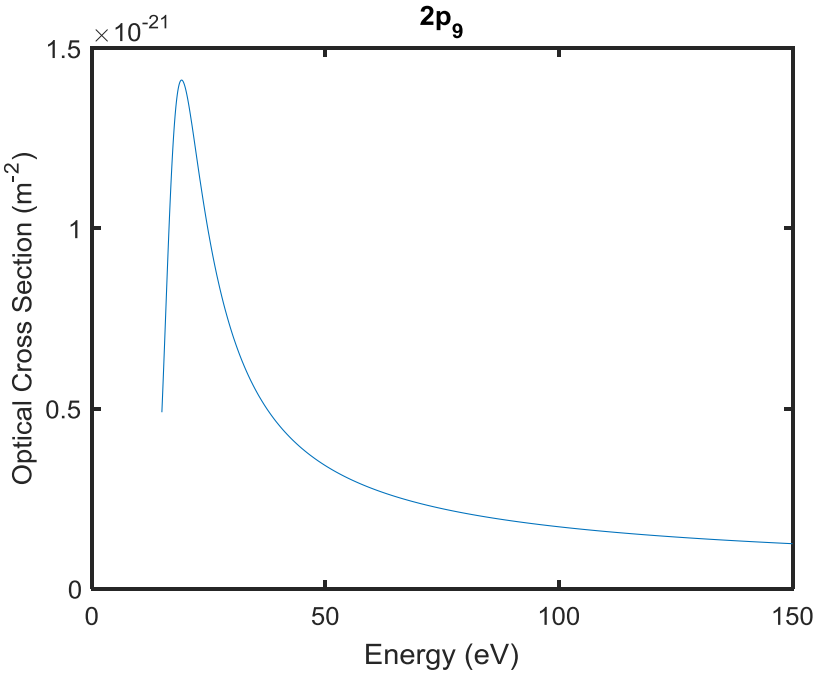

Figure 2.2 Dipole-forbidden, spin-forbidden excitation cross-sections (exemplified by the $2p_9$ state here) very sharply peaked cross-sections in energy space peaked near their onset energy ~20eV. Higher-energy contributions from dipole-allowed transitions or radiative cascades are not present in this cross section. Data taken from [*Boffard et al.,* 2004, 2007].

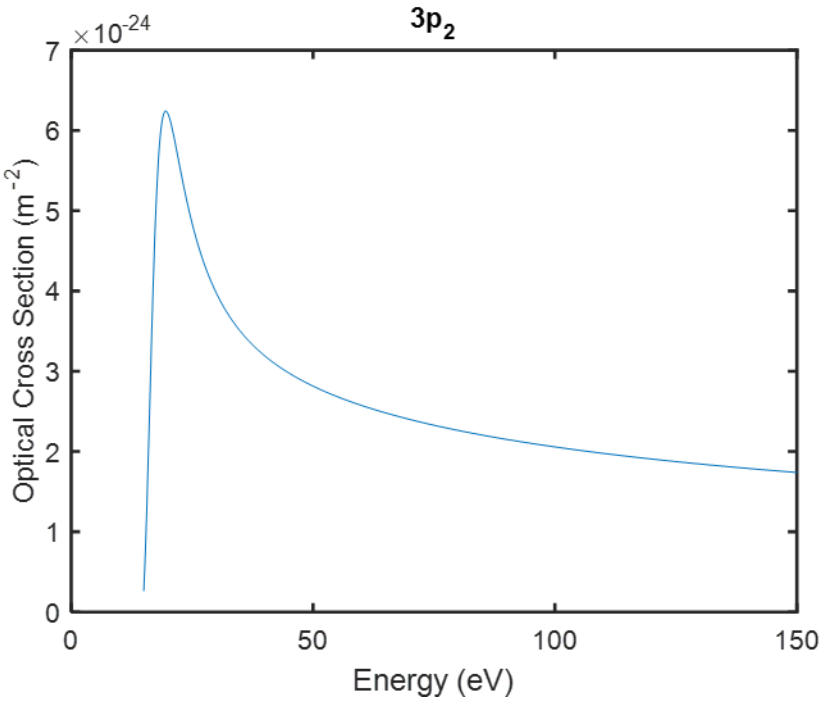

Figure 2.3 Dipole-forbidden, spin-allowed excitation cross-section profiles (exemplified here by the $3p_2$ level) have a sharp peak near 20eV due to electron-exchange collisions and fall off greatly at higher energies. The contribution to the cross-section profile at higher energies (E>50eV) is due to the composite nature of the $3p_2$ wavefunction or due to radiative cascades. Data taken from [*Boffard et al.,* 2004, 2007].

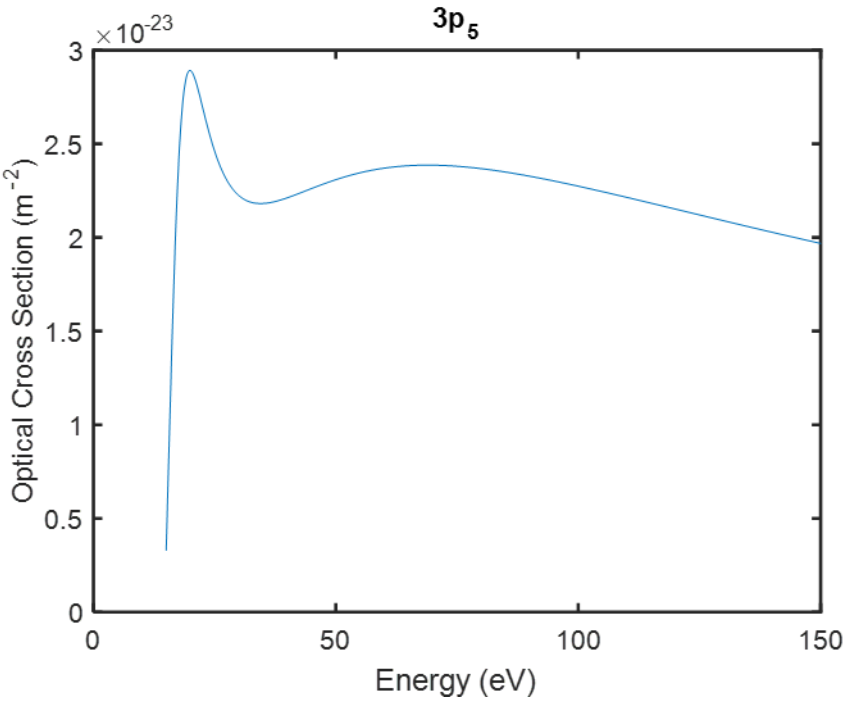

Figure 2.4 Dipole-forbidden, spin-forbidden excitation cross sections may gain a high-energy component due to radiative cascades, which will comprise a substantial part of the overall cross section. Data taken from [*Boffard et al.,* 2004, 2007].

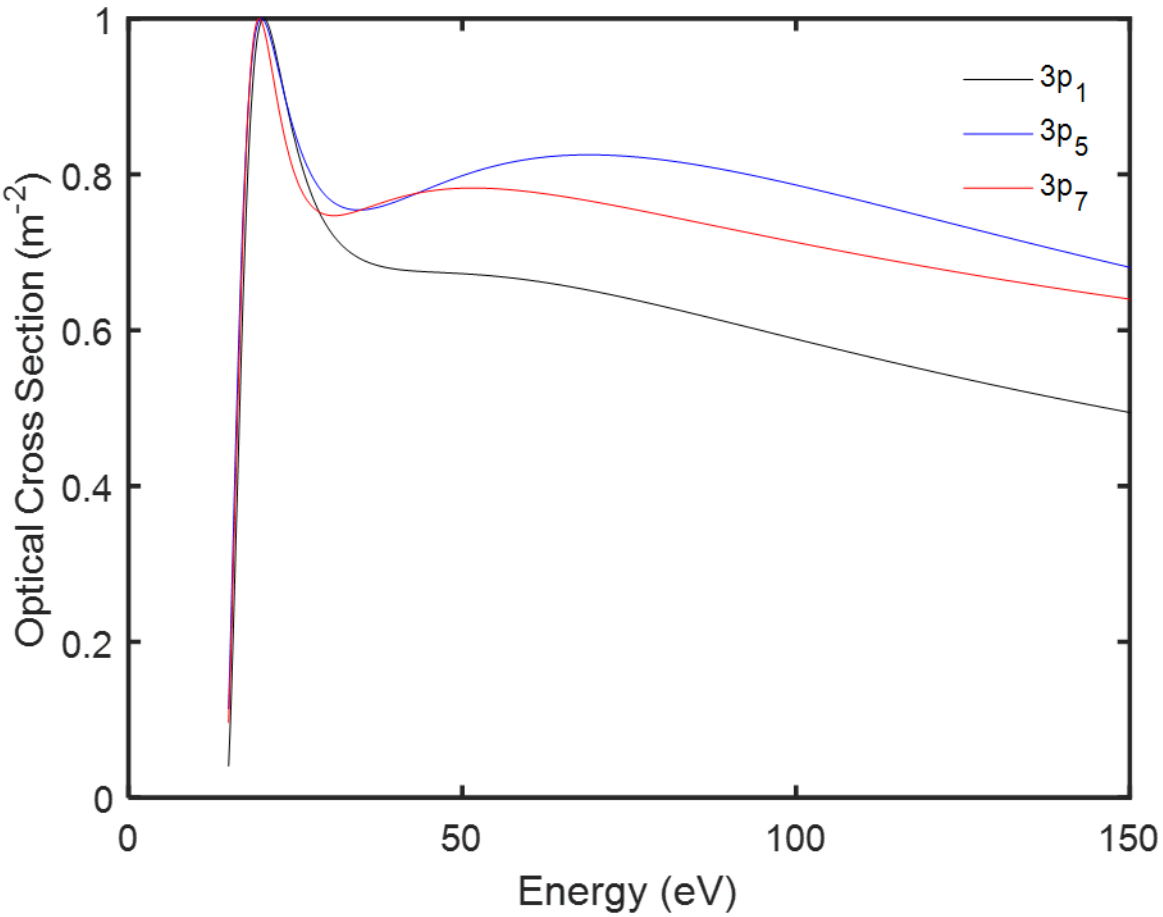

Figure 2.5 Optical Emission cross sections for the ten levels of the 3px manifold are shown. Each cross section is normalized by its peak value. The 3p5 state has the largest (normalized) cascade contribution while the 3p1 state has the smallest. Data taken from [*Boffard et al.,* 2004, 2007].

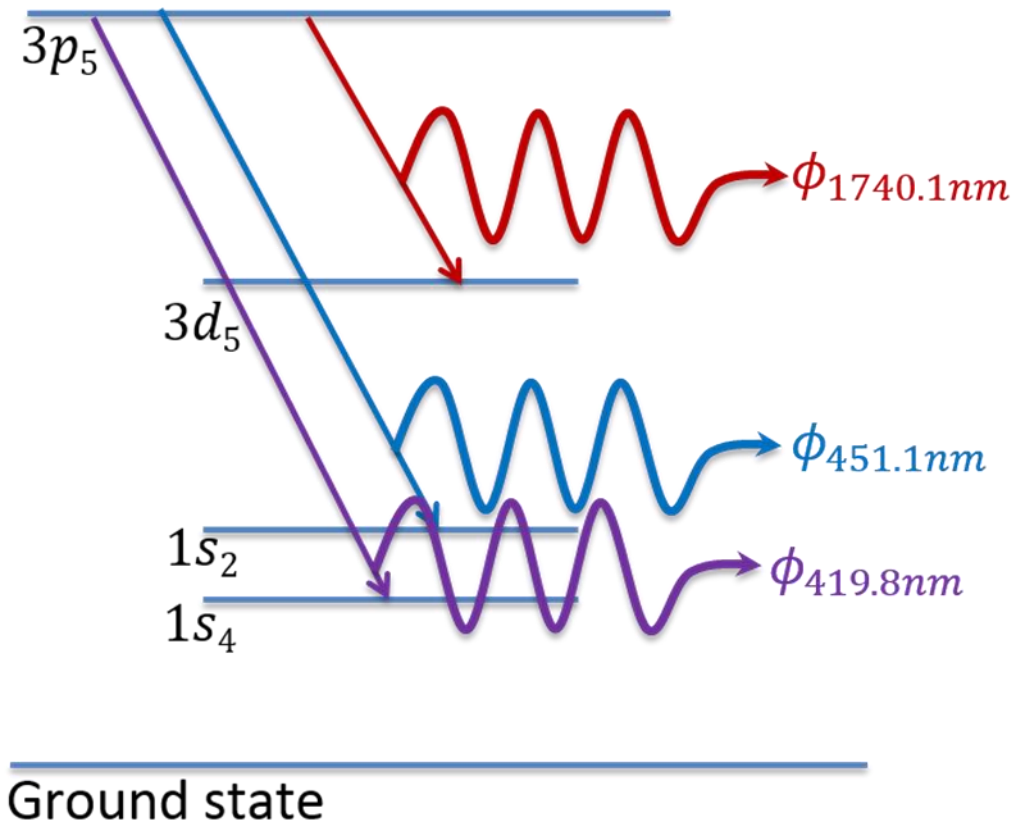

Figure 3.1 Atoms in excited state $3p_5$ may decay into several lower states $1s_4$, $1s_2$, and $3d_5$, producing photon flux at 419.8nm, 451.1nm and 1740.1nm respectively. The likelihood of each relaxation pathway may be determined by equation (3.3). Each of the relaxation pathways produce photons at different wavelengths, thus, accounting for the branching ratio allows for one observed photon flux to describe the upper state *i*. The resulting photon fluxes are distinguishable, therefore, limiting observations to one photon flux may simplify equation (3.1).

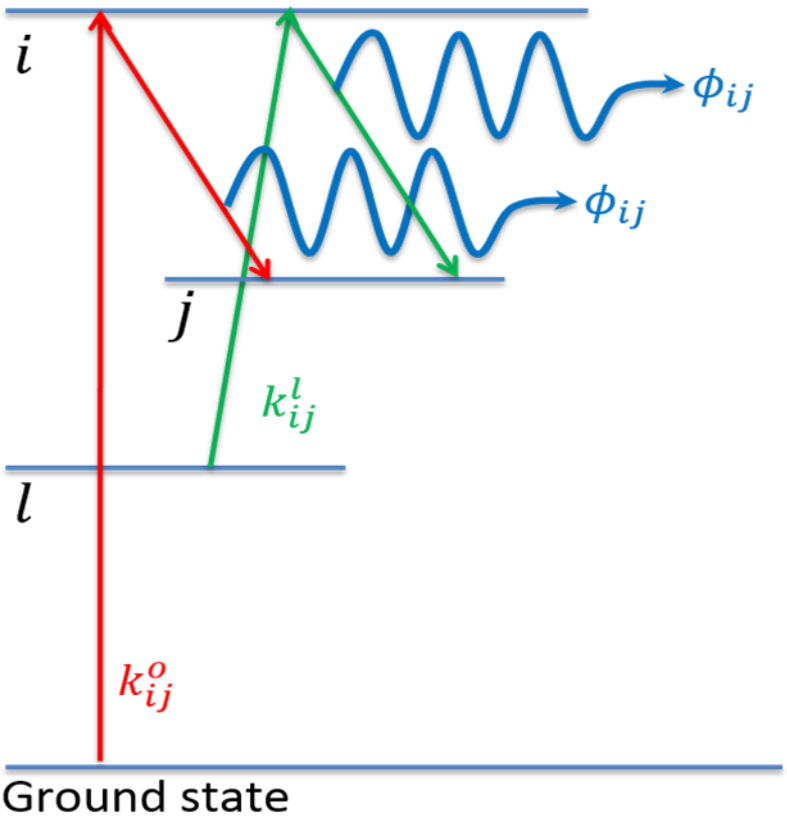

Figure 3.2 Direct electron-collision-induced excitation of an argon atom from the ground state into excited state *i*, and subsequent decay into state *j*, results in photon flux ϕ_{ij}. This process occurs at the rate k_{ij}^{o} and is depicted in red. Stepwise electron-collision-induced excitation of an argon atom from an intermediate state *l* into excited state *i*, and subsequent decay into state *j*, results in photon flux ϕ_{ij}. This process occurs at the rate k_{ij}^{l} and is depicted in green. The photon flux ϕ_{ij} (blue) generated by these pathways are indistinguishable, therefore, both excitation mechanisms must be accounted for in the modeling of the system.

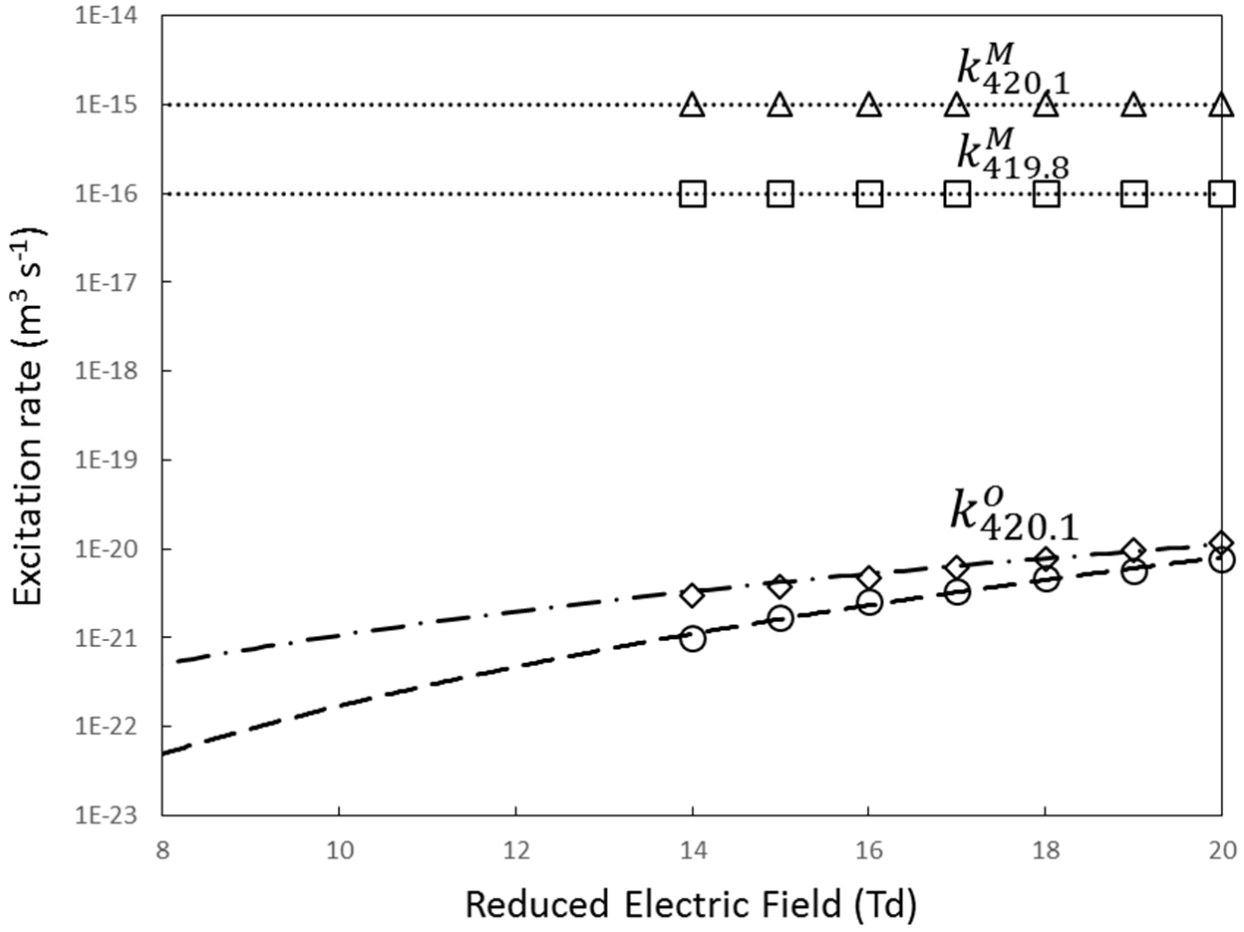

Figure 3.3 Stepwise, $k^M_{420.1}$ (triangle), and direct, $k^o_{420.1}$, excitation rates leading to 420.1nm emission. The bounds of the direct excitation rate are shown for the range of electron density explored here (10^{-5} cm^{-3} diamond, 10^{-6} cm^{-3} circle). Note that $k^o_{419.8} \approx k^o_{420.1}$ in the range presented here. Data points are taken from [*Adams et al.,* 2012].

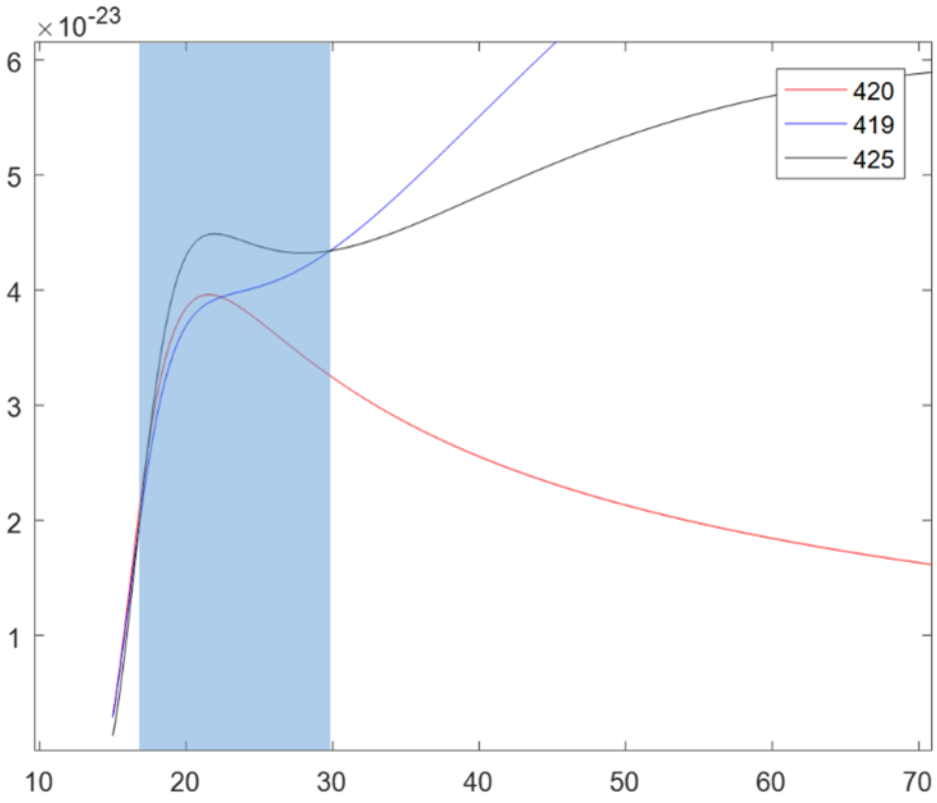

Figure 3.4 Optical emission cross-sections for direct excitation of the 420.1, 419.8, and 425.9nm emission-lines at 1-Torr are shown here. The cross-section for the 425.9nm emission-line is greatest for incident electron energy 15eV<E<30eV. Analytical forms of the cross-sections are taken from [*Boffard et al.,* 2007].

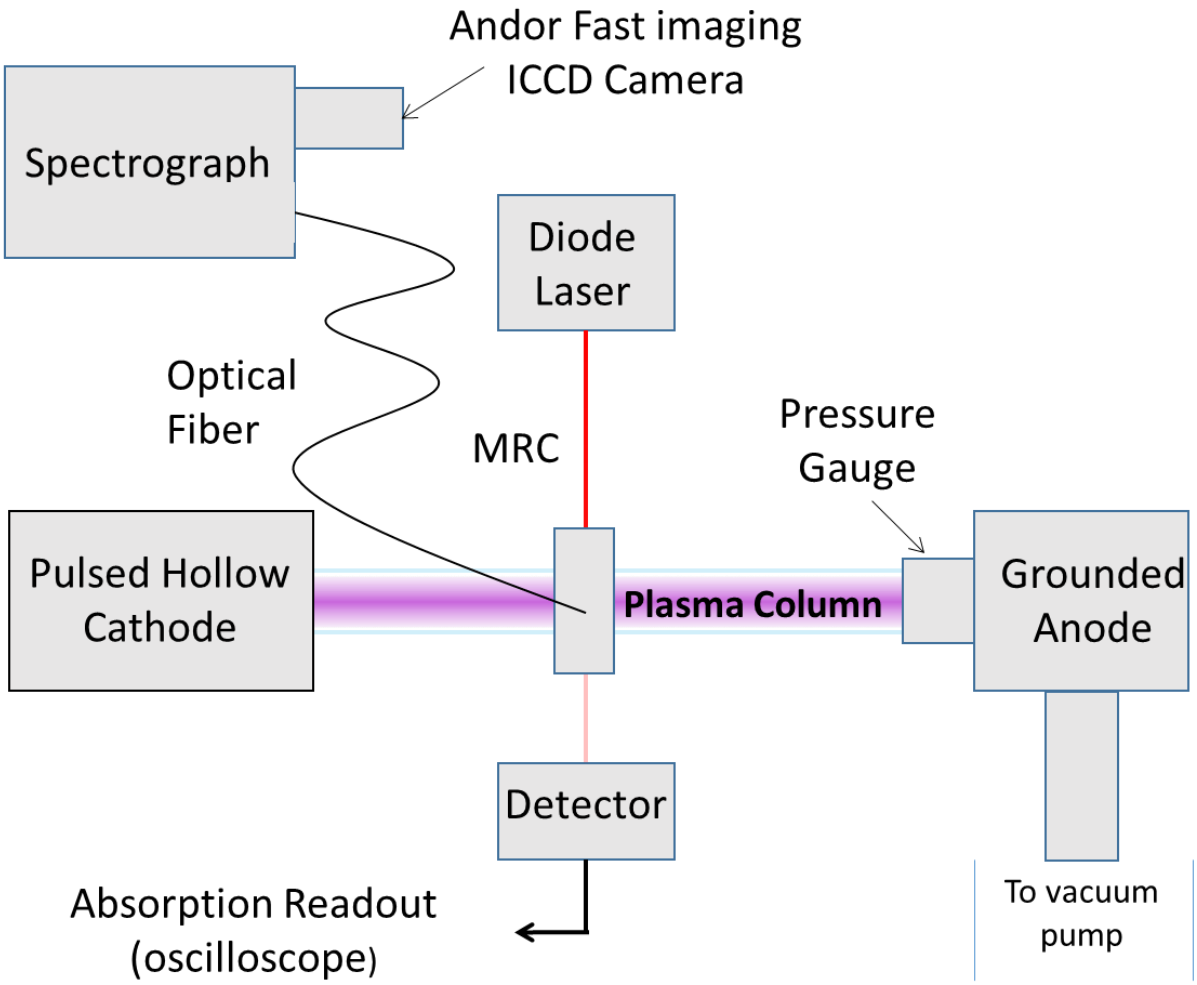

Figure 4.1 The hollow cathode is pulsed at 500Hz to create the positive column studied here. The Microwave Resonant Cavity has optical ports which allow TDLAS and OES measurements to be taken at the same axial position.

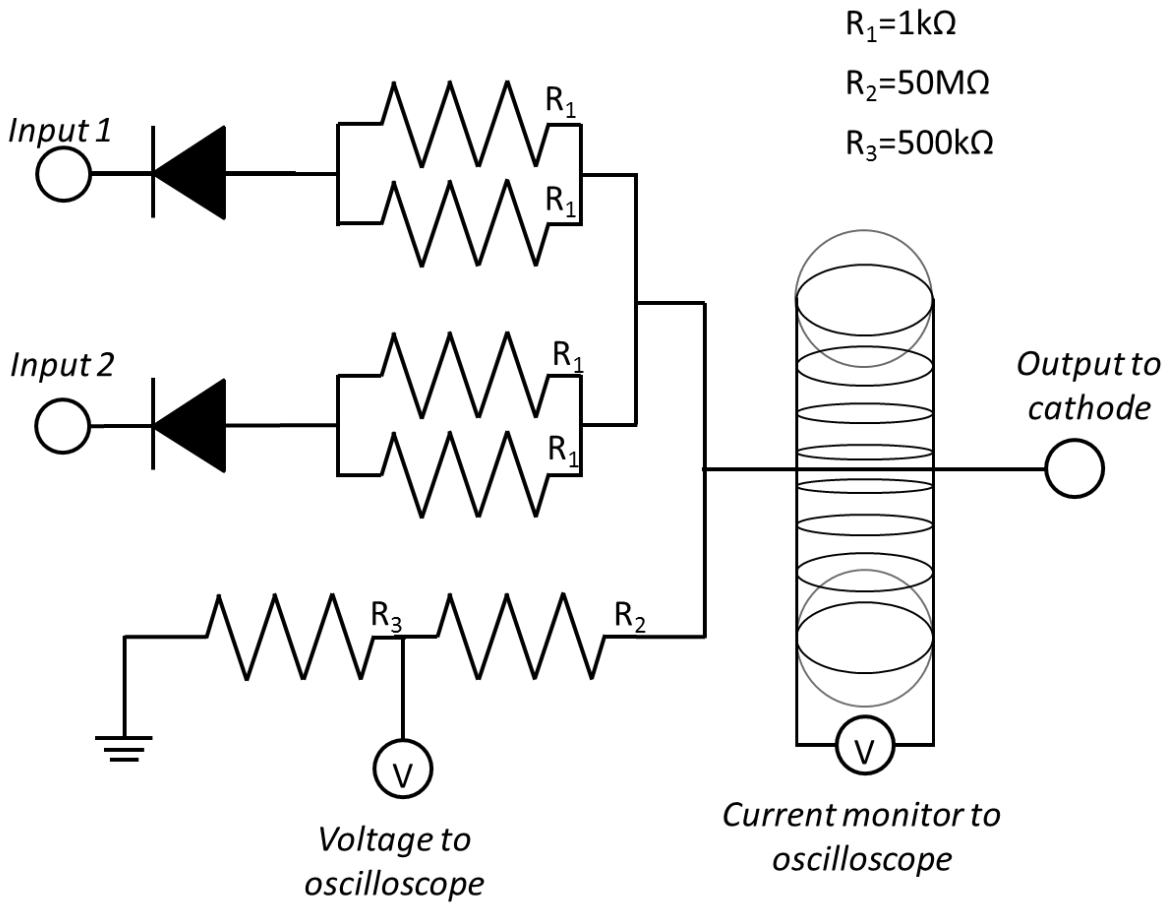

Figure 4.2 Incoming voltage waveforms are conditioned by a committed diode and resistor pair before being combined. A Pearson current monitor and voltage divider are used to produce suitable voltages to the oscilloscope for monitoring.

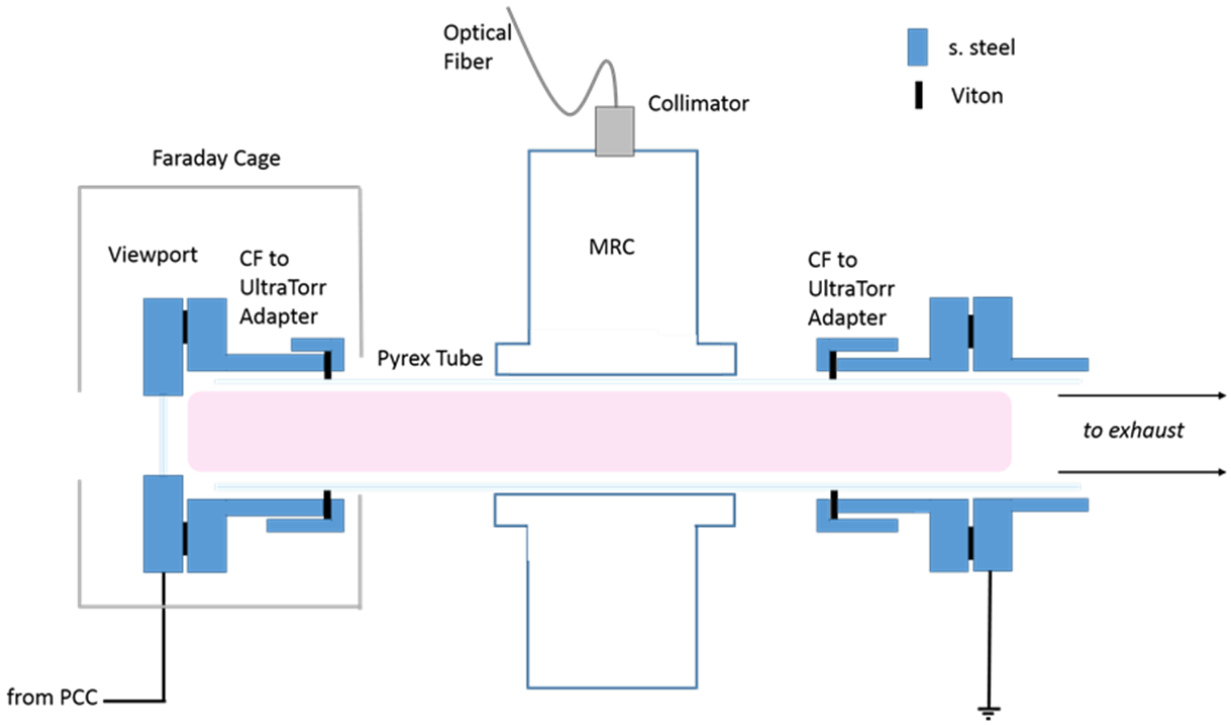

Figure 4.3 A detailed view of the experimental setup surrounding the plasma area of interest is shown here. The viewport flange is biased (from PCC) and a plasma (pink) is struck between the viewport and the grounded anode.

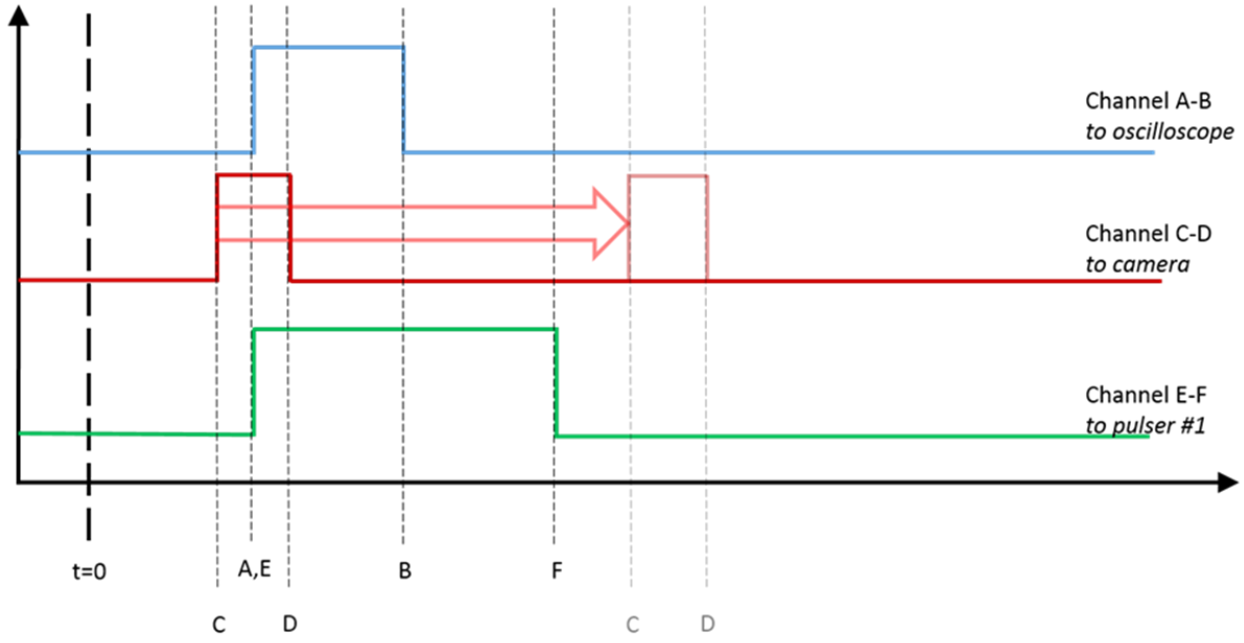

Figure 4.4 Output waveforms from channels A-B, C-D, and E-F for the single-pulse experiments are shown here. Channel A-B is referenced to a specific delay time with respect to the DDG's internal clock at time t=0, and time-point E is always synchronized with time-point A. Time-point F is held at 20μs after time-point E to ensure the plasma-creating pulse is 20μs long. Channel C-D, which triggers the camera, starts 400ns before the plasma-generating pulse (Channel E-F) and advances to capture plasma-emission spectra of the entire pulse duration. The last camera image (Channel C-D, faded) is taken in the afterglow of the plasma generated by Channel E-F.

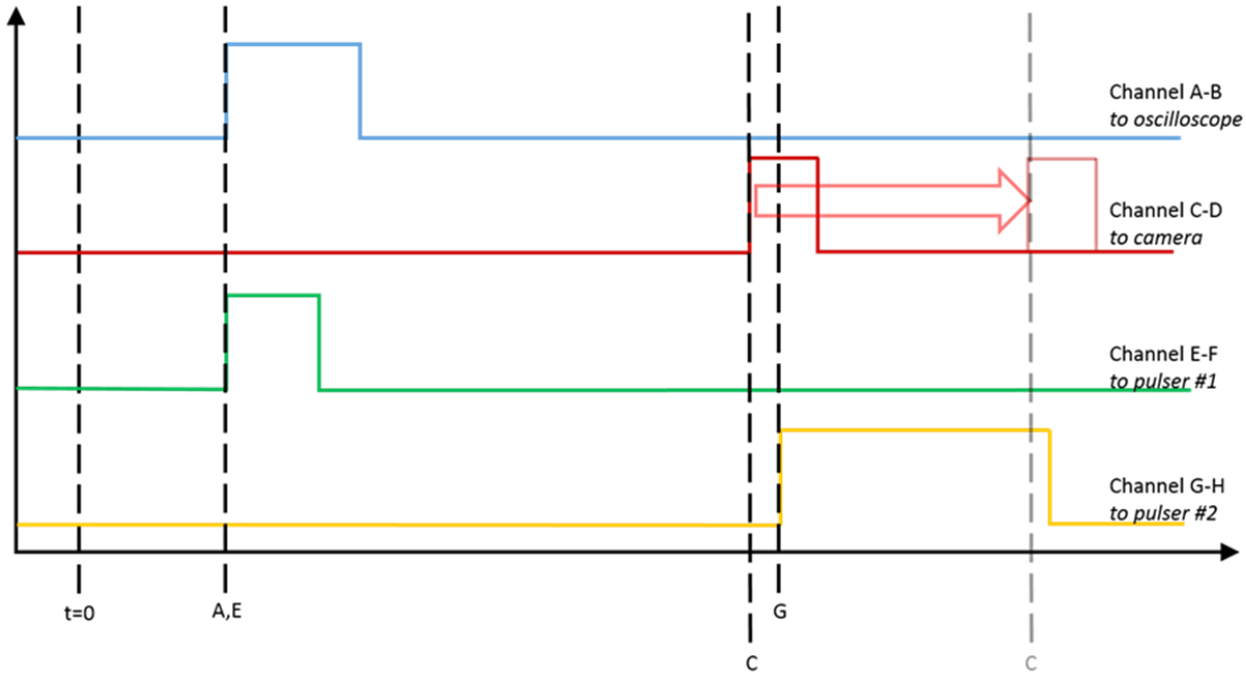

Figure 4.5 Output waveforms from channels A-B, C-D, E-F, and G-H for the double-pulse experiments are shown here. Channel C-D is incremented by 200ns throughout the experiment to compile time-resolved spectra of the plasma-conditioning pulse (Channel G-H).

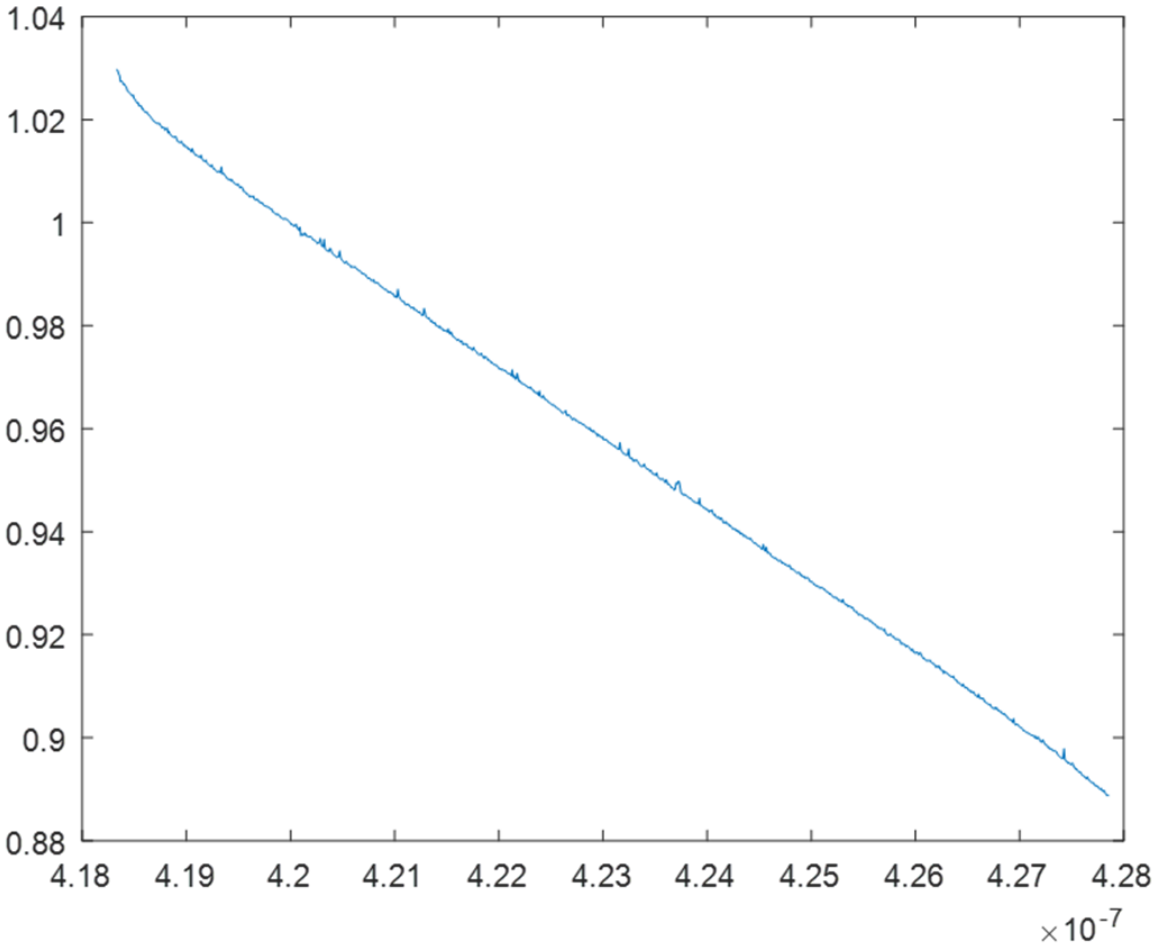

Figure 4.6 The observed transmittance curve used for relative calibration of the spectroscopic system is shown here. The curve is normalized such that the calibration factor for 420.1nm emission is unity.

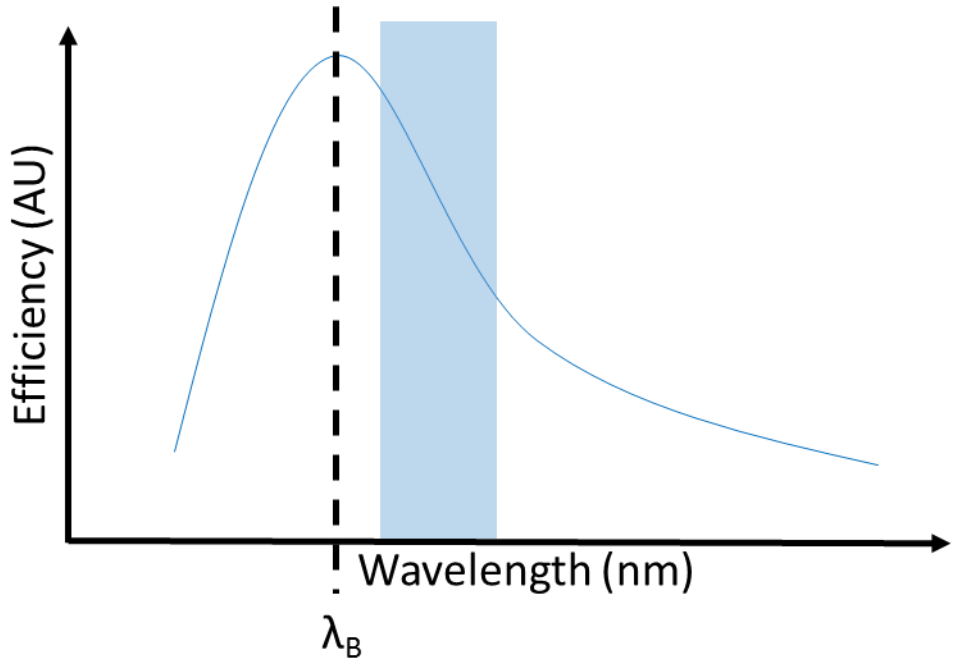

Figure 4.7 The expected transmittance function of a diffraction grating is shown here. The peak efficiency of a diffraction grating is at the blaze wavelength, λ_B = 400nm for the 2400grooves/mm diffraction grating primarily used in this work. The blue shaded area represents the approximate wavelength range imaged by the spectrograph.

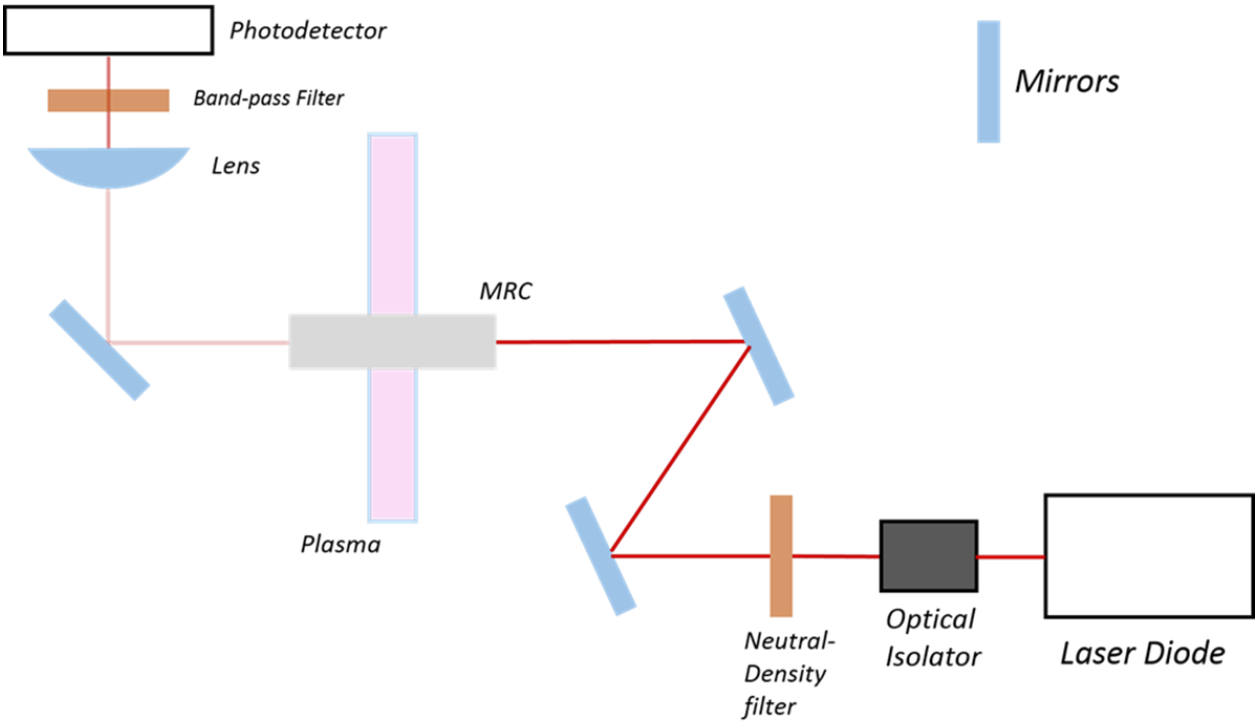

Figure 4.8 Laser light from the laser diode is guided through the body of the microwave resonant cavity. The percentage of absorbed light is proportional to the density of a specific argon excited state in the plasma.

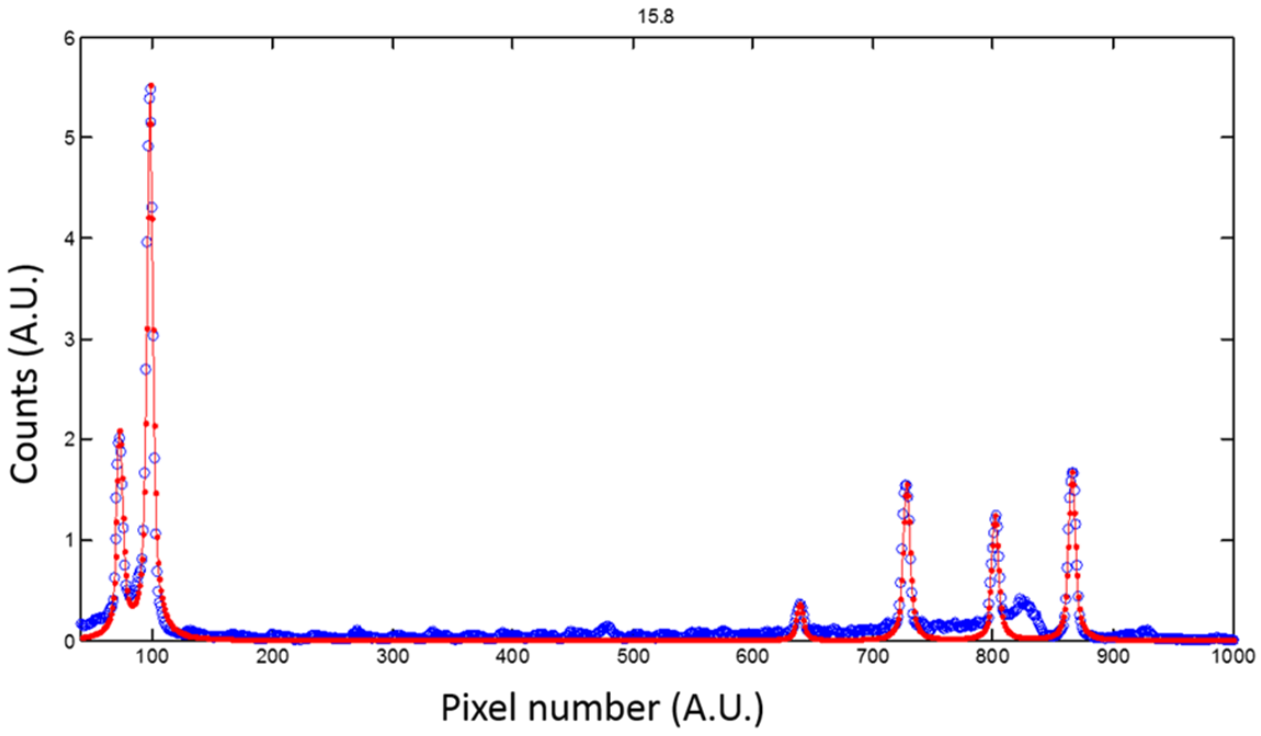

Figure 5.1 Expected argon emission-lines (red) have peaks at 419.83, 420.06, 425.12, 425.93, 426.63 and 427.22nm. Observed plasma spectra (blue) is also shown here. The observed signal peak near pixel #825 (λ~426.9nm) indicates a nitrogen impurity.

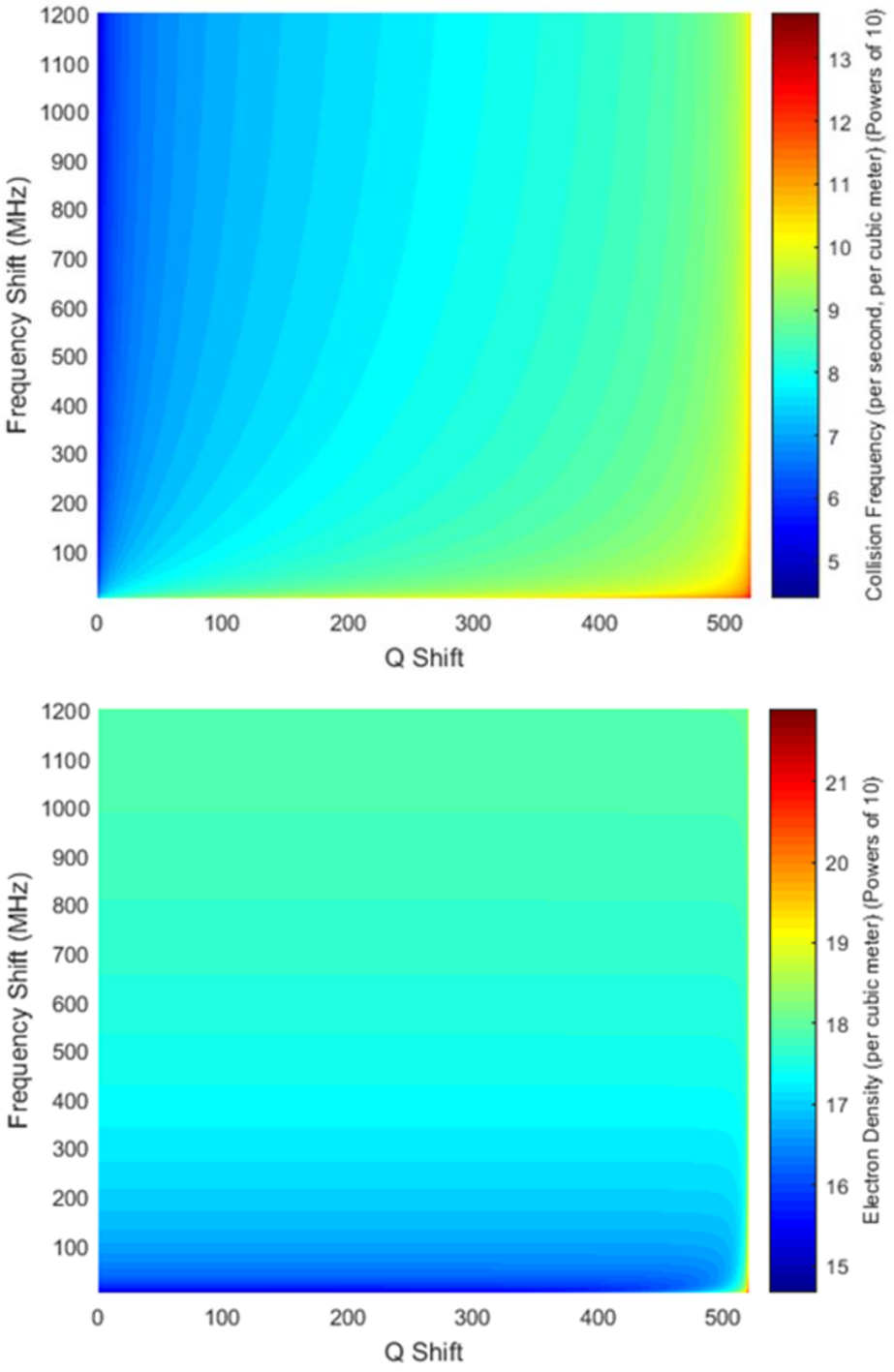

Figure 5.2 Look-up tables produced by equations (eta) and (gamma) produce, in turn, look-up tables for electron density and collision frequency respectively. The observed resonant-peak frequency shift is dominant in determining electron density while Q shift is the dominant factor in determining collision frequency. Observed frequency shift provides a small correction in determining collision frequency.

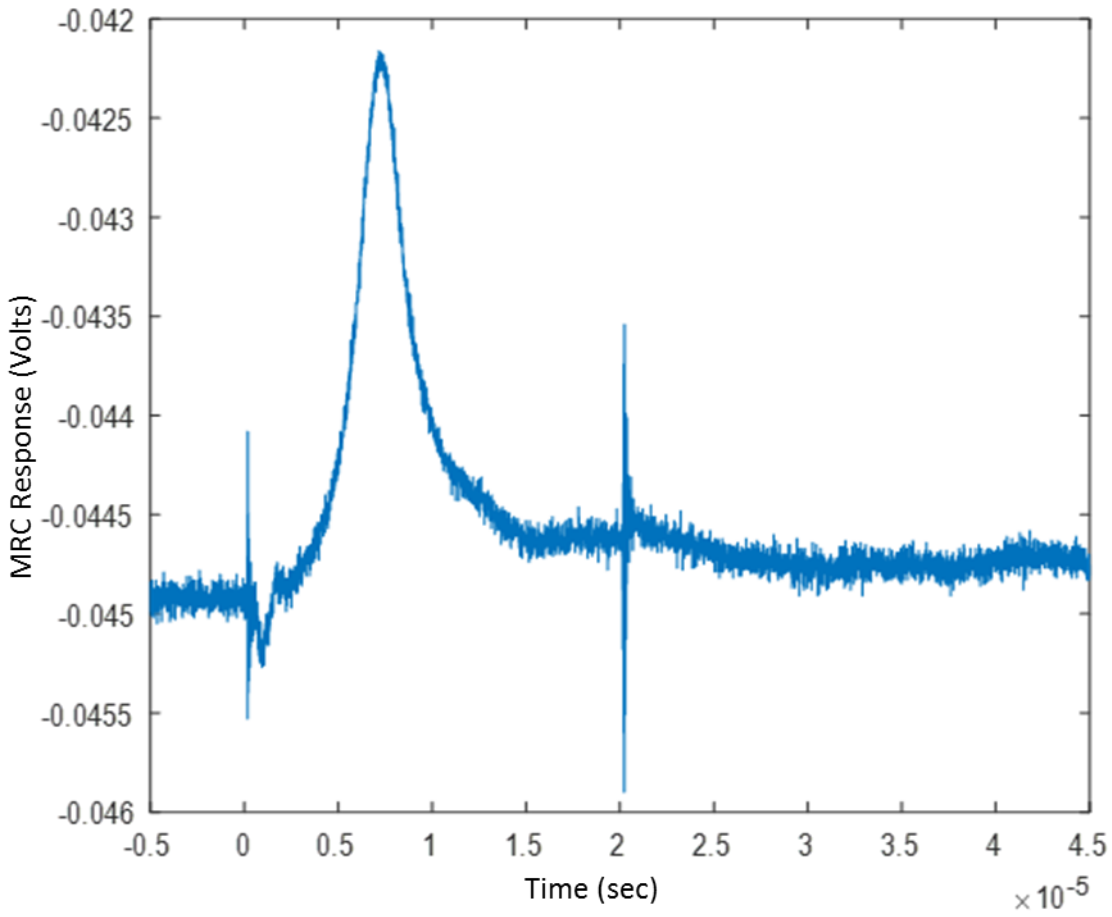

Figure 5.3 The microwave cavity's response to an applied microwave frequency is shown here. Reflected power is shown as a negative voltage. The 'peak' is actually a decreased signal in reflected power and represents increased cavity resonance for the particular frequency. Data from a range of applied frequencies is compiled to create figure 5.4. This figure represents one horizontal line of data shown in figure 5.4.

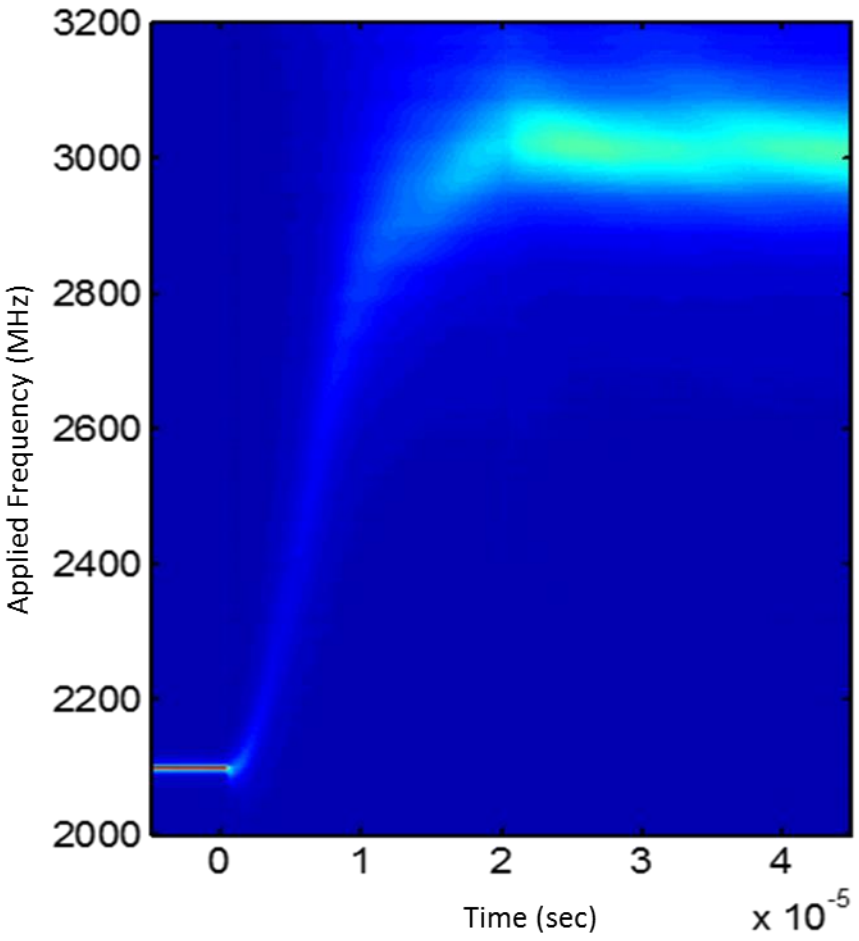

Figure 5.4 Absorbed power (color) at various microwave frequencies (y-axis) are displayed as a function of time (x-axis) for a 20μs applied voltage pulse. A sharp resonance peak in frequency space is observed before the voltage pulse (t=0) near the vacuum-resonant frequency. The resonant peak shifts to larger frequencies (due to increased electron density) and broadens (due to electron collisions) after the voltage is applied. The frequency peak sharpens after the applied voltage pulse ends at 20μs as electron collisions decrease.

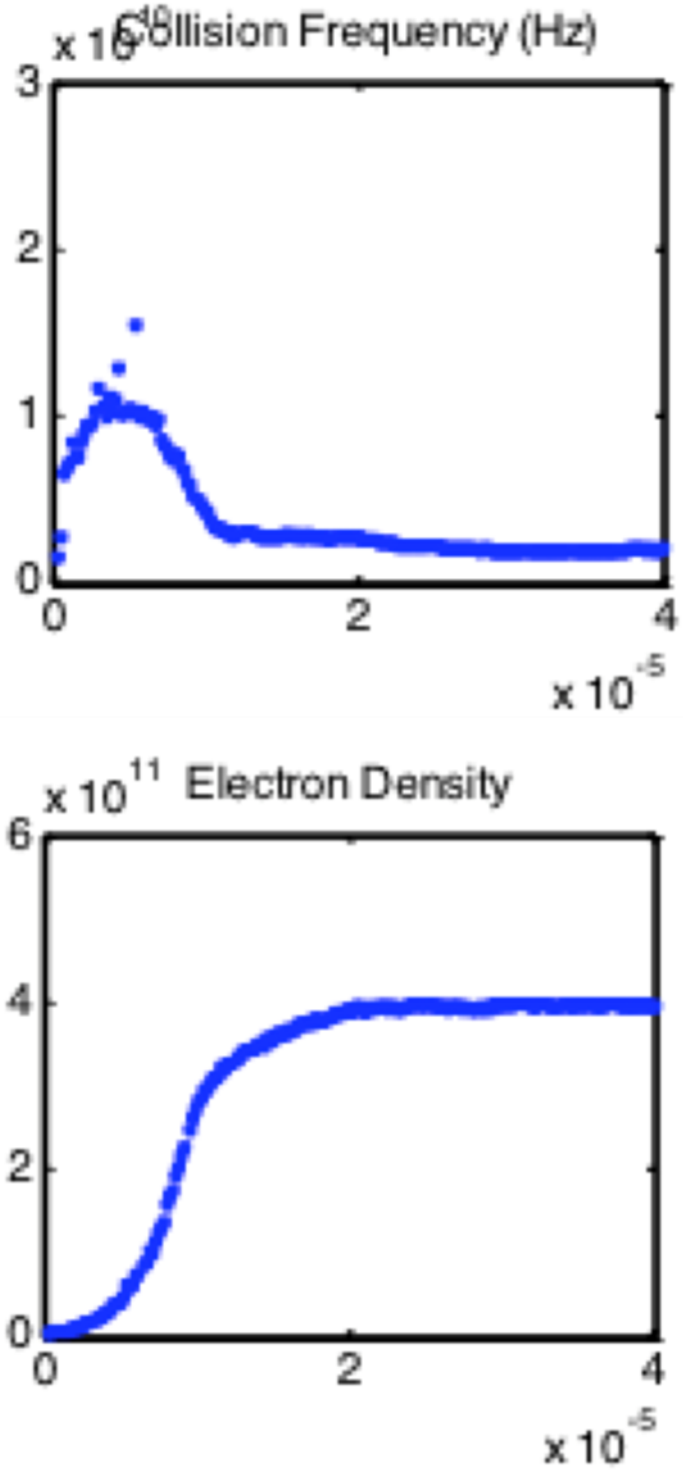
Collision Frequency (Hz)
x 10^8
3
2
1
0
0
2
4
x 10^-5
Electron Density
x 10^11
6
4
2
0
0
2
4
x 10^-5

Figure 5.5

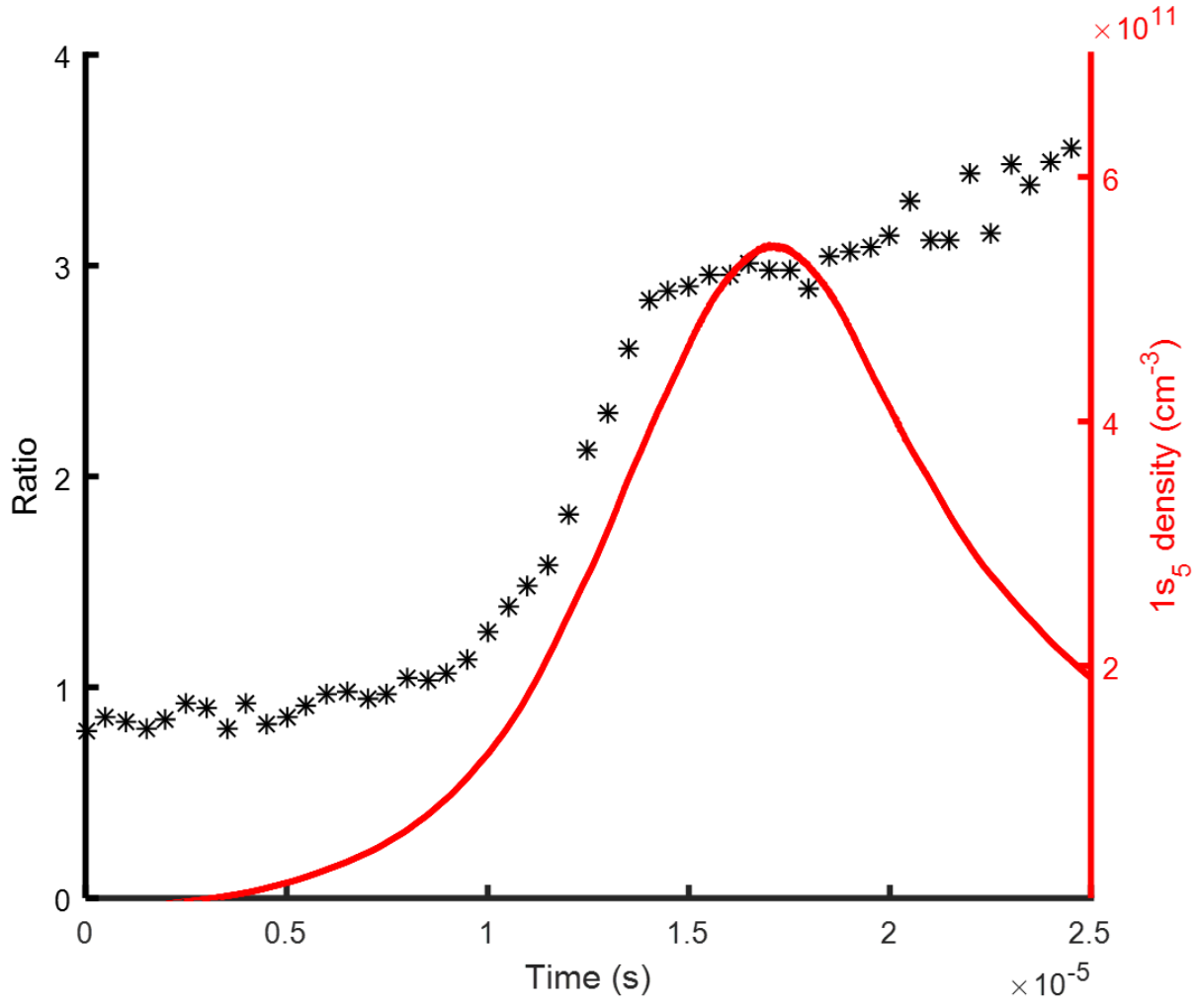

Figure 5.6 420.1-419.8nm emission-line ratio and metastable-atom density as a function of time throughout the discharge is shown. The peak of the metastable-atom density coincides with the time of maximum power input into the plasma and the onset of the Post-Transient stage (~15μs) of the discharge.

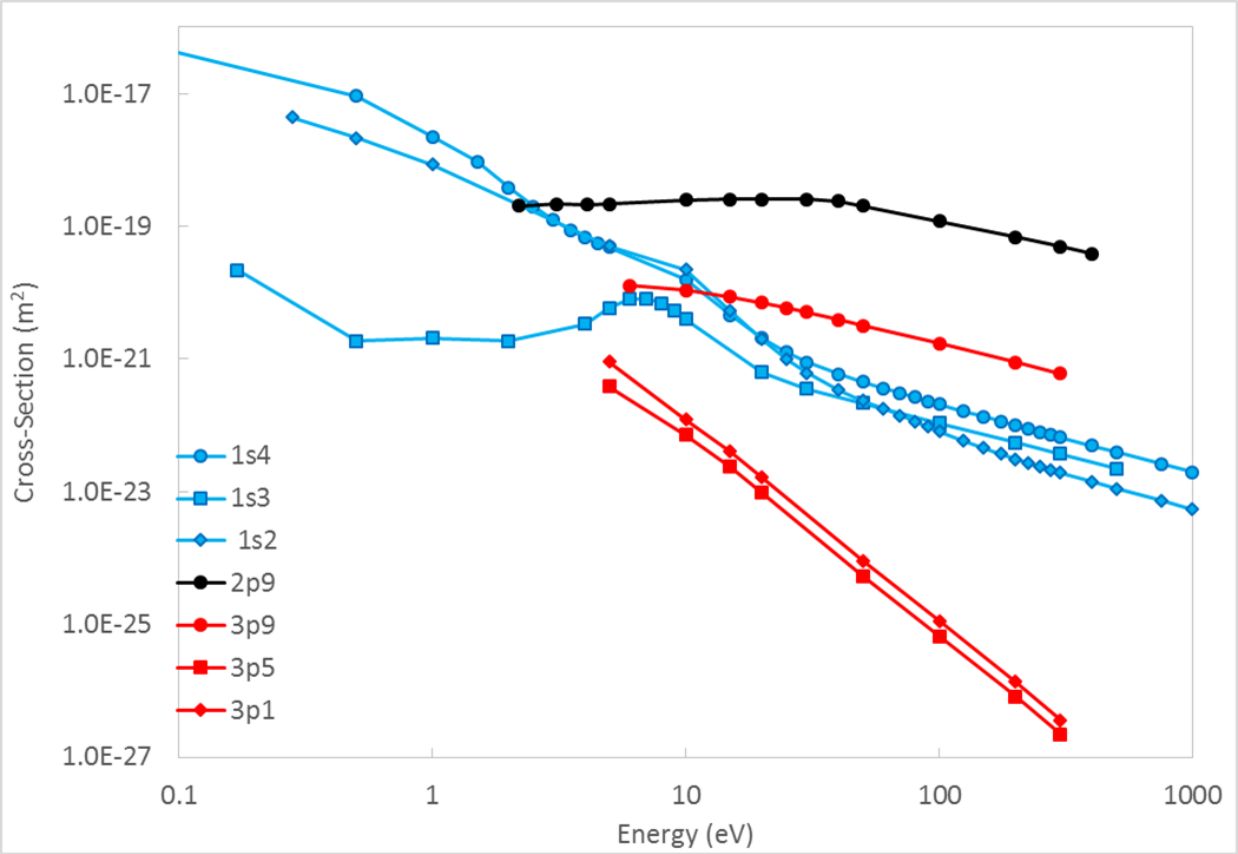

Figure 5.7 Cross sections for electron-collision-induced excitation out of the $1s_5$ state into select excited states are shown. The stepwise-excitation cross-sections into the $1s_4$, $1s_3$, and $1s_2$ states of argon are shown in blue. These states are energetically close (~0.1eV) to the $1s_5$ level and are dominant for small energies (E<3eV). Note, the spin-forbidden transition into the $1s_3$ state (blue square) is several orders of magnitude below the spin-allowed transitions for these energies. The cross section for dipole-allowed, spin-allowed transition into the $2p_9$ state (black) is the dominant excitation path for energies E>3eV. The dipole allowed, spin allowed transition into the $3p_9$ state is approximately an order of magnitude lower than the $2p_9$ state because the 3p manifold is ~1eV further removed from the $1s_5$ state in energy space. The cross sections for the dipole-forbidden, spin-forbidden stepwise excitation into the $3p_5$ and $3p_1$ states (red squares, red diamonds, respectively) are orders of magnitude lower even still. This is the backbone of the metastable-atom diagnostic presented in chapter 3.

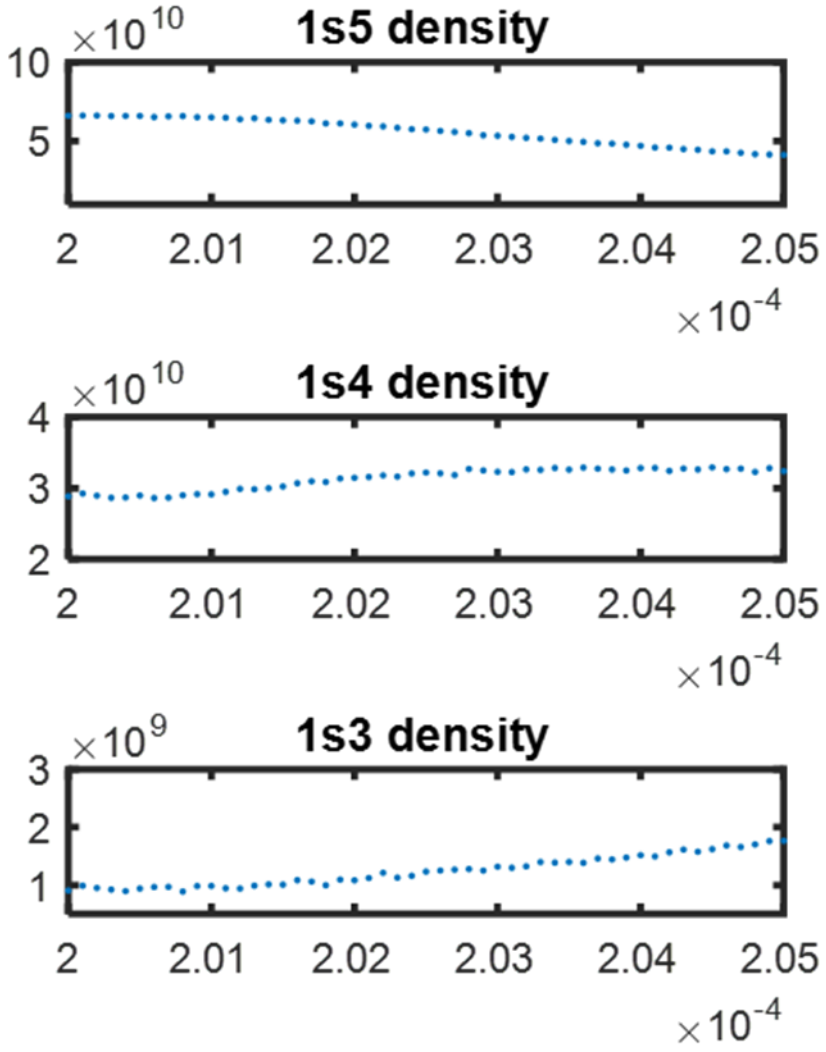

Figure 5.8 The density of the $1s_5$ metastable-atom decreases during the applied plasma-conditioning voltage pulse. Densities of the $1s_4$ and $1s_3$ states, however, increase, implying the metastable-quenching excitation routes $1s_5$-to-$1s_4$ and $1s_5$-to-$1s_3$.

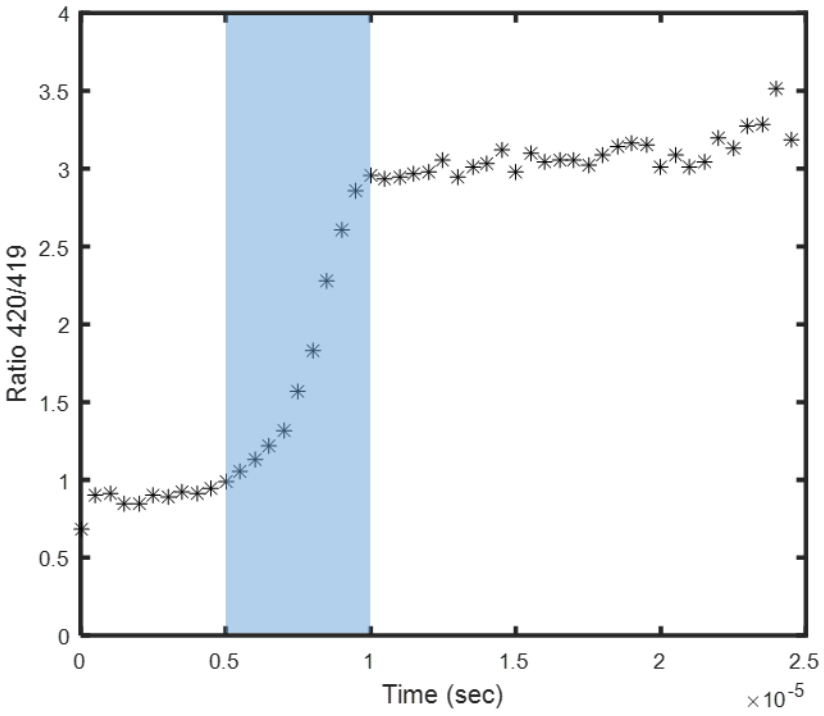

Figure 6.1 The observed 420.1-419.8nm emission-line ratio suggests the plasma emissions may be divided into three distinct stages: Initiation, Transient, and Post-Transient. The Initiation stage is characterized by a static, near unity value for emission ratio. The Transient stage is characterized by an increasing emission ratio. The Post-Transient stage is characterized by a static emission ratio which is greater than unity. Background shading signifies the Transient stage.

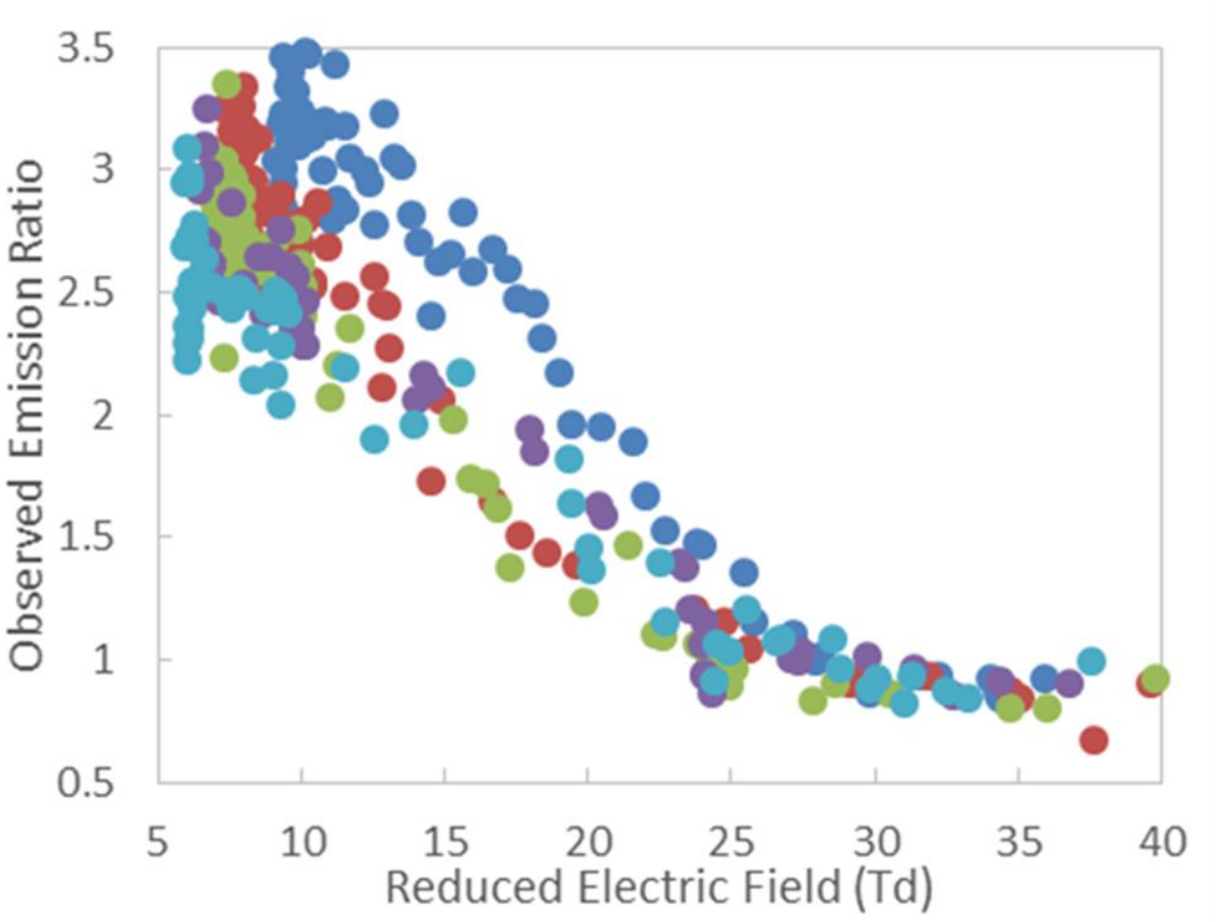

Figure 6.2 Observed emission ratio as a function of reduced electric field. Data taken at 1 Torr (dark blue), 2 Torr (red), 3 Torr (green), 4 Torr (purple) and 5 Torr (light blue) overlap for the range of E/N presented here.

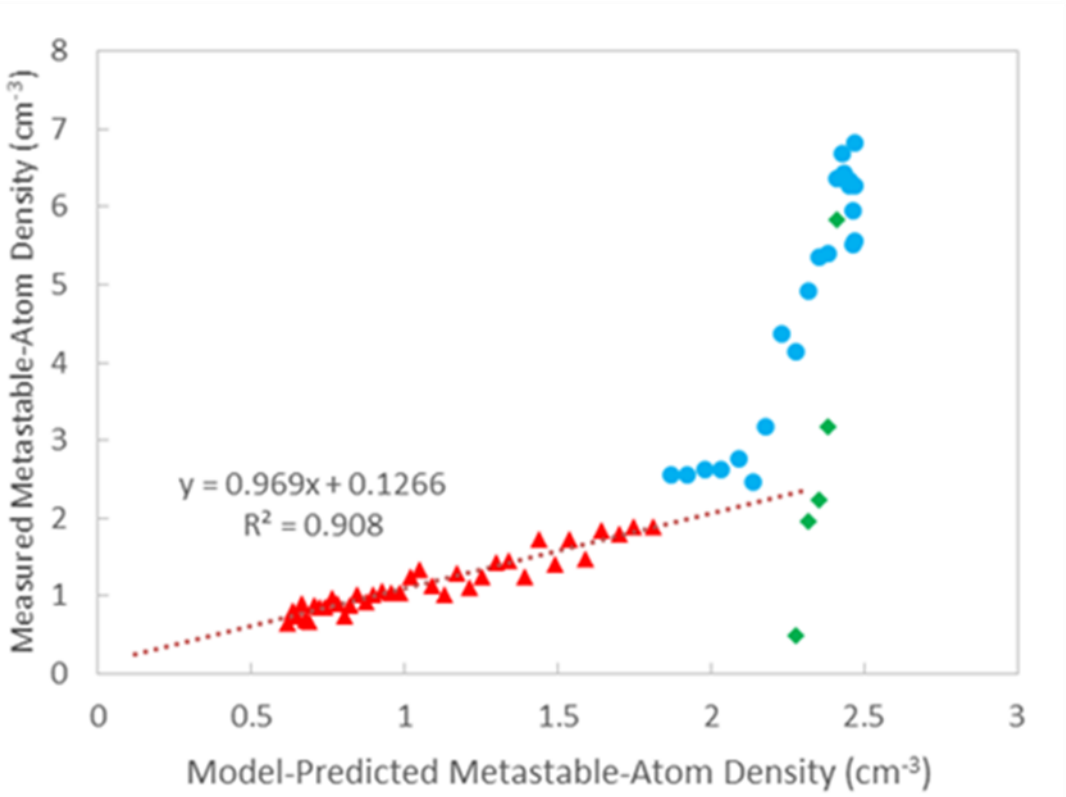

Figure 6.3 Measured metastable atom density vs. model-predicted metastable atom density for all stages of the pulsed positive column. Predictions are made using the calculated reaction rates of [*Adams et al.,* 2012] assuming metastable-atoms have no effect on the EED. Green diamonds, blue circles, and red triangles represent the Initiation, Transient, and Post-Transient stages respectfully. The comparison between densities in the Post-Transient stage show a nearly one-to-one relation between experiment and theory. Both axes are 10^6 times actual values.

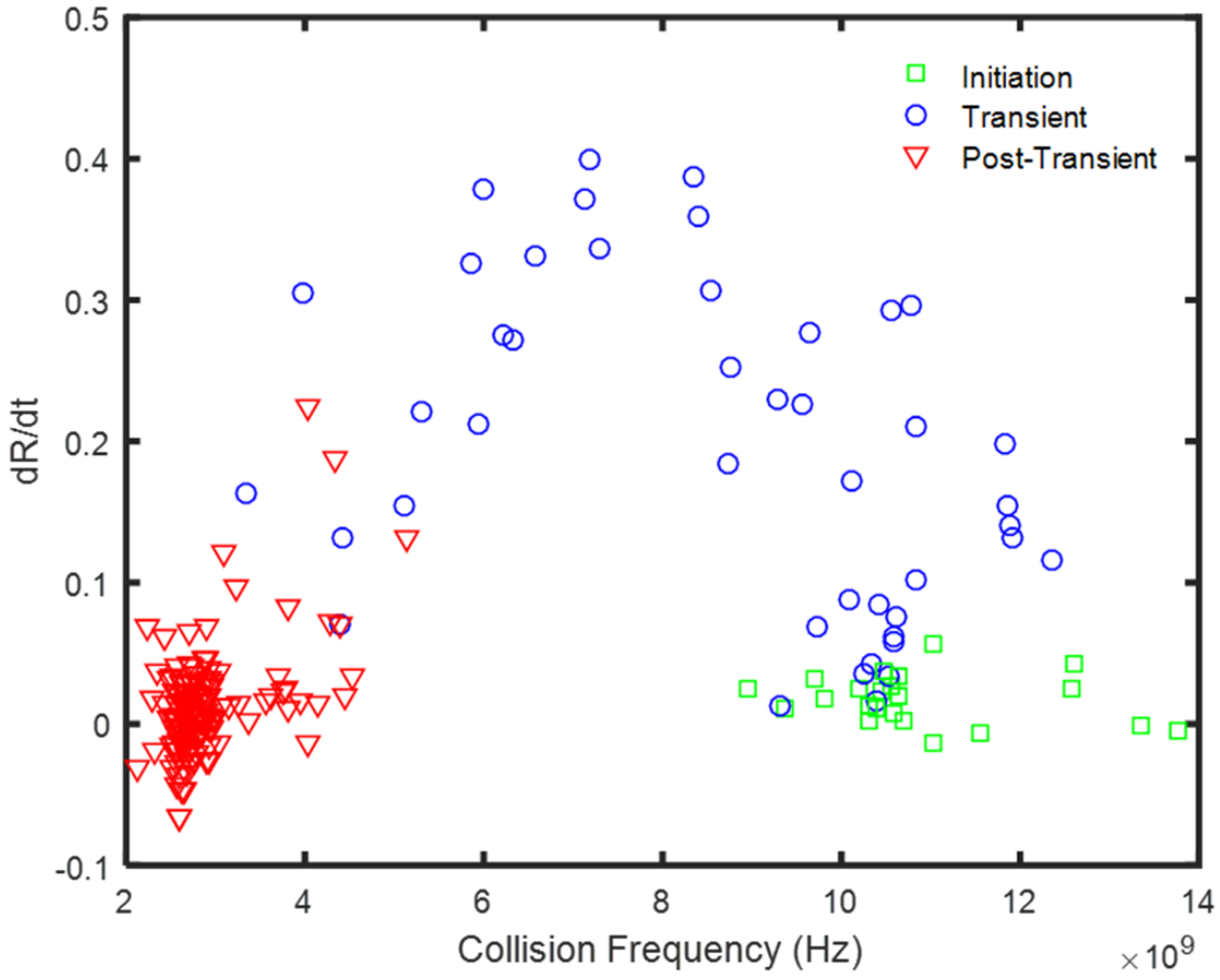

Figure 6.4 The rate of change of the 420.1-419.8nm emission-line ratio is plotted as a function of electron collision frequency. The Initiation stage (green squares) is described by large collision frequency and a static emission ratio. The Transient stage (blue circles) is described by a moderate collision frequency and a changing emission ratio. The Post-Transient stage is described by a low collision frequency and a static emission ratio.

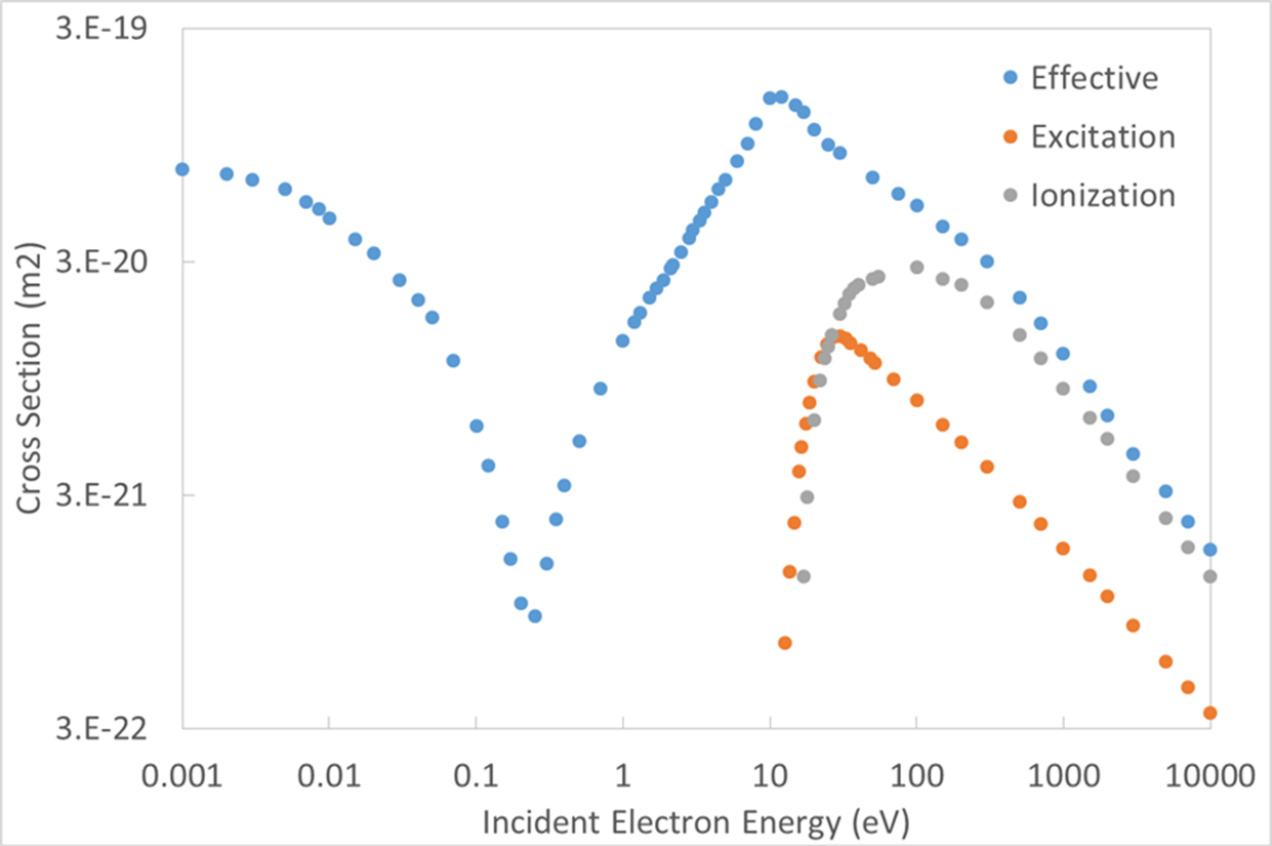

Figure 6.5 The effective collision cross-section for argon (blue) is sharply peaked near 10eV. Excitation and ionization cross-sections (orange and grey) are sharply peaked around 13eV and 15eV. Data taken from Lxcat. Effective cross-section taken from Puech database. Total excitation and ionization cross sections taken from Phelps database.

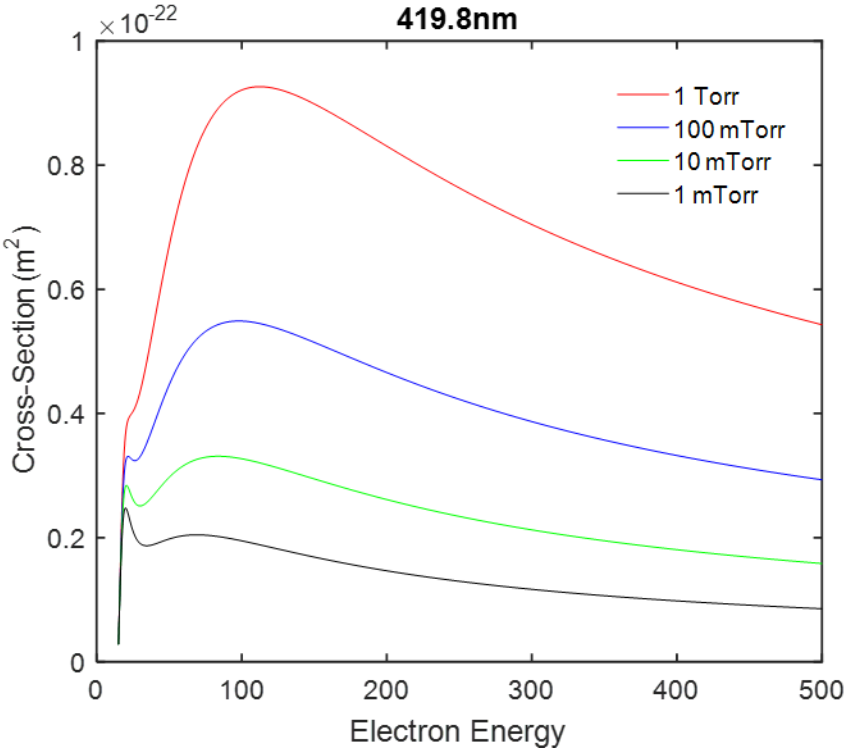

Figure 6.6 Optical emission cross-sections for the $3p_5$ state of argon at four different pressures is shown. The cascade contribution to the cross-section profile becomes dominant at a pressure of 1 Torr.

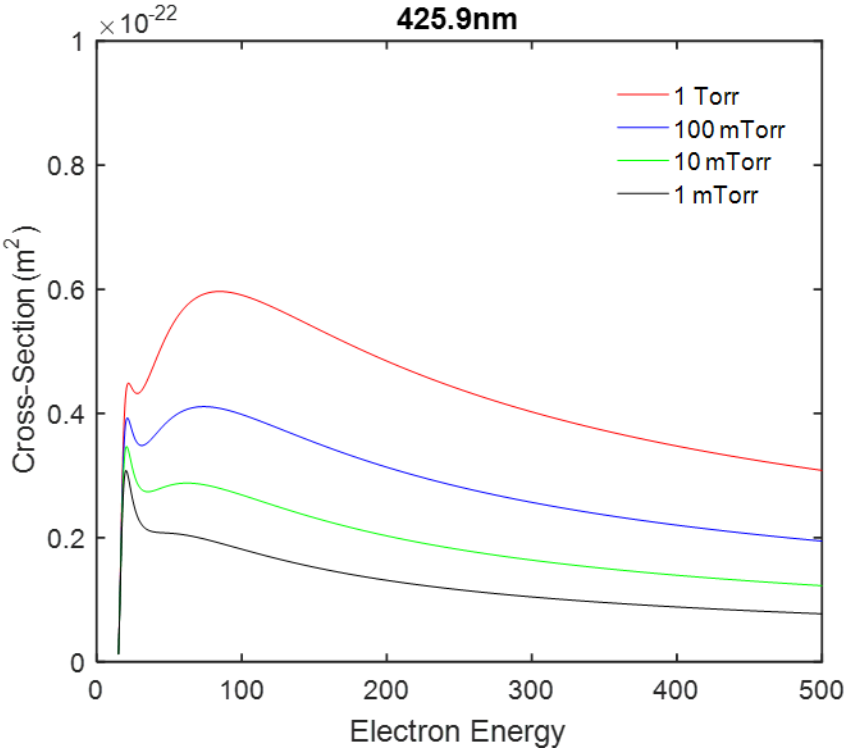

Figure 6.7 Optical emission cross-sections for the $3p_1$ state of argon at four different pressures are shown. The cascade contribution to the cross-section profile is comparable to the electron-exchange peak at 1 Torr.

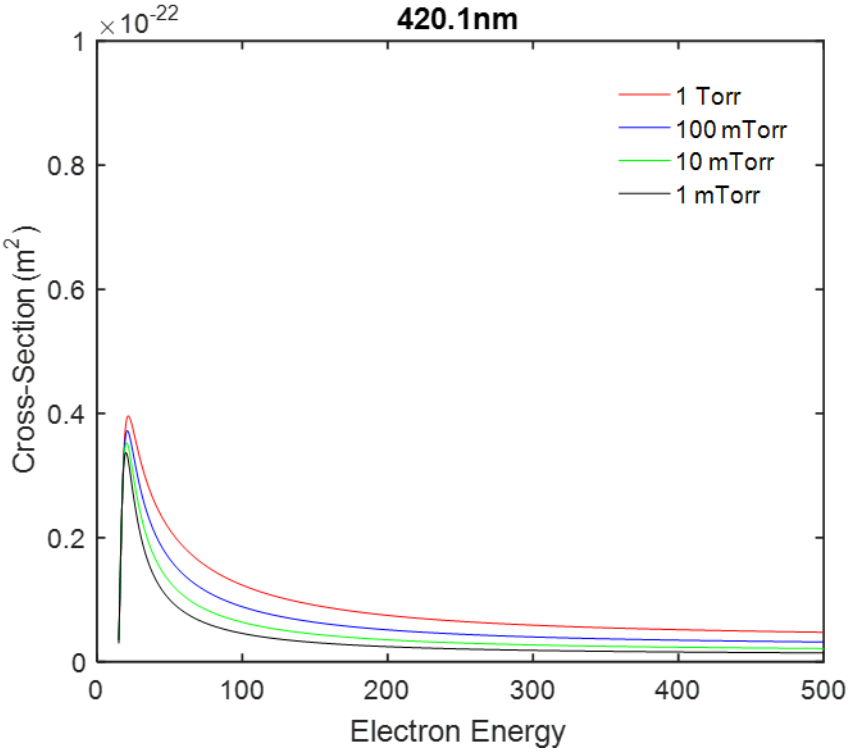

Figure 6.8 Optical emission cross-sections for the $3p_9$ state of argon at four different pressures are shown. The cascade contribution to the cross-section profile is dominated by the electron-exchange peak at 1 Torr.

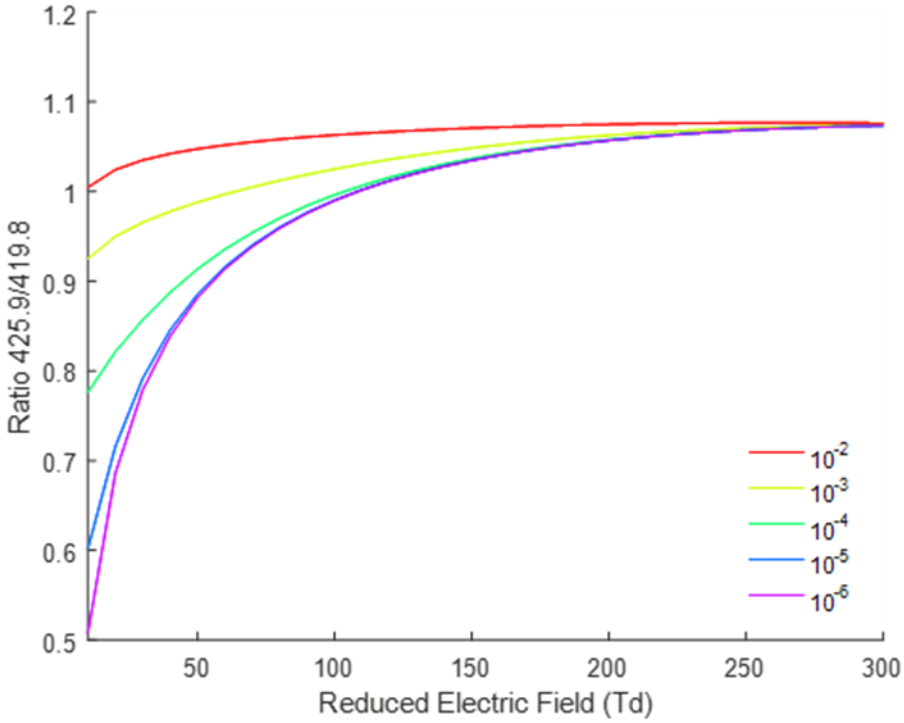

Figure 6.9 . Calculated 425.9-419.8nm emission-line ratio as a function of reduced electric field (E/N) is plotted for several ionization fractions. The ratio is near unity for all ionization fractions for high E/N.

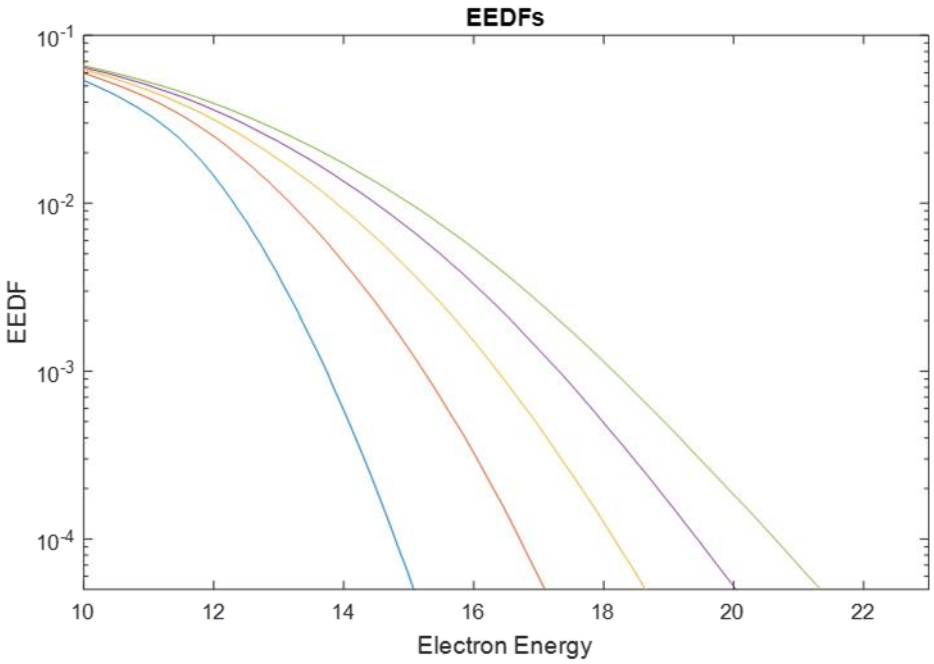

Figure 6.10 Increasing E/N populates the high energy tail of the EED. Electrons from the low-Energy bulk (below 10eV, not shown) are heated and populate the high energy tail of the EED.

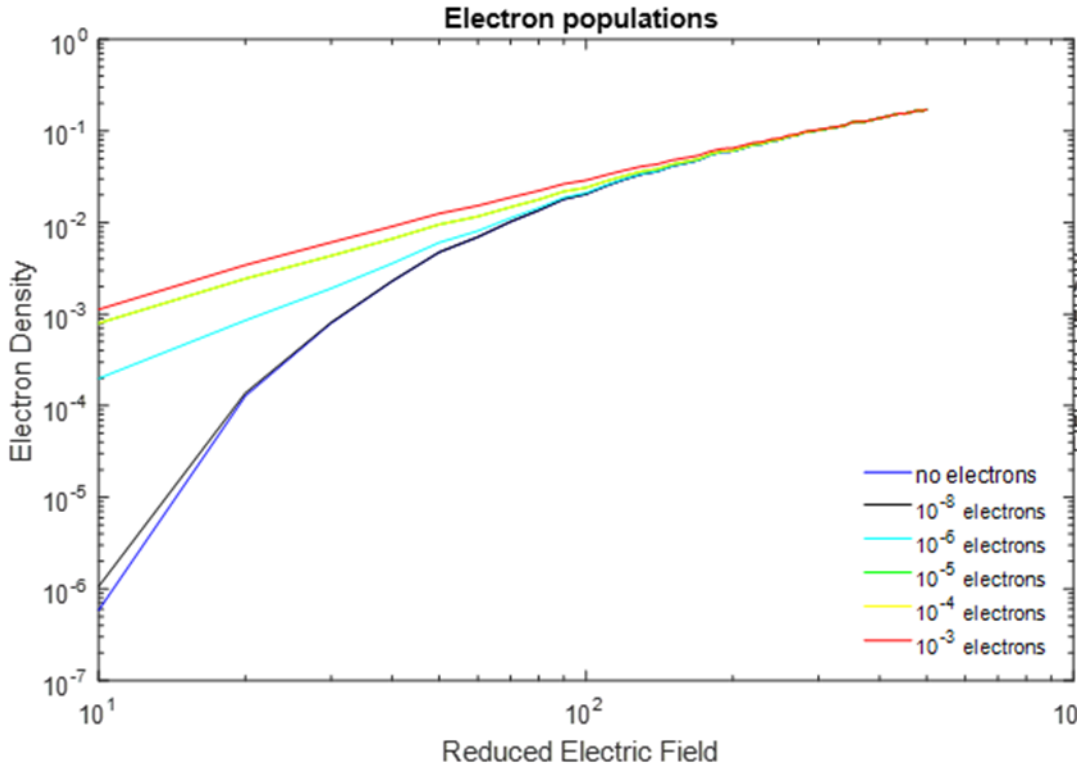

Figure 6.11 The percentage of electrons between 15 and 30eV increases drastically for low E/N as electron density increases; therefore, the 425.9/419.8nm line ratio increases with increasing E/N.

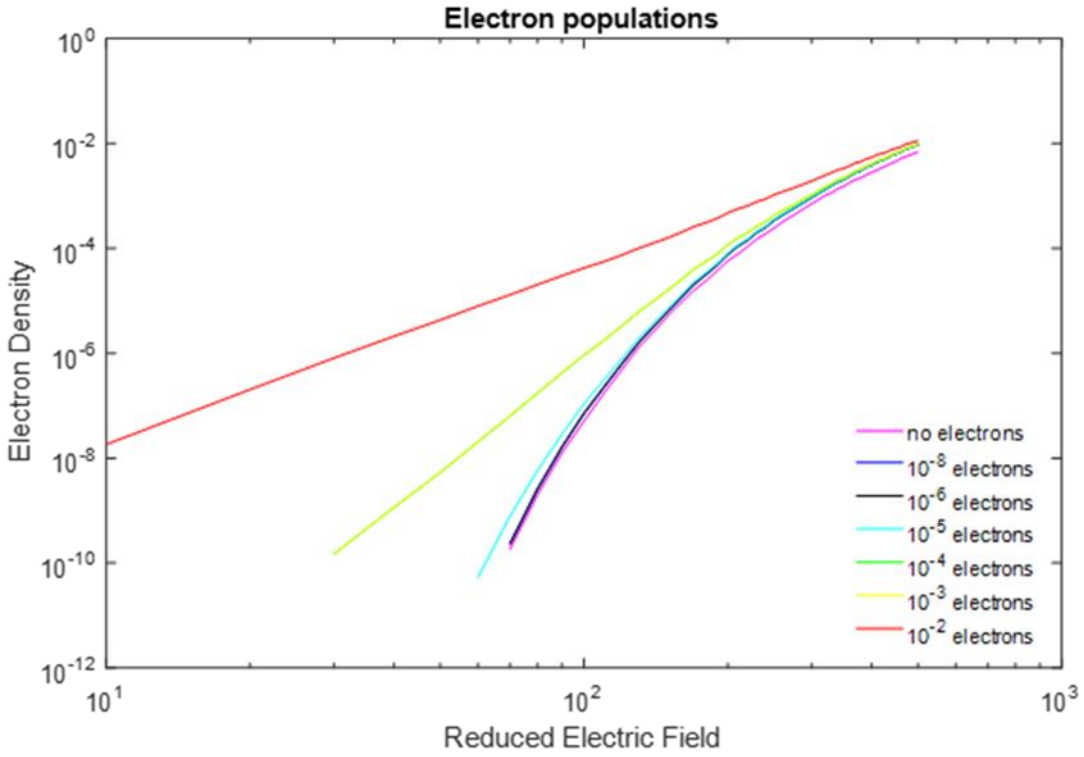

Figure 6.12 The percentage of electrons over 30eV increases drastically as electron density increases for low E/N. High energy (E>30eV) electrons favor 419.8nm emission, therefore, the 425.9-419.8nm emission-line ratio increases less-drastically with increasing E/N when these electrons are present.

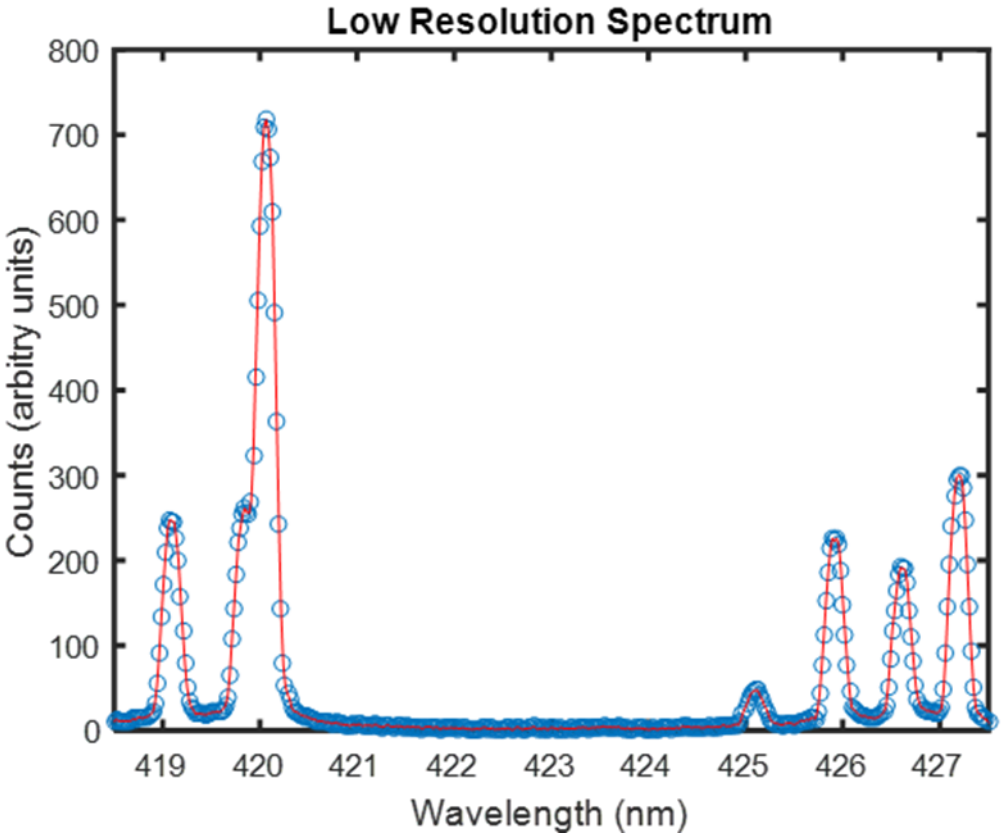

Figure 6.13 Argon spectrum obtained using a 1200 groove/mm diffraction grating. The argon 420.1nm and 419.8nm emission-lines overlap, and obtaining individual emission-line intensities is not straightforward.

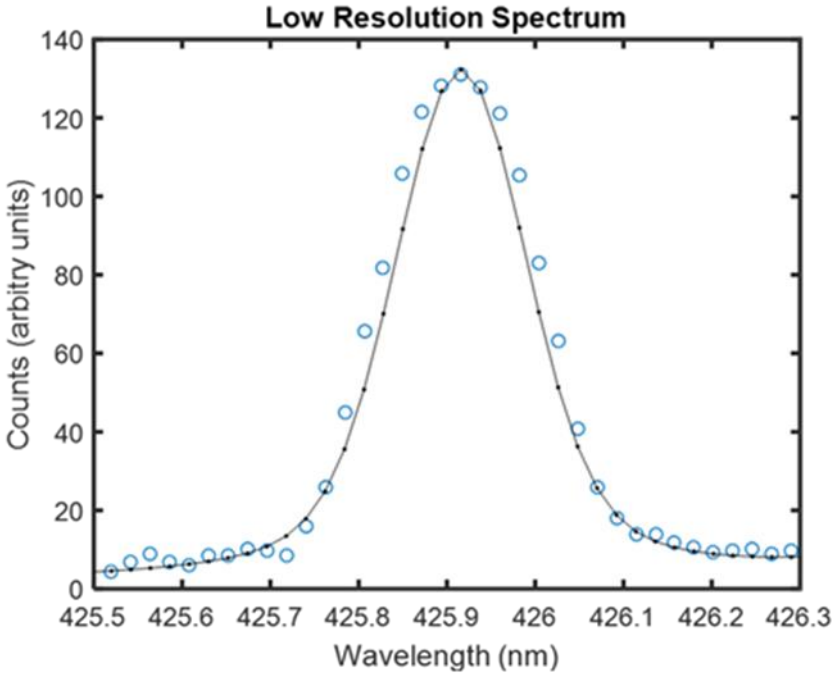

Figure 6.14 The argon 425.9nm emission-line is shown here. The blue circles represent observed data while the black trace represents the numerically computed Voigt profile.

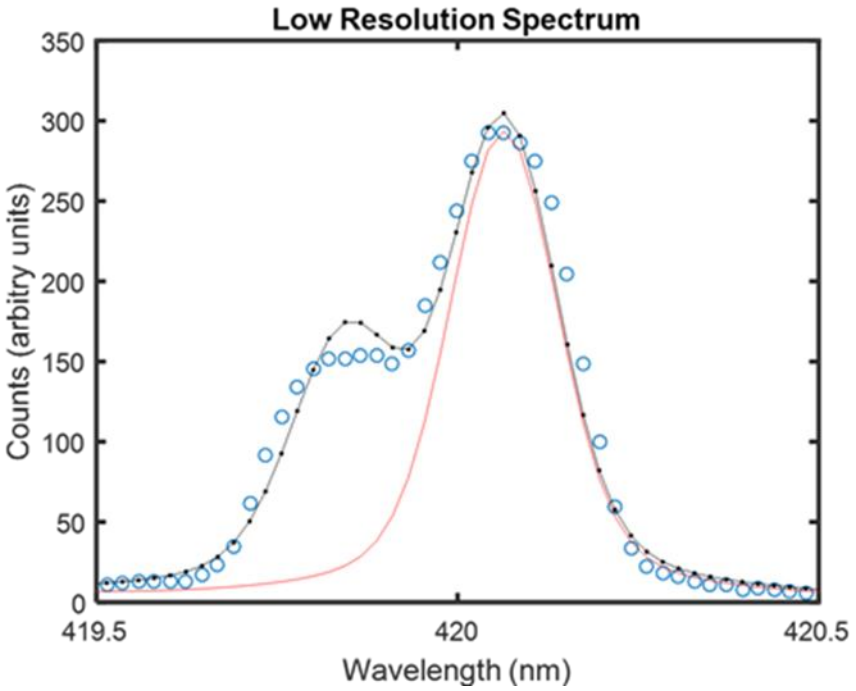

Figure 6.15 Emission-lines are constructed at 419.8 and 420.1nm by assuming the neighboring emission lines have no effect on the peak amplitude. The Gaussian and Lorentzian widths are assumed to be the same as calculated in the 425.9nm profile in figure 6.14. The calculated spectra (black) over-predicts the peak intensity at 419.8nm, which implies that the emission-line amplitude has a non-negligible contribution from the 420.1nm emission-line profile. Fitted data from the 425.9nm emission line is used to subtract-off the contribution of the 419.8nm emission line in the 420nm region. The corrected data (red) shows the peak of the 420.06nm line does not shift in wavelength space, nor decrease in amplitude, implying raw 420.1nm emission-line intensity taken with the 1200grooves/mm grating may be used in the plasma model without deconvolution.

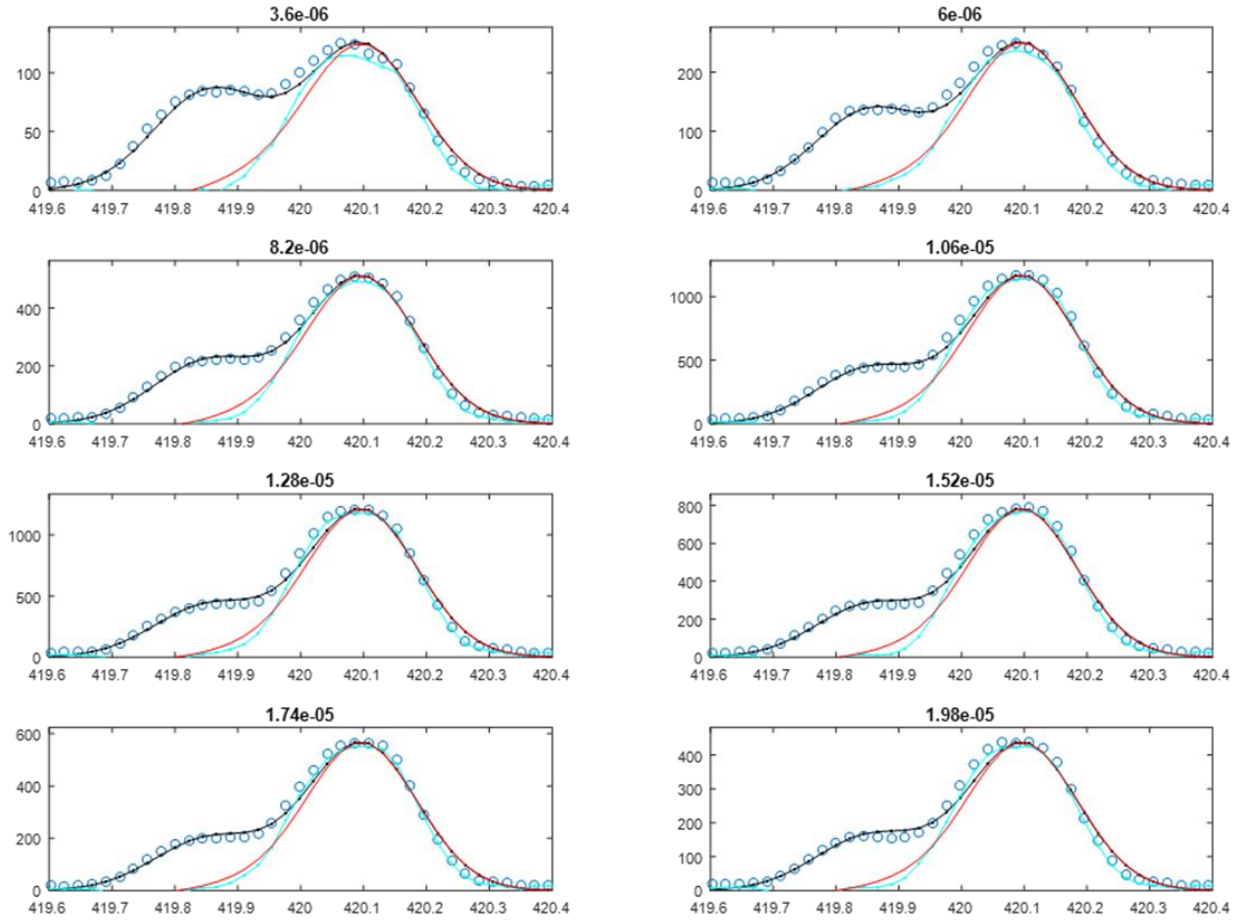

Figure 6.16 The corrected 420.1nm emission-line profile produced by empirical modeling (red) and raw data subtraction (cyan) are shown at various times throughout a 20μs voltage pulse. The two correction techniques are deemed to give similar results.

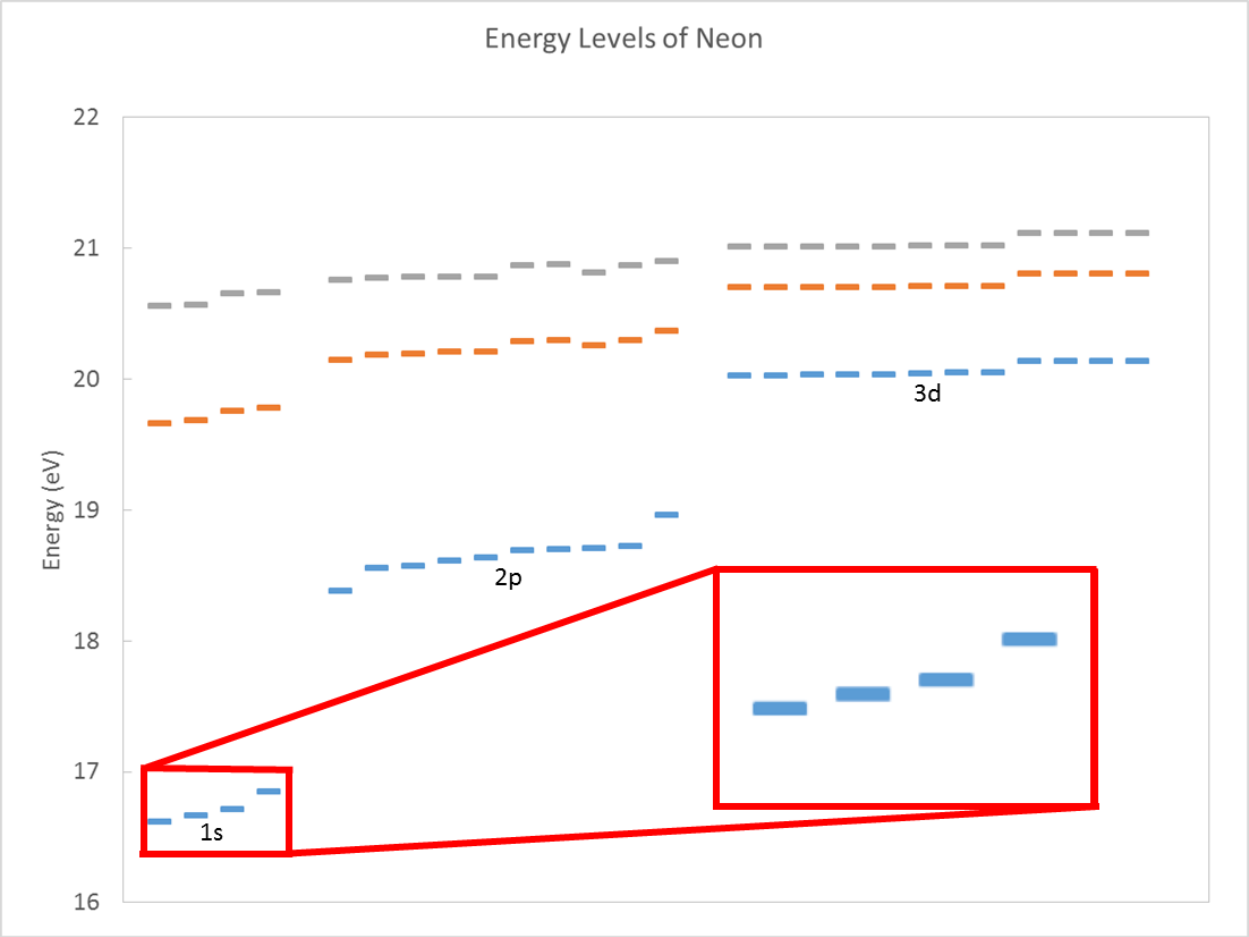

Figure A.1 The $1s_x$ manifold for neon (enlarged for n=3, blue) displays the triplet-singlet energy level structure predicted in Russel-Saunders coupling. This structure disappears for larger values of principle quantum number (n=4, orange, and n=5, grey) because the spin-orbit effect becomes dominant.

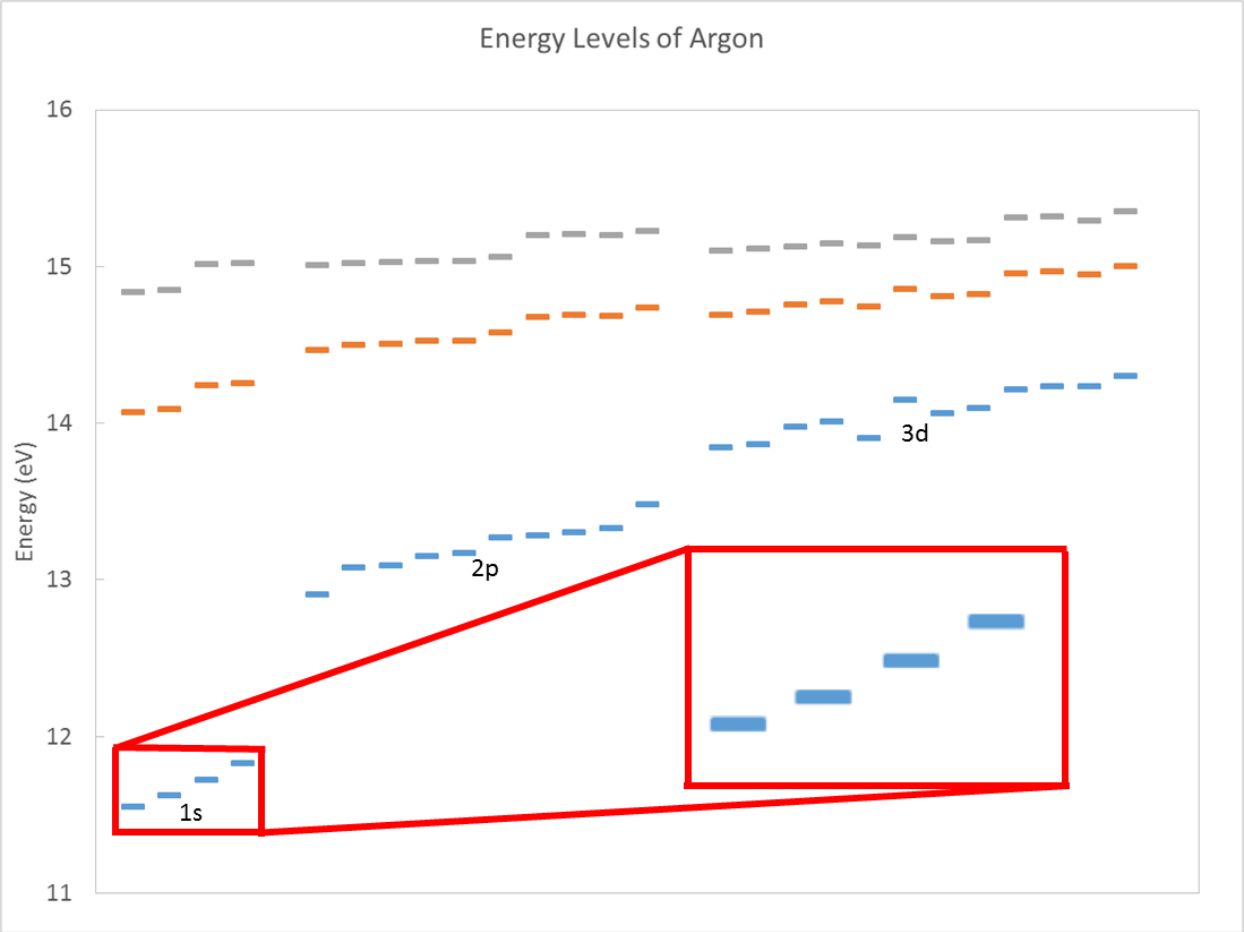

Figure A.2 The spin-orbit effect removes the triplet-like structure of the four levels in the 1s manifold; the manifold displays an “intermediate” nature, where the four levels of the 1s manifold (n=4, blue) are evenly spaced. The doublet-structure, indicative of j-j coupling, is seen in the n=5 (orange) and n=6 (grey) levels.

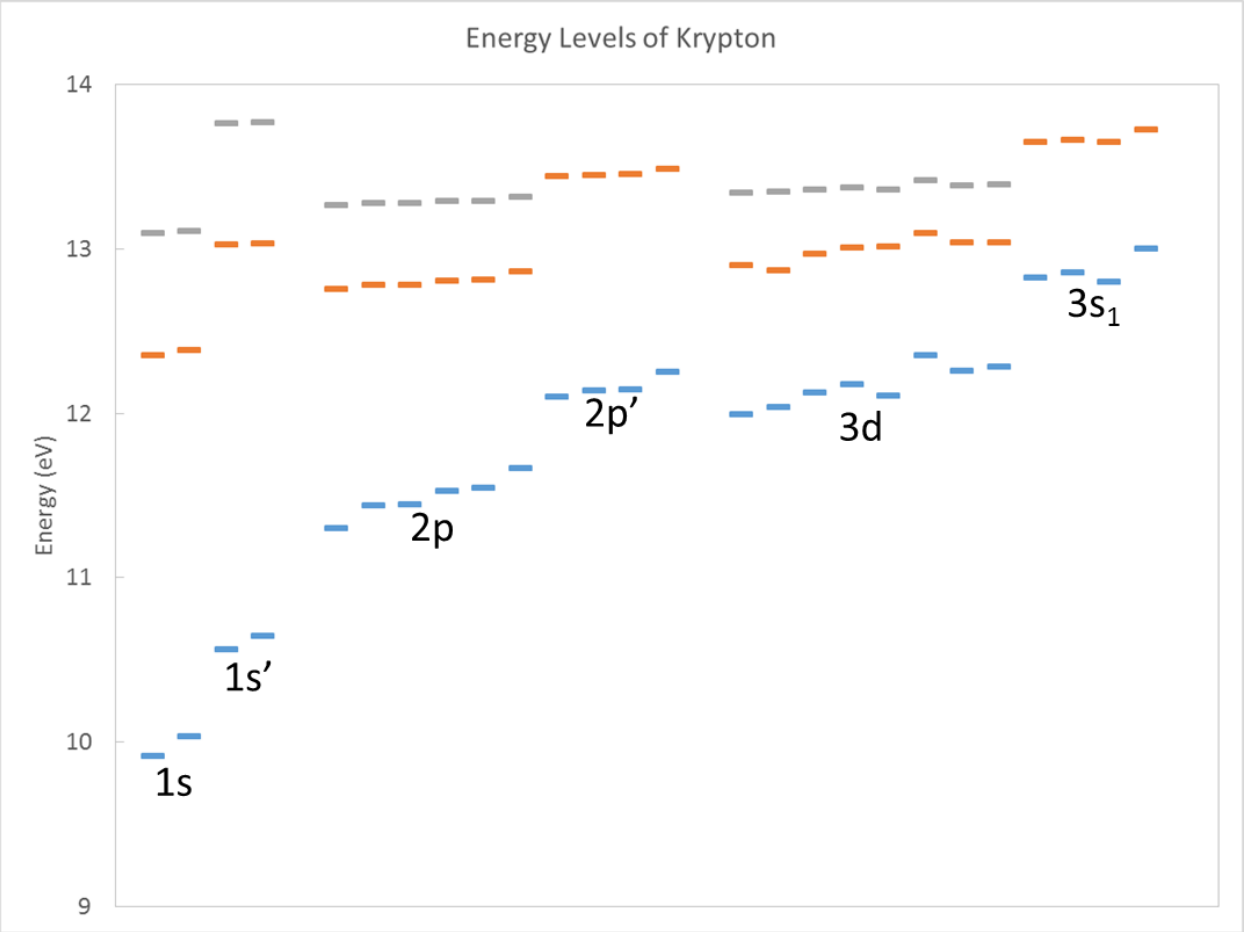

Figure A.3 *j-j* coupling for the three principle quantum numbers (n=5, blue, n=6, orange, and n=7, grey) separates the 1s, 2p and 3d manifolds. States with the j=1/2 ion-core are now labeled 1s', 2p' and $3s_1$.

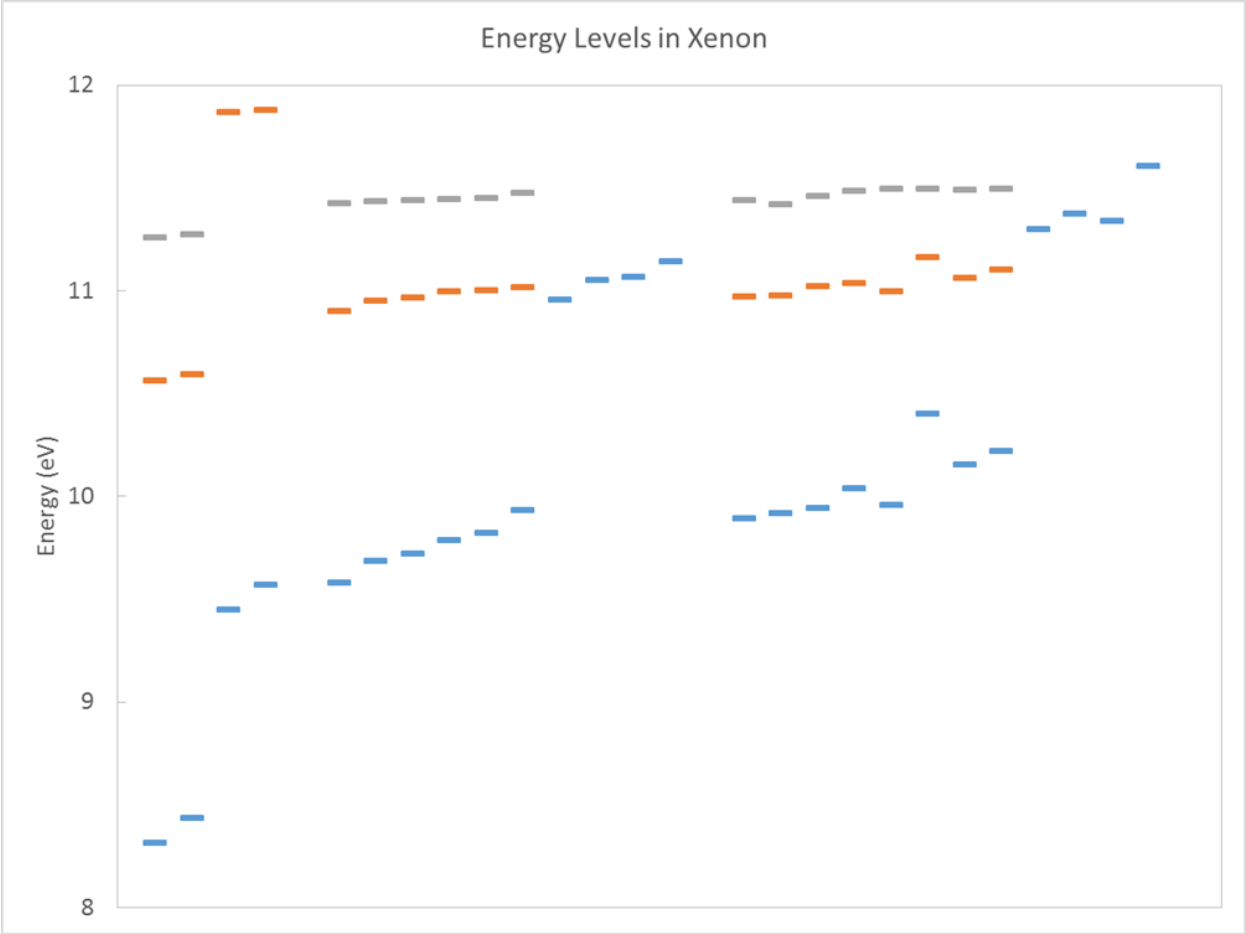

Figure A.4 The spin-orbit coupling is dominant, and 1s' levels (n=7, blue) in xenon (z=54) have energies comparable to the 2p levels. n=8, orange, and n=9, grey, are also shown.

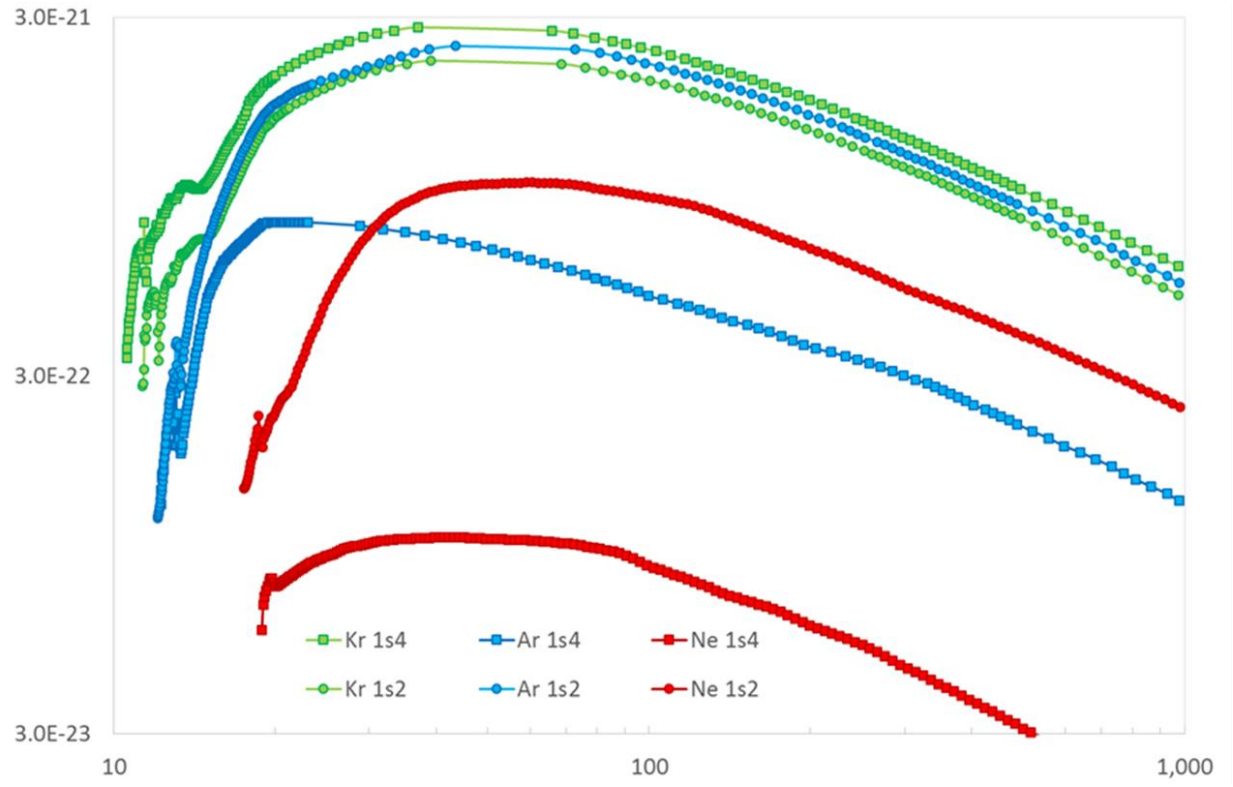

Figure A.5 Coupling Excitation into the $1s_2$ state of neon (red circles) has a triplet-like profile, which peaks ~4X above the excitation on-set energy because the wavefunction is dominated by the triplet ($^3P_1$) term. The $1s_4$ state of neon exhibits a singlet-like profile, which is characterized by a broader peak near the onset energy. The excitation cross-section profiles for the $1s_2$ and $1s_4$ states of krypton (green circles and green squares respectively) show very similar profiles because the states are heavily mixed, i.e. alpha~beta in equations ($1s_2$) and ($1s_4$). The excitation profiles for argon (blue) show an intermediate profile behavior in terms of breadth.